

NEW HORIZONS IN COMPUTER-AIDED DESIGN OF
SHEET METAL STAMPINGS

BY

EDMUND WAI-KWOK CHU, M. ENG.

A Thesis

Submitted to the School of Graduate Studies
in partial fulfillment of the Requirements
for the Degree
Doctor of Philosophy

McMaster University

© September 1983

SHEET METAL STAMPINGS

Dedicated to the Glory of God

"Blessed be the Lord, who
daily bears our burden, the
God who is our salvation."

Psalms 68:19

Also to my mother and Ada

Doctor of Philosophy (1983)
(Mechanical Engineering)

McMASTER UNIVERSITY
Hamilton, Ontario

TITLE: New Horizons in Computer-Aided Design of Sheet Metal Stampings

AUTHOR: Edmund Wai-Kwok 'Chu, B.Eng. (McMaster University)

M.Eng. (McMaster University)

SUPERVISOR: Dr. R. Sowerby

NUMBER OF PAGES: xv, 195

ABSTRACT

The determination of principal finite strains from measurements made on a pair of deformed line elements is discussed. The deformation process is assumed to be either homogeneous or pure homogeneous in nature. Emphasis is placed on the pure homogeneous mode since it leads to a simpler finite strain tensor and this technique is applied to determine the strain over the surface of an industrial stamping. The present work draws the distinction between homogeneous and pure homogeneous deformation. In the latter mode, an orthogonal triad can be identified (the principal axes), which remains orthogonal throughout the deformation. An appropriate strain measure in such processes is that of logarithmic strain. Furthermore, its material derivative equals the rate of deformation tensor. Such a simple expression does not hold when the deformation gradient tensor is nonsymmetric, as in homogeneous processes.

The material derivative of the tensor logarithm is no longer simply related to the rate of deformation tensor, and this is exemplified herein. The resulting expression involves the spin of the triad of the Eulerian and Lagrangian ellipsoids.

Stress components vary as a result of material rotation and constitutive equations whereby rotational effect of material has been accounted for must be formulated. In finite deformation various "rotation" tensors can be defined. Consequently a wide choice of

objective stress rates is available for adoption in constitutive equations, and a number of objective stress rates are examined herein. The utility of the resulting expressions is demonstrated for the case of a hypoelastic material undergoing finite deformation in simple (rectilinear) shear.

Another aspect of this work has been an attempt to establish an approximate computer-aided technique for blank development, referred to as Geometric Modelling, and the investigation of possible strain distributions in forming sheet metal components. The technique is based on the initial assumption (this can be refined at a later stage) that a sheet metal component is transformed from a flat sheet into a non-developable surface without change in thickness. Although few practical forming processes occur in this way, many traditional die design procedures are based on similar notions; either there is no change in surface area or that a line length on the undeformed blank is unchanged during forming. Simple plasticity theory also suggests that the membrane stresses in a sheet would be minimized (in the absence of a normal stress) if no change in thickness occurred, therefore given the opportunity, the deformation is likely to take place in this ideal manner. The method of geometric modelling simulates the traditional manual calculations performed by experienced tool designers. The technique does not aim to replace the skill and experience of the designers but rather to enhance them.

The present work describes the formulation of the fundamental theories of the method which comprise of the element-by-element mapping

and remapping procedures and techniques of surface adjustment. The basic geometric assumptions employed in the development are also described. Two particular automotive stampings have been considered; one is the corner section of a car seat panel and the other is an inner deck-lid of a mid-size vehicle.

A computer-aided design package for tool/die designers has been developed and the detailed analytical procedure is implemented in Fortran code. The analysis has been performed without access to advanced computer graphics. However, it is carried out in a way that future modelling using interactive computer graphics may well be attainable.

ACKNOWLEDGEMENTS

The author would like to record his deep appreciation to his supervisor, Professor R. Sowerby; for his assistance, guidance and continual encouragement in every aspect of this work. The valuable stimulation of the present research, the extensive discussion, support and advice in personal matters provided by Professor J.L. Duncan in the past few years are sincerely acknowledged.

"Finite deformation processes are essentially material rotation in nature". This inspiring statement initiated by Professor G.A. Cravas has changed the author's total outlook towards problems involving large deformation, his inspiring teaching and continual support in various stages of this work is deeply appreciated.

The author would like to thank Professors J.P. Duncan and S.G. Wang, both at the University of British Columbia, for their comments and discussions. Thanks are also extended to my fellow students, in particular, Mr. R. Soldaat and Ms. V. Donatelli for their contributions to this work.

The financial support granted by the Natural Sciences and Engineering Research Council of Canada and by the Ford Motor Company, Dearborn, Michigan, are sincerely acknowledged.

Thanks are also due to the staff of the Engineering Word Processing Centre for their expert typing of the manuscript.

TABLE OF CONTENTS

	<u>Page</u>
List of Symbols	x
List of Captions	xi
CHAPTER 1 INTRODUCTION	1
1.1 Preamble	1
1.2 Scope of the Research	5
1.2.1 Ideal Finite Deformation Processes	5
1.2.2 The Ideal Sheet Metal	7
CHAPTER 2 THE ANALYSIS OF FINITE STRAINS IN METALFORMING	9
2.1 Introduction	9
2.2 Theoretical Considerations	12
2.2.1 Finite Homogeneous Deformation	12
2.2.2 Pure Homogeneous Deformation	16
2.3 Strain Analysis of an Industrial Stamping	21
2.3.1 General Comments	21
2.3.2 Experimental Strain Determination	26
2.4 Discussion	36
2.5 Conclusions	41
CHAPTER 3 GEOMETRIC MODELING	43
3.1 Introduction	43
3.2 The Ideal Sheet Forming Process	45
3.3 Techniques for Mapping Elements	48
3.3.1 Basic Method	48
(a) Mesh Generation	48
(b) Boundary Conditions	49
3.3.2 Mapping Strategies	53
(1) Proportional Deformation	53
(2) Proportional Change of Angles	58
(3) Proportional Area Change	59

	<u>Page</u>
3.3.2 (4) Intersection Method	61
(5) Area Criterion	65
3.3.3 Comments on Mapping Strategies	69
3.4 Remapping - A Theoretical Consideration	70
3.4.1 General Comments	76
3.5 Adjustment	77
3.6 The Evaluation of Finite Strain	81
3.7 Modelling of an Automobile Inner Panel	86
3.7.1 Mesh Generation and Boundary Conditions	86
3.7.2 Discussion	88
3.8 Conclusions	101
 CHAPTER 4 ON THE RATES OF STRESS AND STRAIN MEASURES IN FINITE DEFORMATION	 103
4.1 Introduction	103
4.2 Some Theoretical Fundamentals	108
4.2.1 Deformation Gradient	109
4.2.2 Velocity Gradient	111
4.3 Some Basic Measures of Stress and Strain	113
4.3.1 Conjugate Variables	114
4.3.2 Stress Rates	115
4.3.3 Principal of Material Frame Indifference	117
4.4 Method of Analysis	119
4.4.1 Spins of the Strain Ellipsoids	119
(a) Lagrangian Strain Ellipsoid	120
(b) Eulerian Strain Ellipsoid	122
4.4.2 Choice of Strain and Strain Rate Measures	122
4.4.3 Choice of Stress Rate Measures	126
4.4.4 Frame Indifference Quantities	130
4.5 Rotations and Stress Rates in Simple Shear	133
4.5.1 Discussion	141
4.5.2 Conclusions	143

	<u>Page</u>
APPENDIX A The Evaluation of Finite Strain	145
APPENDIX B The Plotting of Strain Contours	148
Introduction	148
Basic Concept	153
Cubic Spline Interpolation	155
APPENDIX C The Mapping of a Hemispherical Shell: A Test Case	159
Introduction	159
The Test Case	160
Mapping, Assuming No Change in Thickness of Blank	162
(a) Proportional Deformation	163
(b) Intersection Method	165
(c) Area Criterion	165
Influence of Grid Shape	167
Remapping	170
Adjustment	170
APPENDIX D Flow Charts	174
APPENDIX E List of Subprograms	179
APPENDIX F Strain Ellipsoids	183
Lagrangian Strain Ellipsoid	183
Eulerian Strain Ellipsoid	184
Strain Measures	185
Stress Rates	187
Stress Rates in Simple Shear	189
References	193

List of Symbols

\underline{F}	Deformation gradient tensor	\underline{t}	covariant kirchhoff stress tensor
\underline{C}	Deformation tensor	\underline{E}	Green's strain tensor
\underline{L}	Velocity gradient tensor	$\underline{\varepsilon}$	Almansi strain tensor
\underline{P}	Tensor of eigenvectors	$\underline{\dot{\sigma}}^+$	Cauchy stress rate
\underline{R}	Rigid body rotation	$\underline{\dot{\sigma}}^{\nabla}$	Jaumann stress rate
\underline{U}	Right stretch tensor	$\underline{\dot{\sigma}}^*$	Truesdell stress rate
\underline{V}	Left stretch tensor	$\underline{\Delta \dot{\sigma}}$	Hill stress rate
$\underline{\lambda}$	Diagonal tensor of \underline{U}	\underline{Q}	Orthogonal tensor
\underline{P}	Orthogonal tensor	$\underline{d}\eta$	Symmetric deformation gradient
\underline{D}	Rate of deformation tensor	$\underline{\hat{\sigma}}$	Objective stress rate
\underline{W}	Spin tensor	\underline{I}_R	Conjugate stress tensor
$\underline{\sigma}$	Cauchy stress tensor	$\underline{\psi}$	Rotationless tensor
\underline{I}	Kirchhoff stress tensor	$\underline{\Omega}$	Skew symmetric tensor
\underline{T}	First Piola-Kirchhoff stress tensor	$\underline{\dot{\sigma}}^*$	Proposed stress rate
\underline{S}	Second Piola-Kirchhoff stress tensor	$\underline{\phi}$	Skew symmetric tensor
$\underline{\nabla T}$	Co-rotation stress rate tensor	$\underline{\bar{\varepsilon}}$	Representative strain
$\underline{\nabla \sigma}_R$	Modified Cauchy stress rate	$\underline{\varepsilon}_1$	Principal strains
λ_1	Principal stretch ratio	$\underline{\dot{w}}$	Rate of work done
$\delta\phi_{1E}$	Spin of the Eulerian ellipsoid	$\underline{\bar{p}}$	Position vector
$\delta\phi_{1L}$	Spin of the Lagrangian ellipsoid	$\delta\theta_1$	Rigid body rotation
		J	Jacobian

List of Captions

<u>Figure</u>		<u>Page</u>
2.1	represents the homogeneous deformation of the initial square OABC	13
2.2	(a) Simple shear mode (b) A circle is deformed into an ellipse by homogeneous deformation (c) The same shape change in (b) can be achieved by pure homogeneous deformation	18
2.3	A flow diagram indicating the complete logistics of the strain program	23
2.4	Photograph of a typical autobody pressing which was scribed with an initially square grid	24
2.5	A sample of a typical stencil of circle grid pattern	25
2.6	(a) Initially undeformed square elements represented by triangular facets (b) The deformed configuration of (a)	25
2.7	Square grid analysis (a) A computer plot of the upper portion of the stamping in Fig. 2.4 (b) Strain contours are plotted in the undeformed blank	29
2.8	Square grid analysis (a) A mesh of the lower half of the panel in Fig. 2.4 (b) Strain contours of (a) on the flat plane	30
2.9	Circle grid technique (a) A computer plot of the upper part of the panel (b) Resulting strain contours are plotted on the undeformed sheet	32
2.10	Circle grid technique (a) A mesh of the lower portion of the panel (b) Strain contours in the flat sheet	33

	<u>Page</u>
2.11 Element strains plotted in $\epsilon_1-\epsilon_2$ strain space	34
(a) Square grid method	
(b) Circle grid method	
2.12 Contours of equivalent strain distributions	39
(a) Measured by the square grid	
(b) Computed from the circle grid	
2.13 Contours of effective strain distributions which were colour-coded	40
(a) Square grid technique	
(b) Circle grid technique	
(c) Colour codes of strain level	
3.1 (a) Deformation of an element in plane stress	47
(b) A plane stress yield locus	
3.2 (a) Part of a surface in space	47
(b) Boundary conditions of Fig. 3.2(a) on a flat plane	
3.3 Photographs:	51
(a) of a car seat stamping and	
(b) the area removed from the corner for modelling	
3.4 Mesh obtained for part of a car seat panel which is modelled	52
3.5 (a) Quadrilateral element on the curved surface	55
(b) Locating the fourth node in the plane surface	
(c) Illustrating the assumed proportional deformation	
3.6 Transformation of the mesh in Fig. 3.4 onto the flat plane, overlapping of some elements occurs with the proportional deformation strategy	56
3.7 An improved transformation into the flat plane	56
3.8 (a) A facet on the curved surface	57
(b) Diagram showing the assumed proportional change of angles	/
3.9(a)-(e) Diagrams illustrating the sequential mapping procedures of the fourth node L by the intersection method	64
3.10(a)-(e) Diagrams indicating transformation procedures for finding the most probable position of the node L using the method of area criterion	67

	<u>Page</u>
3.11 The resulting transformation of the surface in Fig. 3.4 which is obtained by applying the method of area criterion	68
3.12 (a) Illustrating the position of a remapped point on the surface (b) Diagram indicating the irregular grid points developed by mapping and the superposed regular mesh	71
3.13 A flow chart showing the strategy involved in the remapping procedure	72
3.14 The existence of Q within the quadrilateral ABCD is determined by a vector cross-product rule	75
3.15 (a) Indicating the position of Q and the parameters used to define Q (b) The position of Q' is determined by the corresponding area ratios P1 and P2 in space	75
3.16 Schematic representation of adjustment methods (a) Adjustment of a flat blank performed in a desired direction to the x-axis (b) Adjustment of an arbitrary region over the surface of a blank	79
3.17 (a) Element ABC in the initially undeformed configuration (b) The same element in (a) in the deformed configuration	83
3.18 A photograph of part of an industrial stamping in Fig. 2.4 onto which an irregular mesh was constructed with a marker pen	89
3.19 Isometric projection of the left-hand irregular mesh shown in Fig. 3.18	90
3.20 "Constant area" mapping of the element in Fig. 3.19 onto a plane	90
3.21 Superimposing an array of rectangular elements on the resulting map in Fig. 3.20	91
3.22 Remapping of the regular mesh onto the part surface	91
3.23 A computer plot of the right-hand irregular mesh on the surface of the deck-lid in Fig. 3.18	92
3.24 The mapping of "constant area" irregular patches onto a plane	92

	<u>Page</u>	
3.25	Overlaying of a regular mesh on the blank with equal number of element	93
3.26	Remapping of the regular elements in Fig. 3.25 onto the part surface	93
3.27	The entire resulting transformation of the hand-drawn irregular mesh in Fig. 3.18 onto a flat plane	94
3.28	Photograph of the deck-lid onto which the regular grid in Figs. 3.22 and 3.26 has been transferred. (The features in the region indicated have a large surface area.)	97
3.29	Photograph showing the approximate agreement between the regular mesh and the edge of the stamping produced from a rectangular blank	98
3.30	(a) Photograph of an automotive inner deck-lid panel showing positions of peak strain for comparison (b) Contours of effective strains obtained from measurement of 0.2 in diameter grid circles on the panel (c) Contours of effective strains computed from the remapped regular mesh illustrated in Fig. 3.28 (region of points of peak strain, A to D are given in (a))	99
4.1	Diagram illustrating the deformation of the vector $d\bar{x}$	110
4.2	Schematic illustration of two reference frames	118
4.3	Finite simple shear deformation (a) The undeformed unit cube (b) The deformed element (c) The deformed configuration of (b) in two-dimensional space	134
4.4	Diagram illustrating the variation of non-dimensional stresses with respect to the shear displacement S (a) σ_{11}/μ versus S (b) σ_{12}/μ versus S	139
A.1	Mohr circle representation of finite strain	147
B.1	The strain at A is the mean average of sum of strains of the surrounding elements connected to node A	150

	<u>Page</u>	
B.2	A flow chart of contour developments	151
B.3	Diagram showing a contour line formed by straight segments between points	152
C.1	Schematic of one-quarter of the hemispherical shell under consideration	161
C.2	A typical thickness strain distribution of the hemisphere in Fig. C.1	161
C.3	Arrays of quadrilateral elements on the surface of part of the hemisphere	164
C.4	The "correct" analytical map of the shell surface in Fig. C.3	164
C.5	The resulting blank obtained from the assumed proportional deformation of Fig. C.3	166
C.6	The resulting map Fig. C.3 showing collapse of elements occurs with the intersection method	166
C.7	"Constant area" transformation of the hemispherical shell on a flat blank	166
C.8	An artificial mesh as shown is constructed over the surface of the hemisphere	168
C.9	The "correct" analytical transformation of the mesh in Fig. C.8 on a plane	168
C.10	The resulting map of the surface occurred with the area criterion showing effect of element geometry	168
C.11	A regular grid is superimposed on the developed blank shape	172
C.12	The resulting polyhedron established on the hemisphere surface using the regular grid in C.11	172
C.13	Diagram showing surface adjustment in a specified direction applied to the blank in Fig. C.4	173
C.14	Diagram showing local distortion of a region within the blank in Fig. C.4	173
D.1(a)-(g)	Flow charts indicating the complete logical development of the mapping strategy	175

CHAPTER 1

INTRODUCTION

1.1 Preamble

With the rapid advance in the technology of high speed computers and the development of more flexible and reliable numerical techniques, a solution to many complex metal forming problems can now be realised. However, the ability to analyse practical sheet metal forming operations has not developed as rapidly as was perhaps first envisaged. A number of researchers have created mathematical models which describe, by a sequence of discrete steps, the manner in which a component is formed; the calculations are continued until the final shape is realised or until some imposed failure criterion - based on wrinkling, localized necking, unacceptable thinning and the like - is met. If the model shows that the part cannot be formed, the input conditions are changed and the calculations repeated.

In principle, this approach should facilitate an understanding of the forming process and aid in finding the blank shape and the design of the tools and dies. Some success has been achieved when dealing with parts of simple geometry, particularly axi-symmetric components [1], but the approach is less satisfactory when more complicated shapes are considered. This stems in part from the imprecise knowledge of the initial and subsequent boundary conditions, interfacial frictional conditions between the tooling and the workpiece, rheological behaviour

of the material as a function of strain, strain rate and temperature, and the mechanisms which initiate bifurcations such as localized necks. Furthermore, when using large finite elements codes, the computational time is long and costs are high. Consequently, with the present generation of computers, the step-by-step approach is still not sufficiently well developed to permit its embodiment into a computer-aided design package whereby sheet metal forming operations are studied and the tooling developed through an interactive graphics terminal.

In sheet metal forming industries, a sheet stamping is usually produced by a combination of drawing and stretching. Having decided upon the basic form of the tooling and dies, there is usually a series of press trials which decide the level of clamping at the draw ring and the location of draw beads in order to produce a successful pressing. It will be appreciated that there is a complicated interplay of die geometry, lubrication conditions, and the properties of the sheet material which govern this process, i.e. the clamping has to be sufficient to offer resistance to the material and so prevent wrinkling or buckling, but at the same time permit the materials to "draw-in". If the material is over-restrained, the material will not draw-in and all the deformation will take place by stretching; only very shallow parts can be formed by this technique. Although it is customary to use an initial sheet metal blank of simple geometric shapes, rectangular or circular, these are usually not the optimum shapes. The blank shape can promote or inhibit the inward flow of material in certain parts of the flange, and the amount of scrap which arises in the trim operation can

be minimized with a correctly designed blank shape.

Quite often for simple shapes, a number of geometric and semi-empirical relations found in sheet metal texts are employed. However, many sheet metal components are comprised of highly irregular geometries which cannot be represented accurately by simple mathematical expressions. For these parts, manual measurements and the experience of the designer become important in establishing a suitable blank shape for a given component. The process of finding the size and shape for cutting the initial sheet or blank in order to make a given stamping is called blank development. For complicated shapes, the design of dies for sheet metal forming operations has relied more on technical expertise than detailed analysis. The designer often considers the die to be comprised of modules of simple geometric shapes, it is imagined that these analytical elements are combined together to form the entire surface geometry of the tool and line lengths across different sections of the die are examined carefully. Although the design methods may appear crude, it will be recognized that the tooling can be (and often is) very complex, and a successful pressing demonstrates the skill of the designer.

In many major automotive companies, die designers have developed models which permit the process to be displayed in a computer graphics systems. It is a useful aid to the designer who may, during the course of the design process, interact and instruct the computer to modify or select suitable process parameters in order to establish the best tooling geometry.

In the present work, results are presented of a new method for assessing the shape of a blank for a sheet metal pressing. The technique is one of geometric modelling and is intended as a computer aid for the experienced tool designer. It is the first step in an entirely different approach to computer-aided blank development. The work does not aim to provide, in a mathematical sense, a solution to the forming problem but rather it is a computer aid for the tool designer in dealing with some traditional geometric problems. It is hoped that this study will provide a good starting point for subsequent analyses, such that an understanding, although crude, of the sheet forming process is obtained. Some features which are unique in the proposed method are perhaps worth mentioning and these are summarized below:

- (1) The technique provides a more efficient way of utilizing the skill and experience of the designer, it allows him to interact with the computer graphics system. In the analysis, the designer specifies the most desirable end result of the forming process. This can be done essentially in geometrical terms. The method utilizes a computer technique for finding a suitable blank shape and a strain distribution, which are geometrically compatible with the constraints imposed by the designer. Forces, equilibrium and mechanical properties of the sheet are not accounted for and hence the resulting strain distribution is kinematically acceptable but not necessarily physically possible. Only geometric constraints are satisfied in the model. This is where judgement and practical expertise of the designer is required in

order to achieve a successful design.

- (ii) The surface geometry of the component is described by flat triangular elements, the analysis deals only with these elements and the surface to which it must conform after the stamping operation is completed. The only restriction is that continuity of the elements must be maintained. Overlapping of elements is a very undesirable feature however, overlapping during the initial mapping operation may offer the designer some information about regions in the stamping which are difficult to form. The mapping process is not an incremental one.

1.2 Scope of the Research

An examination of how complicated processes in other branches of engineering are analysed has suggested that simplified models of forming processes are useful even for parts of complex geometry [1]. Various situations are presented herein and a number of idealizations which are employed in the present work are outlined below.

1.2.1 Ideal Finite Deformation Processes

Strain in a sheet metal stamping is typically evaluated from measurements of a grid, usually an array of circles, which has been marked on the surface of the blank prior to forming. The grid method is a surface phenomenon and the strain determination is reduced to a two-dimensional problem. Any measurements taken on the initial and final grid configurations only, without knowing the deformation path, are

insufficient to determine the strains precisely. Nevertheless, in practice, strains are determined by such a technique; and when grid circles are employed it is further assumed that they deform into ellipses. The deformation process which transforms circles to ellipses and straight lines to straight lines is known as homogeneous deformation, but such a mode does not necessarily define the straining path. Under such a deformation mode strain paths can be divided into two main types: those where an initially orthogonal pair of principal axes remain orthogonal throughout the deformation and those where they do not. The same change in shape can be achieved by either type of straining path, the distinction between each straining mode is discussed herein and the results are presented in simple terms.

Emphasis is placed on pure homogeneous deformation, whereby the principal axes do not rotate with respect to the material element. Under this ideal deformation mode, a very simple formulation of large strains is possible. This technique has been applied to the assessment of surface strain on an industrial sheet metal stamping. The details are described in Chapter 2.

In pure homogeneous deformation, an appropriate strain measure in such processes is that of logarithmic strain. Furthermore, its material derivative equals the rate of deformation tensor. In homogeneous processes, the deformation gradient tensor is unsymmetric, and there is no triad (the principal axes) which remains orthogonal throughout. This can lead to a description of the actual deformation in terms of the polar decomposition theorem. The material derivative of the tensor

logarithm is no longer simply related to the rate of deformation tensor, and this is exemplified in Chapter 4. As a result of material rotation, the stress components will vary, and constitutive equations which involve stress rate must be formulated to compensate for the rotation. A number of objective stress rates are examined herein and employed in a constitutive equation describing a hypoelastic solid. The effect of stress rate on the evaluation of stresses in the deforming solid is demonstrated in Chapter 4 for the case when the body undergoes simple (rectilinear) shear.

1.2.2 The Ideal Sheet Metal

In some automotive industries, such as the Ford Motor Company, the tooling for automobile body panels is designed by experienced tool designers with the assistance of computer graphics. The designer can find the deformed shape of a blank by fitting the desired component with a developable surface. However, in stamping operations, the sheet is transformed from a plane to a non-developable surface. Ideally this should be done by pure distortion rather than by thinning. Hence, the ideal sheet material should have an infinite strength or resistance to deformation in the through-thickness direction.

No real sheet performs in this fashion, but it is remarkable that one of the most formable materials, namely drawing quality rimmed steel, has some of these characteristics. The resistance to through-thickness deformation is measured by the extent to which the plastic strain ratio or r -value i.e., the ratio of width-to-thickness strains in a tensile

test, exceeds unity. The r -value for rimmed steel is not infinity as in the ideal material, but it is at least substantially greater than unity.

The analysis of forming of the ideal sheet can be considered as an essentially geometric problem. If there is no thinning elements would deform by shear without change in area. Many of the traditional die design procedures indicate that they are based on a similar assumption, consequently such a constant area hypothesis may provide a useful basis for tool and blank design. The problem is that the geometrical analysis required can only be done manually for quite simple cases. It seemed therefore a very useful computer aid would be to design a mapping system which could transform elements from a flat sheet to a given surface, permitting each element to deform without change in area and ensuring that continuity is satisfied and each element fitted together without gaps or overlapping. The basis of this computer-aided design system is described in Chapter 3.

CHAPTER 2

THE ANALYSIS OF FINITE STRAINS IN METALFORMING

2.1 Introduction

In metal deformation processes involving finite (plastic) strains the material properties depend upon the current state of strain which itself is a function of the deformation history. It is customary to attempt an integration over the strain path, but in general the integral cannot be evaluated explicitly. Furthermore it is usually impractical to measure three dimensional strains, for instance those arising in a forging operation. In sheet metal forming process most strain measurements are based on grid markings on a free surface. If the grid is measured after a small increment in deformation the strain increment is, in general, easily determined. The mode of deformation will dictate how readily the strain increment in each successive deformation step can be evaluated from the distorted grid, and how easily the strain increments can be integrated. In many instances, however, it is either too time consuming or difficult practically, to make incremental measurements and only measurements of the initial and final shape of the grid are made.

It is often assumed that at a point in the sheet metal stamping one principal axis of plastic strain increment is normal to the material surface, with the other two principal directions lying in the plane of the sheet. The well known grid-circle technique, for the determination

of strains in sheet metal pressings, is based upon this hypothesis. The method also invokes the additional assumption that a grid circle, etched or printed onto an undeformed blank, is transformed into an ellipse on the surface of the pressing. By measuring the major and minor diameter of the deformed ellipse the principal surface strains can be determined. Not every element deforms in this manner, although over a large portion of the surface circles do appear to have been transformed into the shape of an egg when viewed by the naked eye or through a toolmakers microscope. In general the deformation path of an element in an industrial pressing is not known precisely. How well the measurements of a grid circle reflect the actual strain is a matter of conjecture, but it will depend upon the complexity of the strain path. In the presence of high strain gradients the grid circle method is inadequate, a grid circle will undergo severe distortion and no longer resemble an ellipse after deformation. The grid circle technique reduces the strain determination to a two dimensional problem, since in order to obtain a reliable measure of the distortion the deformed ellipse must lie on a relatively flat surface. In what follows attention is devoted to strains in two dimensions, and a distinction is drawn between two important straining modes.

The deformation process which transforms straight lines into straight lines and circles into ellipses is usually referred to as homogeneous deformation. As already mentioned, under this general mode there is not an orthogonal line pair which remains orthogonal through the deformation; a classical example is simple shear. When the

principal axes are fixed within a material element the deformation is termed pure homogeneous strain, which is exemplified by the pure shear mode. Note the principal axes only remain fixed in direction, all other line elements would rotate. It is well known [2] that the final shape of a material element following a prescribed homogeneous strain, can also be realized by imposing a pure homogeneous mode followed by a rigid body rotation. This poses the question of equivalence of the strain paths. It is the belief of the author that the two modes are not the same. However, in standard texts on continuum mechanics dealing with finite strain [3,4], the deployment of classical finite strain tensors would lead to the conclusion of equivalence since the same strain components would be evaluated in each case.

In the present chapter the two straining modes are discussed and the theories of which are presented without a detailed development. For more details the readers are referred to Refs. [5,6,7]. In presenting the analysis the deformation of a square or quadrilateral element is considered, with a view to using these types of grids on sheet metal pressings for strain determination. This does not overcome certain problems also encountered with the grid circle technique, such as the presence of strain gradients. However, the uncertainty of assessing the major and minor axis of an ellipse is eliminated, the location and digitization of nodal points is accomplished more readily and an improved averaging of the strain within an element becomes available. Emphasis is placed on the pure homogeneous mode since it leads to a simpler finite strain tensor and this technique is applied to the

analysis of strain of an industrial stamping.

2.2 Theoretical Considerations

2.2.1 Finite Homogeneous Deformation

In what follows the mathematical fundamentals of homogeneous deformation is presented. In Appendix A the complete analogy between the components of a finite strain tensor (for pure homogeneous deformation) and those of the classical infinitesimal strain tensor, is discussed at greater length.

Homogeneous deformation in two dimensions is illustrated in Figure 2.1, which shows the initial and deformed state of a square grid. To relate the initial and final shapes it is mathematically convenient to consider reference coordinate axes which are fixed in space, in Figure 2.1 the reference axes have been arbitrarily selected to coincide with the sides of the undeformed square grid. When using image analysis techniques it would be usual, although not essential to employ a fixed set of measuring axes. With reference to Figure 2.1, the new coordinates (x,y) of a particle are a linear function of the initial coordinates, say (X_0, Y_0) , and can be expressed as

$$\begin{aligned} x &= F_{11} X_0 + F_{12} Y_0 \\ y &= F_{21} X_0 + F_{22} Y_0 \end{aligned} \quad (2.1)$$

or

$$\bar{x} = \underline{F} \cdot \bar{X}_0 \quad (2.2)$$

where \bar{X}_0 is a vector in the undeformed configuration and is mapped into

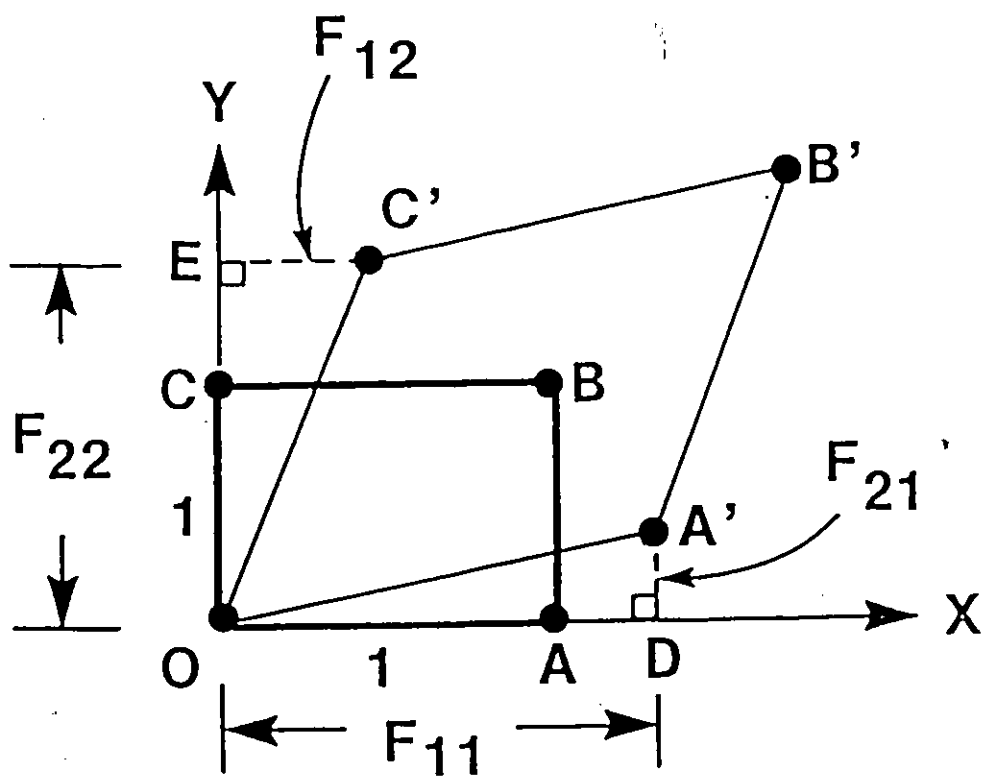


Figure 2.1 represents the homogeneous deformation of the initial square OABC.

\bar{x} . In general, $F_{12} \neq F_{21}$. The deformation gradient tensor, \underline{F} depends upon the basis selected, but the deformation tensor, \underline{C} , where

$$\underline{C} = \underline{F}^T \cdot \underline{F} \quad (2.3)$$

does not. The tensor \underline{C} is symmetric and its eigenvalues are usually referred to as the principal stretch values squared. It is considered that the use of the word principal may be misleading, since homogeneous deformation does not provide a set of orthogonal axes which remain orthogonal throughout the deformation.

Equation (2.2) is the solution of the homogeneous velocity field

$$\bar{v}(x) = \underline{L} \cdot \bar{x} \quad (2.4)$$

where \underline{L} is the spatial velocity gradient tensor and can be expressed as

$$\underline{L} = \dot{\underline{F}} \cdot \underline{F}^{-1} \quad (2.5)$$

where

$$\dot{\underline{F}} = \begin{pmatrix} \dot{F}_{11} & \dot{F}_{12} \\ \dot{F}_{21} & \dot{F}_{22} \end{pmatrix}. \quad (2.6)$$

For a homogeneous velocity field the components of \underline{L} are constants hence it is proposed that

$$\underline{L}^* = \int \underline{L} dt = \ln(\underline{F}), \quad (2.7)$$

and the right hand side of (2.7) can be expressed as

$$\ln(\underline{F}) = \underline{P} \cdot (\ln \underline{\lambda}) \cdot \underline{P}^{-1} \quad (2.8)$$

where

$$\underline{\lambda} = \begin{pmatrix} \lambda_1 & 0 \\ 0 & \lambda_2 \end{pmatrix} \quad (2.9)$$

is the matrix of the eigenvalues of \underline{F} and \underline{P} is the matrix of the associated eigenvectors.

The eigenvalues of \underline{F} can be expressed as

$$\lambda_1, \lambda_2 = \frac{F_{11} + F_{22}}{2} \pm \sqrt{\left(\frac{F_{11} - F_{22}}{2}\right)^2 + F_{12} F_{21}} \quad (2.10)$$

and

$$\underline{P} = \begin{bmatrix} F_{12}/(\lambda_1 - F_{11}) & F_{12}/(\lambda_2 - F_{11}) \\ 1 & 1 \end{bmatrix} \quad (2.11)$$

From (2.5) to (2.9), the components of $\underline{L}^{\#}$ can be expressed as

$$\begin{aligned} L_{11}^{\#} &= \frac{1}{2} \ln(\lambda_1 \lambda_2) + \frac{F_{11} - F_{22}}{2(\lambda_1 - \lambda_2)} \ln(\lambda_1/\lambda_2) \\ L_{22}^{\#} &= \frac{1}{2} \ln(\lambda_1 \lambda_2) - \frac{F_{11} - F_{22}}{2(\lambda_1 - \lambda_2)} \ln(\lambda_1/\lambda_2) \end{aligned} \quad (2.12)$$

$$L_{12}^{\#} = \frac{F_{12}}{(\lambda_1 - \lambda_2)} \ln(\lambda_1/\lambda_2)$$

$$L_{21}^{\#} = \frac{F_{21}}{(\lambda_1 - \lambda_2)} \ln(\lambda_1/\lambda_2) ..$$

Note that the eigenvalues of \underline{F} are not necessarily real and there is some advantage in expressing the components of \underline{L}^* in terms of trigonometric functions, as was demonstrated by Bredendick [8]. A detailed account of the theory can be found in Ref. [6].

2.2.2 Pure Homogeneous Deformation

As already mentioned, the tensor \underline{F} need not be symmetric but if it is we have the particular case of pure homogeneous deformation. Hence when \underline{F} is symmetric, the principal values and the orientation can be found in the usual way. The components of \underline{F} can be regarded as strain components, note $F_{12} = F_{21}$ can be associated with the shear strain and $(F_{11}-1)$ and $(F_{22}-1)$ with the direct strain. Actually F_{11} and F_{22} represent stretch ratios, i.e. $\frac{\text{final length}}{\text{initial length}}$. The principal values (eigenvalues) of \underline{F} are also stretch ratios, say λ_1 and λ_2 , which can be determined from equation (2.10). The orientation of the principal axes is obtained from

$$\tan 2\theta = \frac{2F_{12}}{F_{11} - F_{22}} \quad (2.13)$$

The principal logarithmic (or natural) surface strains, say ϵ_1 and ϵ_2 , are determined from

$$\epsilon_{1,2} = \ln(\lambda_{1,2}) \quad (2.14)$$

while the third principal strain, ϵ_3 , is furnished by the incompress-

ibility assumption

$$\epsilon_1 + \epsilon_2 + \epsilon_3 = 0. \quad (2.15)$$

The representative or equivalent strain, $\bar{\epsilon}$, is given by

$$\bar{\epsilon} = \sqrt{\frac{2}{3} (\epsilon_1^2 + \epsilon_2^2 + \epsilon_3^2)}. \quad (2.16)$$

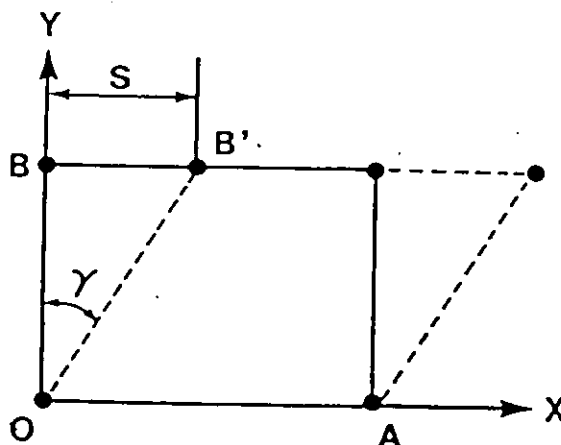
Note also that for a symmetric \underline{F} the components of (2.12) are given by the standard transformation expression

$$L_{ij}^* = C_{ip} C_{jp} \ln \lambda_{pp}, \quad (2.17)$$

where the C_{ip} represent direction cosines, derivable from (2.13).

To further highlight the distinction between homogeneous and pure homogeneous deformation the shape change produced in the simple (rectilinear) shear process will be discussed. Figure 2.2(a) shows the simple shear mode, where the initially orthogonal line pair OA and OB have been deformed to OA and OB'. The simple shear process is a homogeneous deformation process and the deformation gradient tensor, \underline{F} , is unsymmetric with components

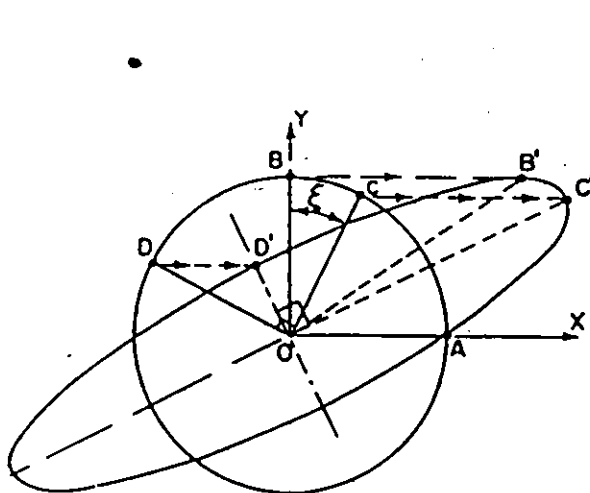
$$\underline{F} = \begin{pmatrix} 1 & S \\ 0 & 1 \end{pmatrix}, \quad (2.18)$$



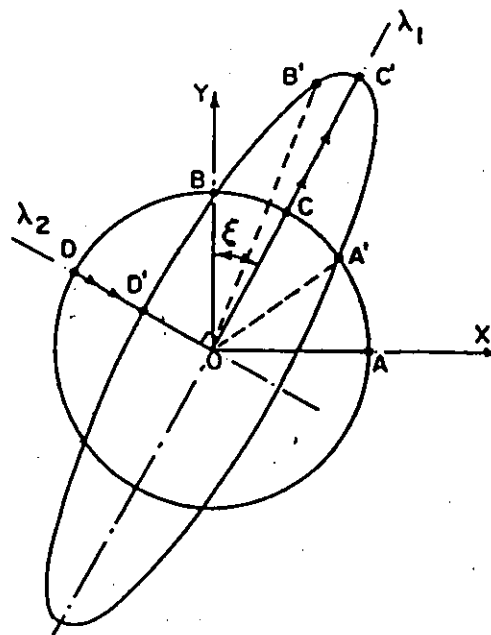
(a)

HOMOGENEOUS DEFORMATION
SIMPLE SHEAR

PURE HOMOGENEOUS DEFORMATION
PRINCIPAL AXES λ_1 AND λ_2 FIXED



(b)



(c)

Figure 2.2: (a) Simple shear mode.
 (b) A circle is deformed into an ellipse by homogeneous deformation.
 (c) The same shape change in (b) can be achieved by pure homogeneous deformation.

where S is the shear displacement of point B . Figure 2.2(a) is redrawn in greater detail in Fig. 2.2(b), the latter diagram also indicates a circle deformed into an ellipse. The shape changes exhibited in Fig. 2.2(b) can also be realised by a pure homogeneous mode and this is illustrated in Fig. 2.2(c). The principal axes are denoted by OD and OC ; these axes remain fixed in Fig. 2.2(c). Upon deformation D moves to D' and C to C' while all other line elements rotate e.g. OB moves to OB' and OA moves to OA' . Note that point A does not move in a circular arc since OA changes in length during the deformation. However it is of the same length (say unit length) in both the initial and final position OA' . For a shear displacement S the principal stretch ratios in Fig. 2.2(c) are given by

$$\lambda_1, \lambda_2 = \frac{1}{2} (S^2 + 4)^{1/2} \pm \frac{S}{2}, \quad (2.19)$$

and the orientation of the principal axes can be determined from (2.13) where

$$\tan 2\theta = \tan 2(90-\xi) = -\tan 2\xi = -\frac{2}{S}, \quad (2.20)$$

or

$$\cot \xi = \frac{S}{2}. \quad (2.21)$$

Note that the deformation gradient tensor, say \tilde{U} , producing the shape change of Fig. 2.2(c) is not given by (2.18), but rather

$$\tilde{U} = \frac{1}{(S^2 + 4)^{1/2}} \begin{bmatrix} 2 & S \\ S & 2 + S^2 \end{bmatrix}. \quad (2.22)$$

As already remarked the deformed ellipse in Figs. 2.2(b) and (c) are

identical in shape as are the configurations B'OA in Fig. 2.2(b) and B'OA' in Fig. 2.2(c). The initial orthogonal line pair, OD and OC, are identical in each diagram. They remain orthogonal in Fig. 2.2(c) since they are aligned with the principal axes. This is not the case in Fig. 2.2(b), and although the line pair start and finish orthogonal they do not remain orthogonal throughout. Hence the distinction between the deformation modes of Figs. 2.2(b) and (c) is apparent, the initial and final configurations are the same but all intermediate configurations are distinct. If the deformation modes are intrinsically different, how is this difference made manifest? Sowerby and Chakravarti [6] have demonstrated that the equivalent strain is minimised when the shape change is achieved by a pure homogeneous deformation mode. As shown in Ref. [5] the equivalent strain for the simple shear process of Fig. 2.2(b) is

$$\bar{\epsilon} = S / \sqrt{3}, \quad (2.23)$$

while for the pure homogeneous mode of Fig. 2.2(c) it is

$$\bar{\epsilon}_{P.H.} = \frac{2}{\sqrt{3}} \ln \lambda_1, \quad (2.24)$$

where λ_1 is given by (2.19). Equation (2.24) always result in a lower value than (2.23) and the difference increases with increasing S . However in practical sheet forming operations the difference may not be large. For example, a shear displacement of $S = 1.5$ constitutes a large deformation in sheet forming, and yet the difference between (2.23) and

(2.24) is only about 10 per cent. Nevertheless it has been the purpose of this section to exemplify the differences between homogeneous and pure homogeneous deformation.

As is well known it is always possible to create a symmetric tensor out of the unsymmetric deformation gradient tensor of (2.18), which characterises the simple shear mode. One way is the creation of the deformation tensor \underline{C} , defined in (2.3). The eigenvalues of this tensor are

$$\lambda_1^2 = \left(\frac{S^2}{2} + 1\right) + \frac{S}{2} (S^2 + 4)^{1/2}$$

$$\lambda_2^2 = \left(\frac{S^2}{2} + 1\right) - \frac{S}{2} (S^2 + 4)^{1/2}$$
(2.25)

which are the squares of the quantities given in (2.19). Even though the use of the deformation tensor \underline{C} results in the same eigenvalues as the pure stretch tensor \underline{U} , eqn. (2.22), the deformation modes are different as demonstrated above. Furthermore the use of the \underline{C} tensor would not reveal the difference in the equivalent strain accumulated in each deformation process.

2.3 Strain Analysis of an Industrial Stamping

2.3.1 General Comments

Strain in a sheet metal stamping is typically evaluated from measurements of a grid, which has been marked on the surface of an undeformed blank. The technique is widely employed in sheet metal stamping plants, and informs the tool designer or die-setter of the

location of the critically strained regions within the pressing. There is no restriction on the geometry of a grid which can be marked on a blank, but an array of circles is often adopted. In evaluating the principal strains it is implicit in the grid circle technique that straining occurs by pure homogeneous deformation, whereby circles are transformed into ellipses and measurements taken of the major and minor axes determine the principal surface strains. In regions of high strain gradients, measurements become erroneous since a circle may be deformed into an irregular, complex shape. Nevertheless, the grid circle provides a convenient way of assessing the strain at selected points within a stamping, assuming the strain gradients are not too severe. If the objective is the determination of the strain distribution over the entire surface of the stamping, the grid circle technique can be very time consuming, and an array of square or rectangular grids is more convenient. Coordinate measuring machines allow a stylus to be moved over the surface of the pressing, and the nodes of a square grid facilitate the location of points in space and the digitizing of their coordinates. However, the square grid does not obviate the problems associated with high strain gradients, which could cause the grid to be deformed into a curvilinear quadrilateral. The nodal point measures would still permit some assessment, albeit a highly inaccurate one, of the strain; but even such a crude estimate might not be readily available from a distorted grid circle.

In the present Chapter, the surface strain distribution is determined for two identical industrial stampings from measurements of

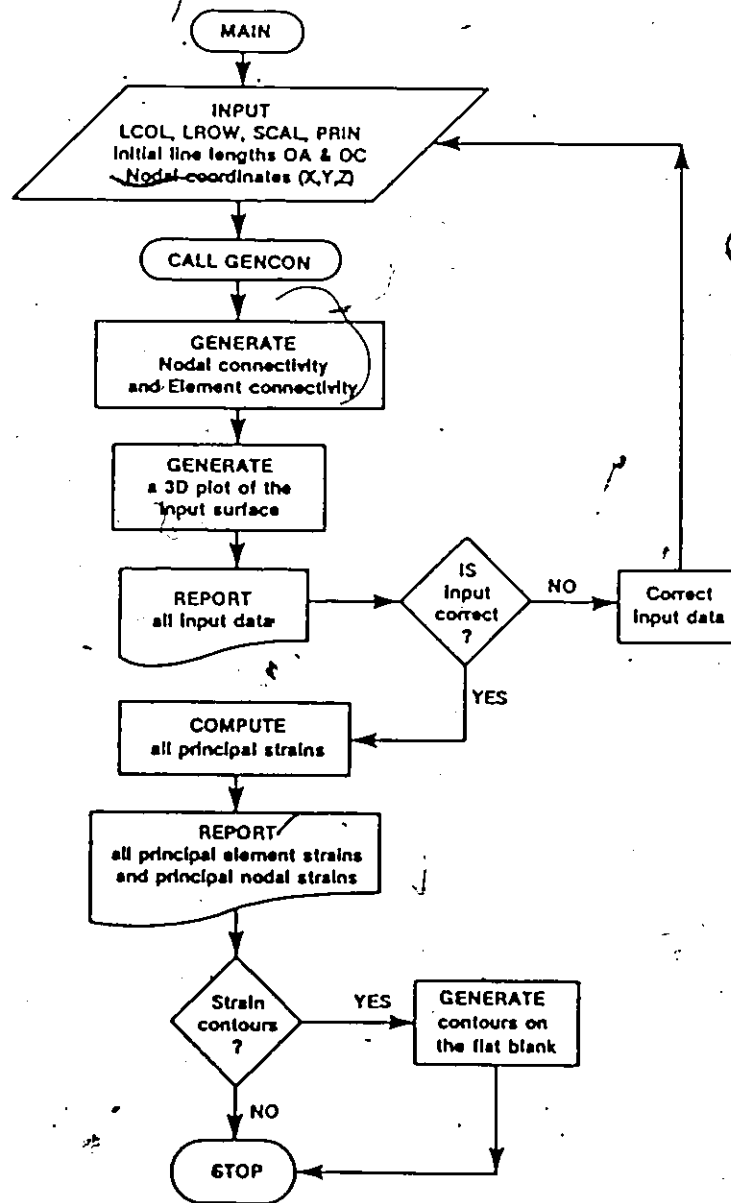


Figure 2.3: A flow diagram indicating the complete logistics of the strain program.



Figure 2.4: Photograph of a typical automobile pressing which was scribed with an initially square grid.

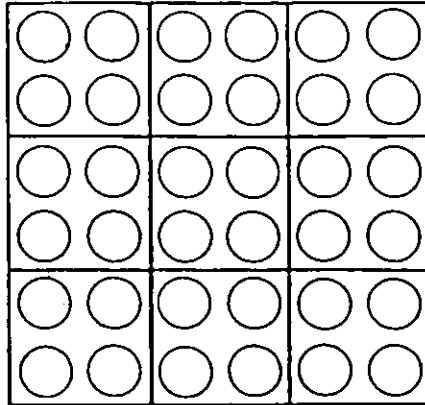


Figure 2.5: A sample of a typical stencil of circle grid pattern.

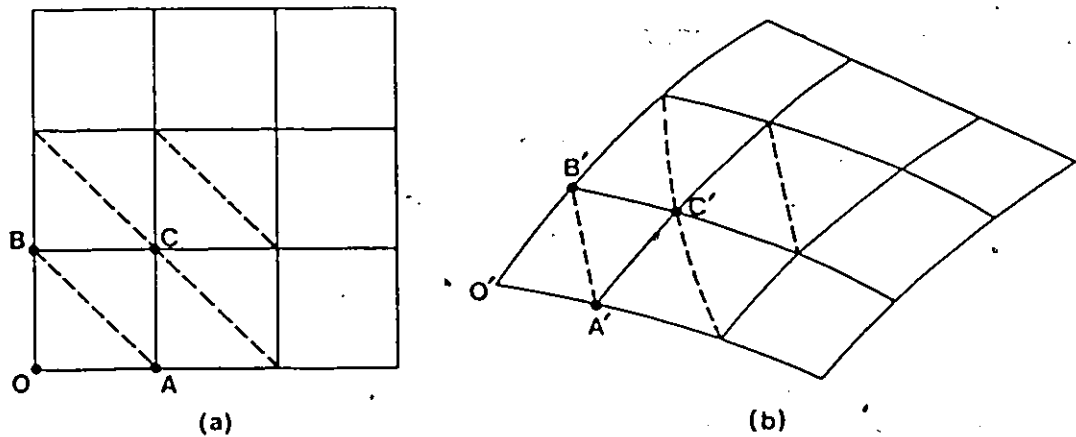


Figure 2.6: (a) Initially undeformed square elements represented by triangular facets.
 (b) The deformed configuration of (a).

distorted square and circular grids. A computer program has been developed, for the assessment of the magnitude and direction of the principal finite strains from measurements made on a deformed pair of lines. The technique is based on the work of Ref. [5] which has been summarized in the preceding section and also discussed in Appendix A. The determination of the distribution of natural strains over the entire area of a deformed sheet is a possible application of this program. Details of the programming technique, user input variables, operating procedures and the like are not presented here but they can be found in Ref. [9]. A flow diagram indicating the philosophy of the program solution is presented in Figure 2.3.

2.3.2 Experimental Strain Determination

A photograph of the autobody inner panel is shown in Figure 2.4, the left and right hand sides of the panel are symmetric. Two identical panels were used to assess the resulting strain distribution. On one panel an array of lines had been scribed, prior to deformation, to form a network of squares of 1/2 in (12.7 mm) side. While on the second blank a grid of 1/2 in (12.7 mm) squares and 0.2 in (= 5 mm) diameter circles had been electrochemically etched. This grid pattern is shown in Figure 2.5. Both grids covered only part of the panel, as indicated in Figure 2.4. The full depth of the panel was gridded, corresponding to about 70 horizontal lines at 1/2 in intervals; while the region extending from the extreme left hand side of the panel was comprised of about 35 vertical lines at 1/2 in pitch. Thus approximately 2500 nodes

were digitized for the scribed square grid, and a like number of circles were measured on the electro-etched grid. It will be noticed that the grid patterns did embrace the most severely distorted regions of the panel. The gridded domain was divided into two regions along a line OX, see Figure 2.4, which is about half-way down the panel. The subdivision was introduced for the convenience of plotting the strain contours, since there was insufficient capacity with our equipment to handle all the nodes of the entire mesh on a single plot. The basic theory of the contour plotting routine is outlined in Appendix B.

The measurement of the vertices, of the deformed scribed squares, was performed manually with the aid of a milling machine. Thus each deformed square is now represented as four nodal points each lying on the surface of the panel. To arrive at an estimate of the strain, the undeformed square grid is assumed to be divided across a diagonal as shown in Figure 2.6(a). After deformation, a triangular region like OAB in Figure 2.6(a) would form a small flat facet (at least that is the only information the nodal points such as O'A'B' would reveal, see Figure 2.6(b)) on the deformed surface. The strain within the triangle can be determined from a knowledge of the location of the deformed nodes and the side length of the undeformed square. The technique has already been described in section 2.2.2, and is based on the assumption that the straining has occurred by pure homogeneous deformation. The analysis furnishes the magnitude and orientation of the principal surface strains (either natural or engineering) within the triangle, the assumption of incompressibility will provide the natural thickness strain. The

procedure is repeated for each successive triangle. To facilitate the plotting of the strain contours, we execute this in the flat plane using the undeformed grid as a reference. A typical boundary node such as A or B, in Figure 2.6(a), forms a vertex for three triangles; while at an interior node like C six triangles intersect. Therefore when determining the strain at a particular node, an unweighted average of the strain within each triangle is computed. Once a strain value is assigned to a nodal point, the plotting routine executes linear interpolation between the nodes and can provide strain contours at any desired level. Any quantity, such as thickness strain, largest surface strain, equivalent strain etc., can be plotted. In the present work contours of equivalent strain are evaluated at 5 percent intervals. A typical result for the upper half of the panel is shown in Figure 2.7. The diagram, designated Figure 2.7(a), is a computer plot of the surface of the panel as determined from the nodal coordinates of the deformed squares; while Figure 2.7(b) shows strain contours in the undeformed plane. Similarly, the surface strains for the lower half of the inner panel shown in Figure 2.4 are analysed in the like manner. The diagram of Figure 2.8(a) is the computer plot of the lower portion of the panel determined from the deformed nodal points and Figure 2.8(b) is the resulting contours of equivalent strain for the deformed portion of Figure 2.8(a).

It was apparent from the two panels under investigation that there was some misalignment between the scribed square grid and the electro-etched grid pattern. The latter had been marked on the panel

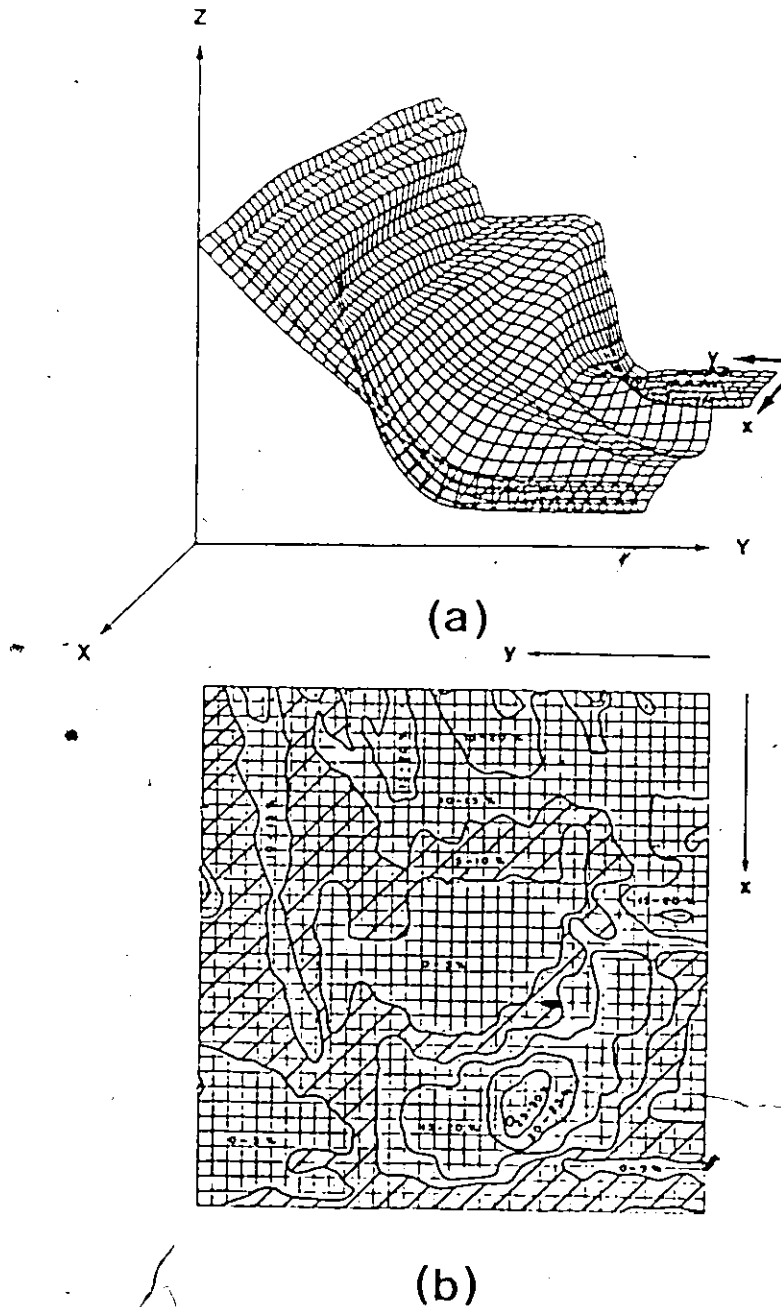


Figure 2.7: Square grid analysis
 (a) A computer plot of the upper portion of the stamping in Fig. 2.4.
 (b) Strain contours are plotted in the undeformed blank.

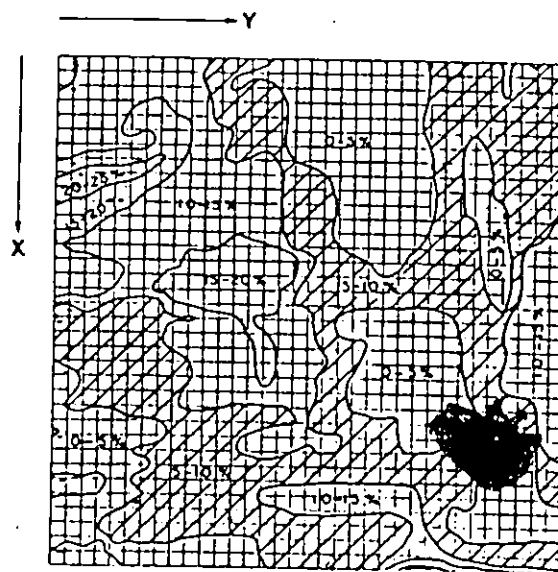
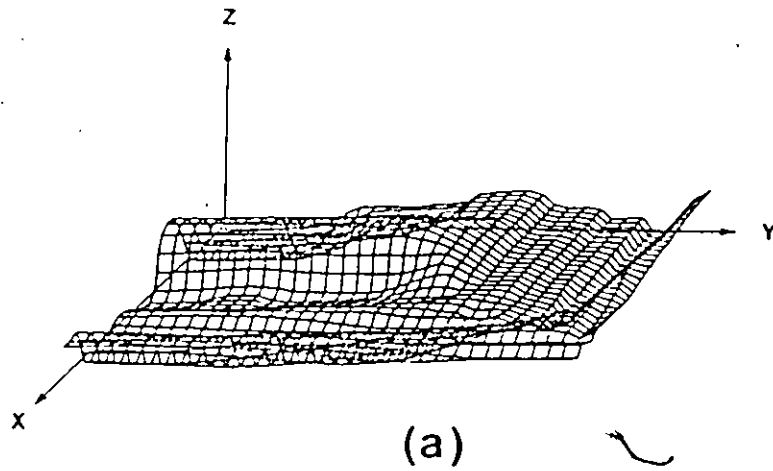


Figure 2.8: Square grid analysis
 (a) A mesh of the lower half of the panel in Fig. 2.4.
 (b) Strain contours of (a) on the flat plane.

using a stencil to form contiguous patches, this had also resulted in a slight mismatch so that there was not a continuous chequer board pattern to the squares which circumscribed the grid circles (see Figure 2.5). If the alignment had been better then the electro-etched pattern would have permitted the nodes of the squares to be digitized as well as providing the strain readings from the deformed circles. In order to provide identical reference points on each panel -- to facilitate the plotting of the strain contours -- the two panels were placed on top of each other and small holes were drilled through every other node of the scribed grid into the electro-etched panel below. When plotting the strain contours, calculated from the grid circle measurements, the strain assigned to a node, i.e. the drilled hole, is in general the average value of the strain in the four nearest grid circles. For the sake of convenience, the computer plots of the deformed mesh of the panel shown in Figure 2.4 are repeated in Figures 2.9(a) and 2.10(a). The resulting equivalent strain distributions, determined from measurements made of the major and minor axes of the deformed circles, are illustrated in Figures 2.9(b) and 2.10(b). These diagrams show the strain contours of the upper and lower portion of the panel respectively. The major and minor strains obtained using the square grid and the circle grid technique are plotted on a strain space, i.e. with the principal surface strains ϵ_1 and ϵ_2 as the co-ordinate axes, shown in Figure 2.11(a) and 2.11(b) respectively. The well known forming limit diagram (F.L.D.) [10] is constructed in ϵ_1 - ϵ_2 space, and therefore theoretically predicted or experimentally determined (from

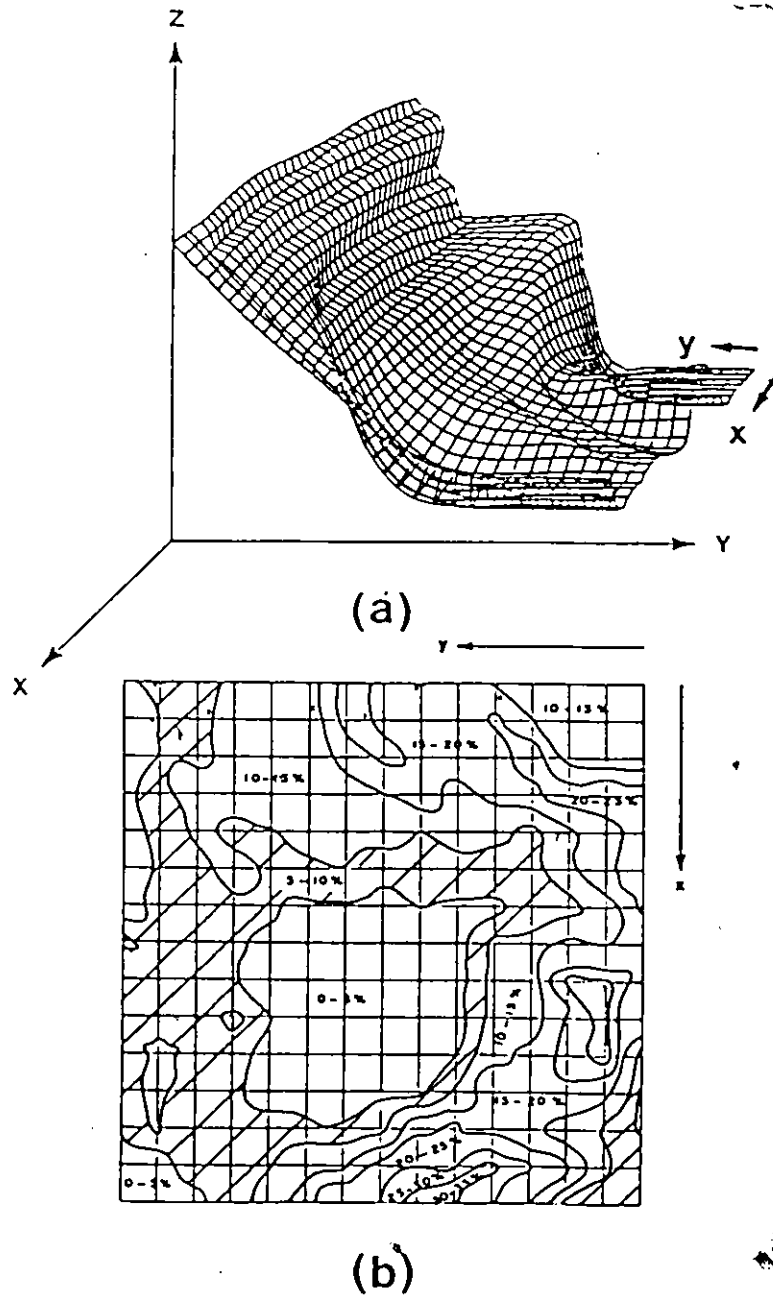
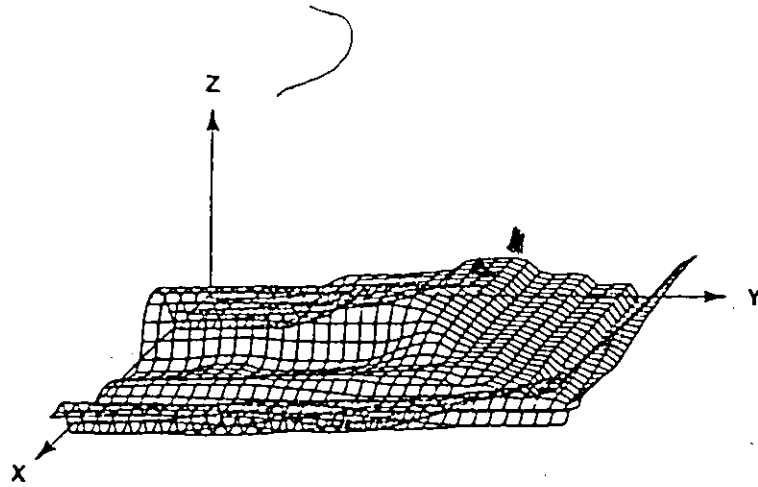
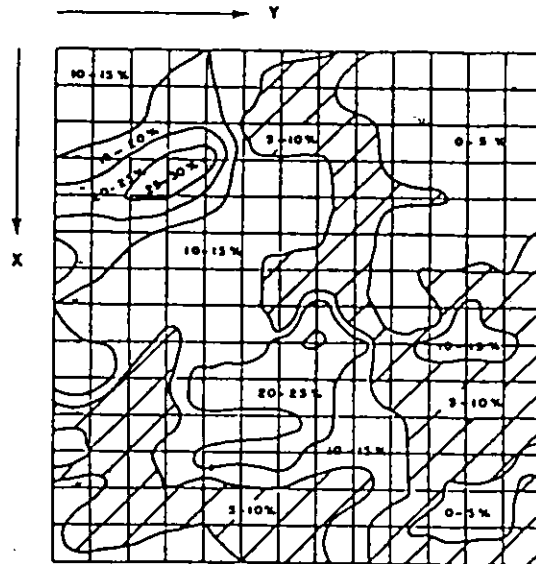


Figure 2.9: Circle grid technique
 (a) A computer plot of the upper part of the panel.
 (b) Resulting strain contours are plotted on the undeformed sheet.



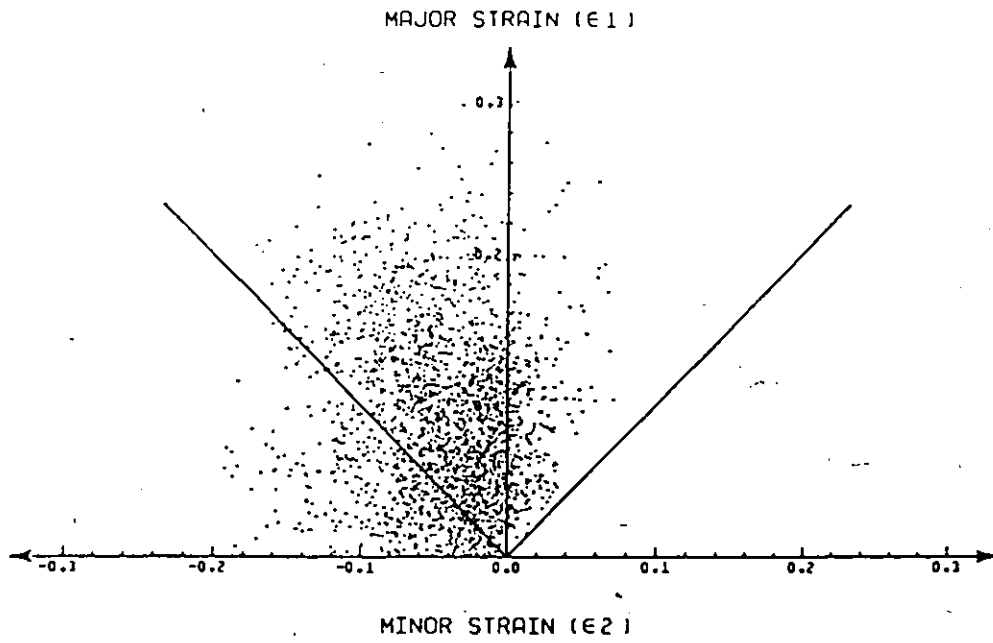
(a)



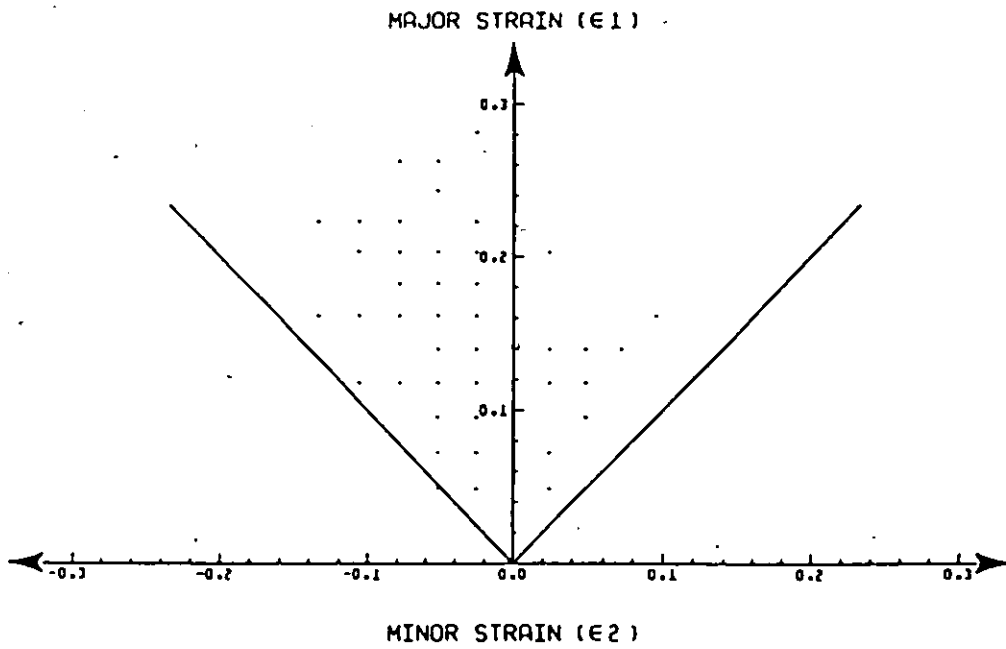
(b)

Figure 2.10: Circle grid technique

- (a) A mesh of the lower portion of the panel.
 (b) Strain contours in the flat sheet.



(a)



(b)

Figure 2.11: Element strains plotted in $\epsilon_1 - \epsilon_2$ strain space
(a) Square grid method.
(b) Circle grid method.

laboratory tests) F.L.D.'s can be superimposed on such diagrams as Fig. 2.11. Hence a comparison is available between the anticipated F.L.D. and the measured strain distribution. The experimentally determined points shown in Figs. 2.11(a) and (b) are for the upper left hand portion only of the panel shown in Fig. 2.4. The measured strains for the lower left hand portion showed a similar distribution. Figure 2.11(a) indicates that 90% of points obtained are below a major strain of 0.1. This is expected since in most sheet metal stamping operation materials seldom deform extensively. However, some of the points in the compressive region near a minor strain of -0.1 to -0.2 may be spurious because the analysis assumes chordal distances between adjacent nodes, whereas at sharp corners in the pressing, the surface lengths may be much longer. It may be that the half inch grid spacings are too coarse for this particular application. Figure 2.11(b) illustrates experimental strains determined from the circle grid analysis. Measurements were made of the deformed circles on the surface of the panel using an optical eye piece, and the maximum allowable accuracy of the instrument is about 0.02 inch; therefore small difference between adjacent ellipses cannot be measured and as such a point on the FLD may represent more than just one measurement.

The plots shown in Figs. 2.11(a) and (b) can serve as a useful aid to the designer. It is well known that sheet metals do not deform extensively when both principal surface strains are positive, i.e. the stretch mode. They tend to do better in the stretch-draw mode when the principal surface strains are of opposite sign. Furthermore when the

surface strains are equal and opposite there is no thickening of the sheet and this is represented by the line with slope -1 in Figs. 2.11(a) and (b). Deformation without change in thickness can be regarded as an ideal mode, and the plots of Figs. 2.11(a) and (b) reveal how close the designer is to achieving this. Furthermore, as already indicated, the anticipated F.L.C. can be superimposed on the measured strain plots. This permits the designer to decide whether any adjustments need to be made to the processing parameters if the measured strain is close to the proposed F.L.C. It also establishes the usefulness of F.L.C.'s particularly when these have been constructed theoretically as well as determined experimentally from laboratory tests.

2.4 Discussion

The present chapter has demonstrated how the magnitude and direction of the principal strains can be determined from measurements made on a deformed pair of lines. The application to the assessment of strains on a sheet metal component has also been illustrated.

Two techniques, namely the grid circle and the square grid technique, have been applied to the industrial stamping shown in Figure 2.4. The grid circles used were initially 0.2 in (= 5 mm) diameter and these were measured directly on the surface of the deformed part. The nodes of the square grids, initially of 1/2 in (12.7 mm) side, were digitized using a milling machine. A properly instrumented coordinate measuring device would have considerably reduced the labour involved but this was not available for this work.

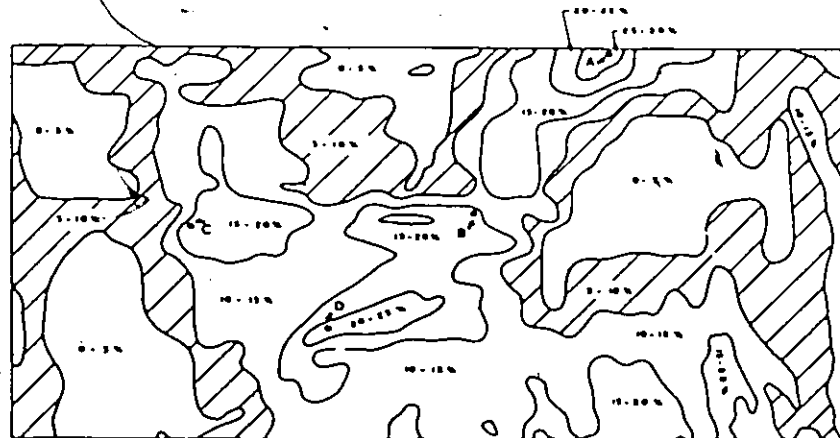
Contours of equivalent strain distributions, over the surface of the blank, measured by the usual circle grid method on the actual part and those computed from the square grid are summarised in Figure 2.12 for the purpose of comparison. Figure 2.12(a) and (b) are composite diagrams, where the strain contours of Figs. 2.7(b) and 2.8(b) have been combined to produce Fig. 2.12(a) and Figs. 2.9(b) and 2.10(b) amalgamated to provide Fig. 2.12(b). Regions of high and low strain level are observed by the square and circle methods. The magnitudes of the strains obtained by the square grid method is generally 5% lower than that of the measurements made from the circle grid.

With any moderately sophisticated computer-graphics system it would be easy to encompass any area on the strain contour diagram of Figure 2.12, and have the corresponding domain delineated on a plot of the surface of the panel. This is not done in the current study, but strain contours were manually drawn on the surface of the panel; these were colour coded to provide a better visual representation of the strain distribution on the whole panel, and this is illustrated in Figure 2.13. This shows that the smaller grid circle provides a more detailed account of the change in level of the strain contours, but the squares also reveal the same regions of high and low strain. It is debatable whether plotting contours of equivalent strain, as selected here, is the most appropriate way of helping the designer to assess critically strained regions of a stamping. Contours of thickness strain could be determined with equal ease, in this case excessive thinning or thickening would indicate a propensity to tearing or buckling

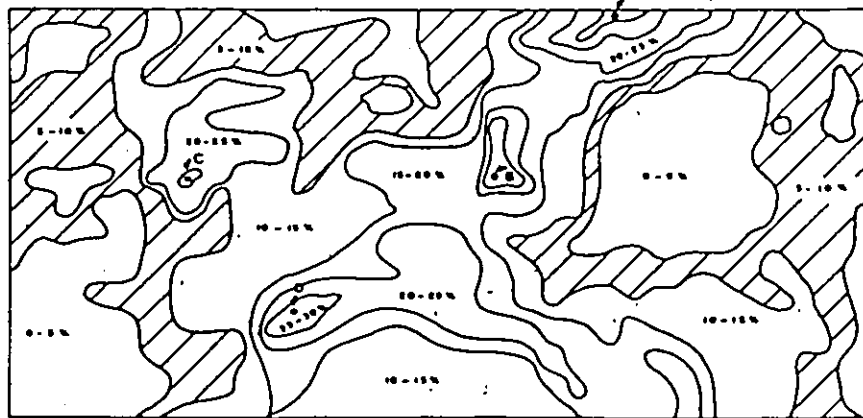
respectively.

The tedious manual measurements techniques used here are entirely unsuited for industrial practice. Techniques of automatic coordinate measurement are available and also image analysis systems have been developed to determine major and minor diameters of a deformed grid circle. Knowing that these aids exist, questions still remain about which grid patterns should be used, how they should be measured, what strain parameters should be calculated and how they should be presented. If no grid is used, measurements are limited to surveys of thinning. These are useful but if more information is required then, as mentioned before, some surface markings must be employed. If it is desired only to ascertain strain at a single point in the sheet, then the use of a grid circle is the most suitable method. If however, distribution of strain over a large region is required then it is almost mandatory that automatic measurement coupled with a computer-aided method of strain analysis and plotting will be employed. This chapter has illustrated how this can be achieved although a more efficient method of measuring the nodal points on the deformed panel would be desirable.

It has been shown that using a simple but nonetheless accurate method of strain analysis, the principal strains and their directions can be derived from measurement of a deformed square grid with greater ease than is generally imagined.

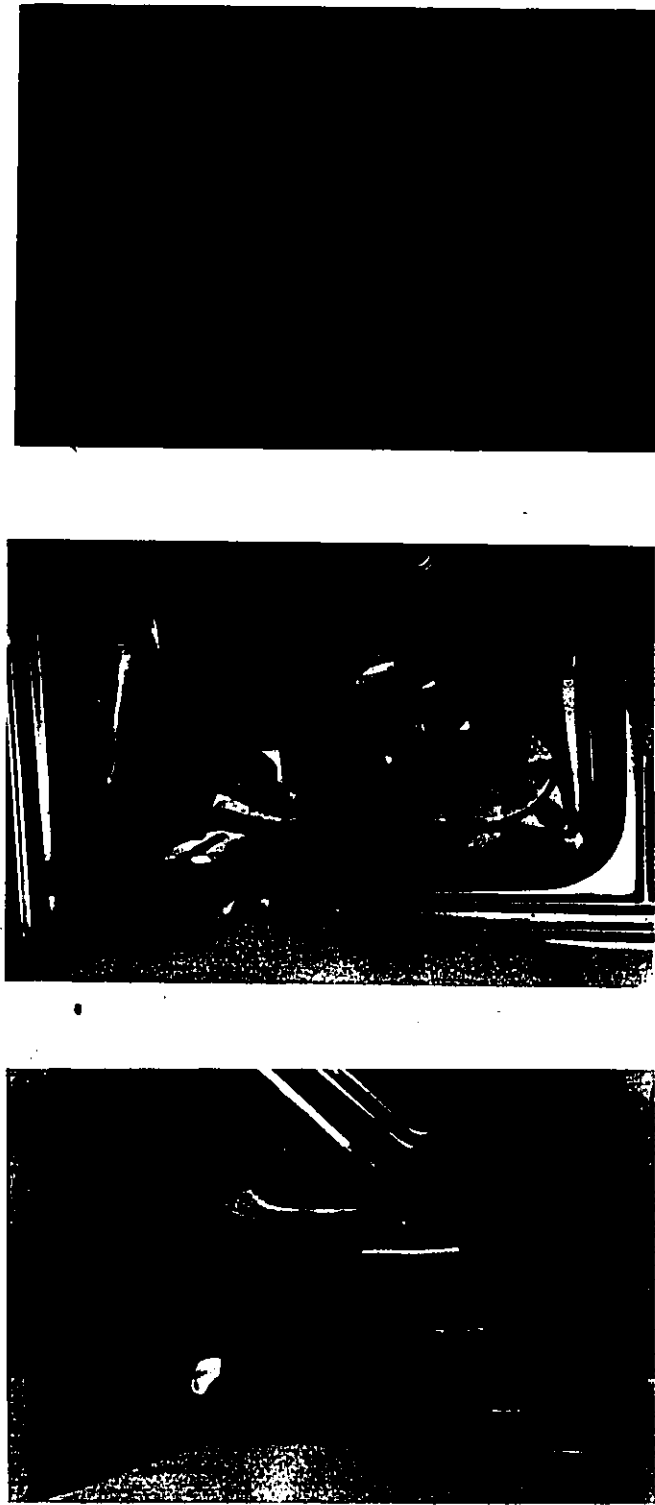


(a)



(b)

Figure 2.12: Contours of equivalent strain distributions
(a) Measured by the square grid
(b) Computed from the circle grid



(a)

(b)

(c)

Figure 2.13 Contours of effective strain distributions which were colour coded

(a) Square Grid Technique

(b) Circle Grid Technique

(c) Colour Codes of Strain Level

2.5 Conclusions

The present Chapter has demonstrated how strain distributions can be determined in certain finite deformation processes, based on measurements of the initial and final configurations of a grid marked on the surface of the workpiece. Certain differences between homogeneous deformation and pure homogeneous deformation have been drawn, when each mode produces the same final shape. The modes of deformation are intrinsically different, and although the initial and final shapes can be the same for each mode, all intermediate configurations are not. It has been mentioned that pure homogeneous deformation minimises the accumulated equivalent strain when producing a given shape change, and consequently the work done in such processes is likely to be minimised.

An example has been given of strain measurement of two similar auto body inner panels, one using an array of grid circles electro-etched on the blank and the other employing a blank on which a regular grid of square elements had been scribed. The measurements were taken manually, but the analysis and plotting were performed using the Cyber computer. A computer program for the evaluation of finite strain has been developed, based on the assumption of pure homogeneous deformation, and the principal surface strains within each grid element can be calculated with relative ease. In general, this will result in an underestimate of the actual strain incurred. The error may not be large, but since the strain path of elements on the surface of a panel is unknown, a lower bound estimate of the strain has to be tolerated. It is recommended that a square or rectangular grid of lines be employed for the

calculation of strain over the surface of industrial stampings.

With the advent of coordinate measuring devices and computer-aided techniques of image analysis, it is possible to obtain a quick check on the strain distribution over certain chosen regions of interest on the stamping. Thus, it allows a tool designer or die-setter to gain more insight into the deformation of the component that he works with.

The technique of finite strain determination will be incorporated into a computer-aided tool and die design package described in Appendix D.

CHAPTER 3
GEOMETRIC MODELLING

3.1 Introduction

A sheet metal panel is usually produced in a double-action press. The tooling consists of two basic assemblies - a matching punch and die which define the shape of the panel, and a draw ring or binder, which surrounds the punch and die and controls the flow of the sheet inwards as it is formed to the required geometry. In order to design the punch properly, the deformed shape of the blank must be known after it is preformed by the binder. The proper design would be the one in which the preformed blank wraps around the descending punch gradually and uniformly with the avoidance of loose metal and hence the possibility of wrinkling. When conforming to the binder there is no stretching or distortion of the sheet under the clamping action of the press, only bending. As the punch descends and contacts the sheet, tensions are developed and the material is dragged inwards against the restraint exerted by the binder. The process of forming a flat sheet of metal to a complicated shape between matching dies in a press is known as stamping. Considerable expenses are involved in developing and manufacturing the tooling, and a typical automotive stamping die may cost as much as one half of a million dollars.

Traditionally, tool geometry has been determined by experience or by an experimental die try-out process. If wrinkling occurs during the

process then draw beads can be added into the tooling in order to reduce the tendency of the material to draw-in. The process is repeated many times until a final acceptable result is achieved. However, the technique tends to become very tedious when dealing with more complex geometries and requires the engineering skill and experience of the tool designer.

In modern sheet metal engineering practice, the shape of the finished panel is specified in a master geometric data base within a computer graphics system [11-14]. The tool designer will extend this data base to specify tooling in the regions outside of the trim line for controlling tension and restraining the edges of the panel during forming. He must also specify the size and shape of the flat sheet required to form the part. This problem, known as blank development, determines the size and shape of the initial sheet or blank, but in order to aid the designer in devising appropriate tooling shapes, it would be highly advantageous to know precisely where all points in the flat sheet are located after forming; that is to say, one needs in the computer graphics system a transformation of points between their initial and final position. As pointed out in the Introductory Remarks of Chapter 1 this can be a formidable task, and it seems worthwhile to explore simpler, albeit more approximate, methods for achieving this.

In the present study some results are presented of a detailed development of a computer-aided die design system for assessing the shape of a blank for a sheet metal stamping. The technique is referred to as geometric modelling and is intended as a computer aid for the

experienced tool designer. No attempt is made to satisfy force equilibrium point to point within the material, and the mechanical properties of the sheet material are not even considered. Only geometric constraints are accounted for.

3.2 The Ideal Sheet Forming Process

The starting point in the process is some specified final part shape that the designer would like to achieve. Geometric modelling, as the name implies, is a technique whereby a flat sheet is transformed to the final part by purely geometric means. In fact the reverse procedure is adopted herein and the proposed final shape is initially mapped back into a flat sheet. The mapping process does not reveal a unique solution, merely a geometrically possible one. However on the basis of the mapping strategy a possible strain distribution can be calculated for a deformation process which is geometrically feasible.

In most instances, the designer would like the sheet to transform from the flat or developable surface to the complicated shape of the final part without change in thickness. This mode of deformation has been alluded to in Chapter 1. Each element would be deformed by plastic shearing so that its area remains constant. Avoidance of thinning is usually a practical objective and furthermore, it may be shown that failure by tensile necking or tearing is not likely to occur in this mode [15]. (The process is less than "ideal" in a practical sense since wrinkling can still occur.)

In most sheet processes, the contact pressure between the sheet

and the tooling is quite small and we can consider that the only stresses acting are those in the plane of the sheet as illustrated in Figure 3.1(a), i.e. a state of plane stress. If the material is assumed to be a rate-insensitive, isotropic solid, obeying the Von-Mises yield criterion, the plane-stress yield locus is as shown in Figure 3.1(b). The laws of plastic deformation indicate that the combined stresses necessary to deform this element are related by the ellipse shown in Figure 3.1(b). The process in which $\sigma_1 = -\sigma_2$ results in a constant area deformation is usually referred to as "drawing" and it can be seen that the magnitude of the stresses required to deform the sheet are less for this process than for any other. In sheet metal forming, deformation is produced by tensions transmitted through the sheet, not by forces applied to the surface as in forging, and therefore that deformation process which occurs at the lowest value of stress is at least a likely mode of deformation.

It is found that many of the traditional die design calculations which are described in handbooks are based on this constant area rule [16]. These die design formulae were devised for manual calculation techniques and are not appropriate for a computer-based system. The method described here is essentially an extension of this approach to an elemental mapping technique which can be applied automatically in a computer system and which provides the designer with an indication of the way in which a flat sheet would deform if it obeyed the constant area hypothesis.

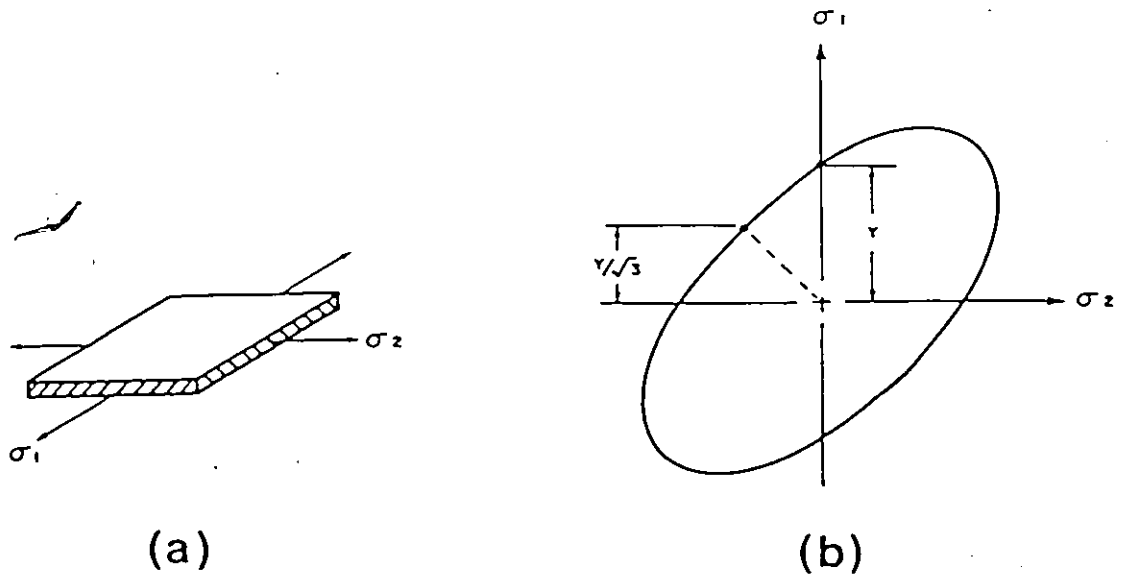


Figure 3.1: (a) Deformation of an element in plane stress
 (b) A plane stress yield locus

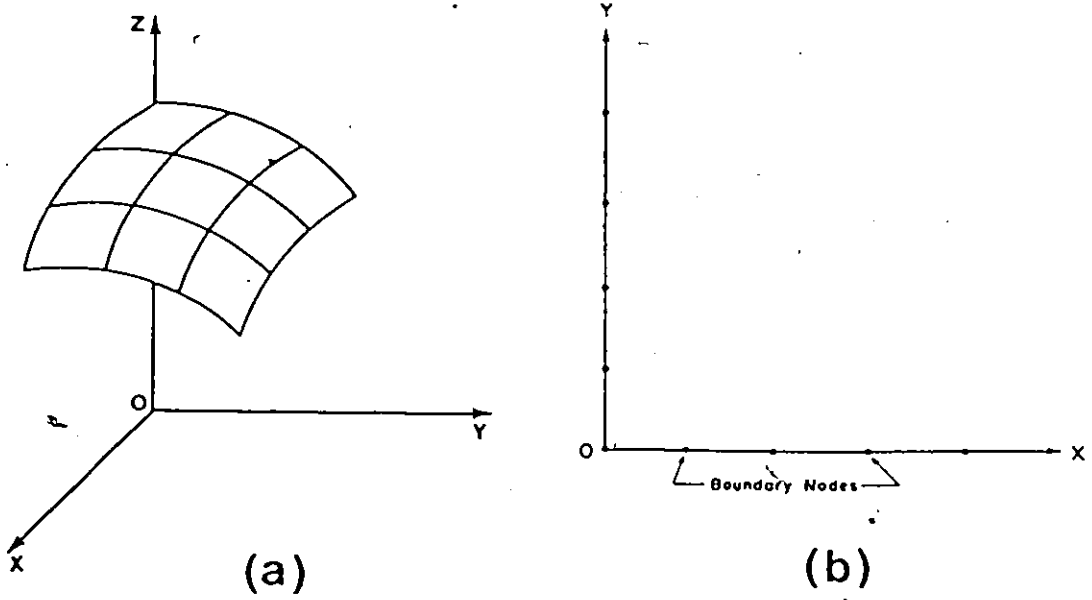


Figure 3.2: (a) Part of a surface in space
 (b) Boundary conditions of Fig. 3.2(a) on a flat plane

3.3 Techniques for Mapping Elements

Results are presented of a new method for finding the shape and size of a blank for a sheet stamping. The present method is intended as a computer aid for the experienced tool designer. This computer-aided technique involves element-by-element mapping of an irregular mesh, which has been marked on the deformed surface, back into a flat blank. The transformation of the elements requires a mapping procedure and it is the purpose of this section to provide a detailed discussion of some of the mapping strategies developed. The merits and drawbacks of each are also examined. In this system, no attempt is made to satisfy force equilibrium from point to point within the material, in fact the mechanical properties of the sheet material are not even considered. Continuity of the elements is however maintained and the resulting deformation is geometrically possible. Whether or not the solution is physically possible depends on the skill of the designer in guiding and adjusting the process.

3.3.1 Basic Method

(a) Mesh Generation

The surface geometry of a stamping can be specified by a physical model, an engineering drawing or in a computer graphics system. One may then generate a mesh to cover this surface, as for example, in part of a stamping as shown schematically in Figure 3.2(a). The surface is approximated by contiguous triangular elements, each pair composing a

quadrilateral element folded along one particular set of diagonals.* These elements approximate the actual geometry of the given stamping and furthermore these elements are arranged so that they form a rectangular array of rows and columns. This is known as a topologically rectangular mesh.

The designer must be aware that two options of grid markings are available if an actual stamping is employed.

(1) The grid can be a deformed grid of lines previously scribed on the undeformed blank - such as the part shown in Figure 2.4, and which is discussed in Chapter 2 but only in terms of strain analysis. However, the same grid could be used for the mapping.

or (2) A topological grid is marked on the deformed blank, such as the seat stamping of Figure 3.3, using a felt marker pen. This technique is adopted in this Chapter.

Quite often in the design process an actual stamping is not available and a clay or wooden model of the part is employed, hence a grid would have to be marked on the surface of the model.

(b) Boundary Conditions

The method requires that some appropriate displacement boundary conditions be specified for certain nodes. In most sheet metal pressings a plane of symmetry, or alternatively a dividing line, can always be identified. It is indicated in Figure 3.2(a) that planes XOZ

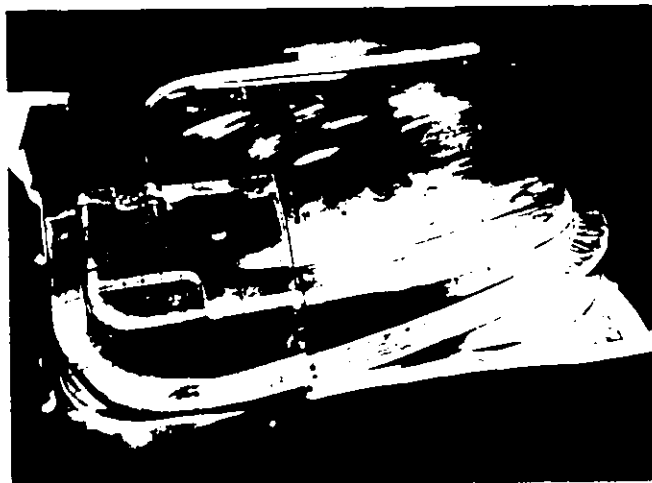
* It is chosen so that a general sub-program for automatic numbering of nodal points and elements on a given surface may be achieved.

and YOZ are planes of symmetry and hence the components of displacement perpendicular to these planes will be zero. In the initial mapping it is also specified that the distance between these boundary nodes does not change, i.e. the sheet deforms without extension along these lines of symmetry. This particular boundary condition is an arbitrary one.

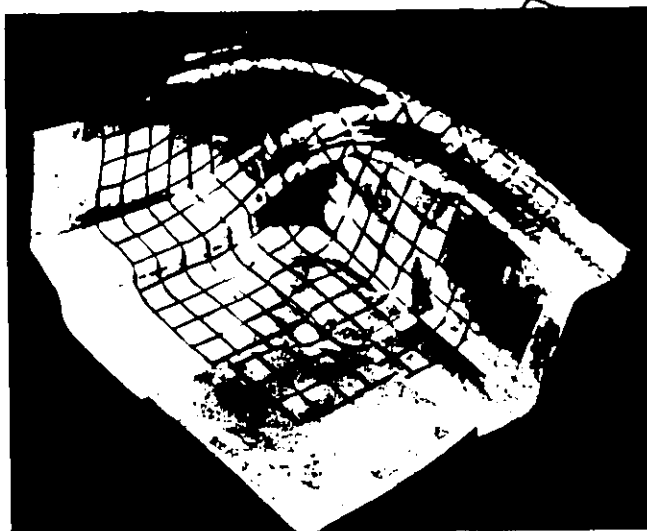
If the designer considers that the spacing between the nodes changes along the axes of symmetry he can impose such a condition; hence the designer may change the input conditions in light of his own experience.

The boundary nodes can then be mapped in the XOY plane, as illustrated in Figure 3.2(b). This provides a starting point in which three vertices of a quadrilateral have been fixed at the intersecting corner of the axes of symmetry. The problem now is to map each of the nodes onto a flat plane according to some selected strategy. One essential requirement is that adjacent elements remain contiguous during the mapping process.

An automotive stamping is considered, it is chosen for the purpose of determining the feasibility of the mapping procedures. A grid of quadrilateral elements was drawn freehand on the part using a marker pen and these elements are topologically rectangular. A photograph of the original stamping from which the corner section was removed, is shown in Figure 3.3(a). The stamping is part of a passenger car seat. Figure 3.3(b) shows a photograph of the piece removed from the corner for modelling. Each mapping method developed herein will then be adopted to find the size and shape of a sheet metal blank which could be transferred into the surface of the deformed part which is



(a)



(b)

Figure 3.3 Photographs:

- (a) of seat stamping and
- (b) the area removed from the corner for modelling

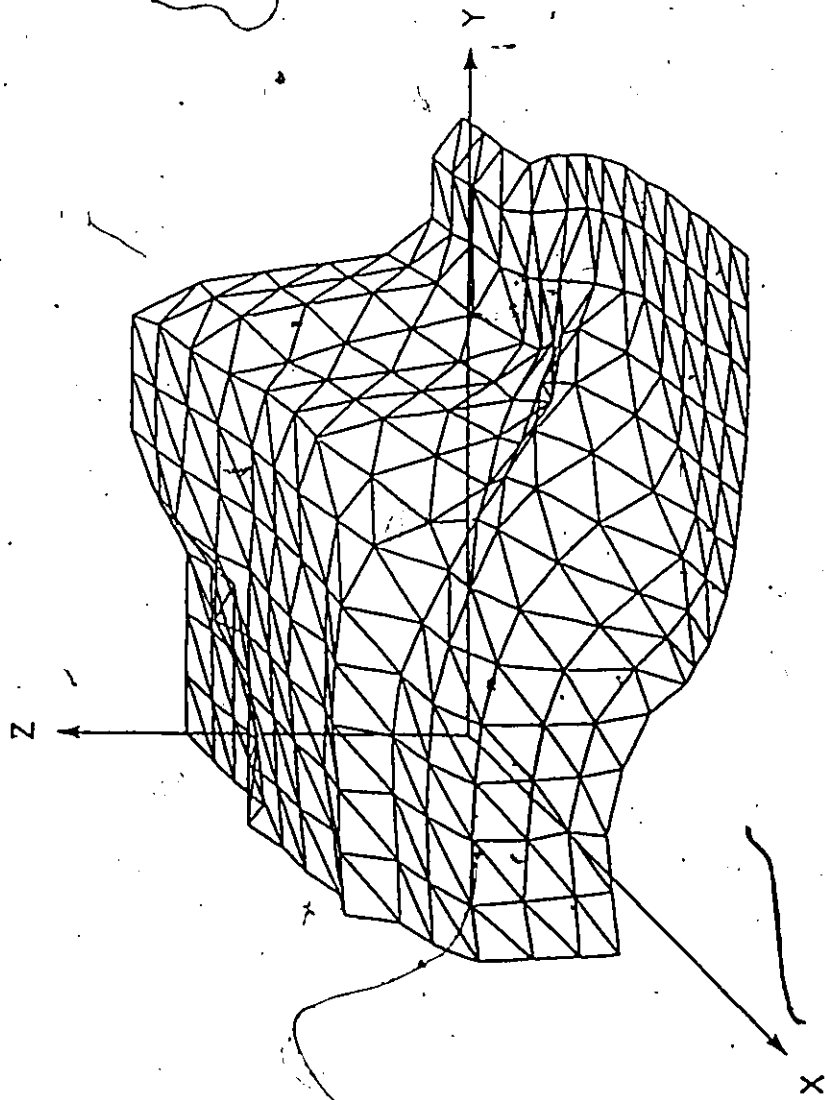


Figure 3.4: Mesh obtained for part of a car seat panel which is modelled

defined by the grid of lines shown in the photograph. The nodes of the grid were digitized with the aid of a milling machine and a computer plot of the surface is shown in Figure 3.4.

3.3.2 Mapping Strategies

(1) Proportional Deformation :

The quadrilateral element IJKL in Fig. 3.5(a) is assumed to represent part of a curved surface in three dimensional space. The two triangular domains, IJK and ILK, actually represent two flat facets on the deformed surface. We assume for the moment that part of the mapping process has been completed and the points i, j and k have been located in the flat plane XOY, as shown in Figure 3.5(b). The area of the triangle ijk is known and the vertical height, h, of the new triangle kil can now be determined, since this must satisfy the condition of equal area for the initial and final quadrilateral.* The area of the individual triangles IJK and KIL do change in this mapping process but the sum of their areas is constant, i.e. the area of the quadrilateral IJKL is unchanged.

The position of l along the line shown in Figure 3.5(b) must now be found. Proportional displacement is assumed, and this will be apparent from Figure 3.5(c) where the initial triangle KLI and the ~~final~~

* The constant area hypothesis is an arbitrary one. A designer may change the area of elements in light of his own experience, however, this assumption is a convenient and simple one. It is based on the fact that under idealised conditions, materials tend to deform without change in area (a pure shear mode).

triangle kli are shown superimposed. The position of m along ki is determined by the assumption that the displacement of M will be proportional such that

$$\frac{MI}{KI} = \frac{mi}{ki} \quad (3.1)$$

The new node l can then be located on the XOY plane. The mapping of the rest of the elements is conducted in the same manner.

This method was found wanting when applied to the part of the stamping shown in Fig. 3.3(b) or Fig. 3.4. The mapping procedure failed in the more severely deformed regions of the component. It can be concluded that this particular mapping strategy develops unacceptable instabilities in the sheet leading to overlapping of elements as shown in Figure 3.6. In an attempt to overcome this difficulty, an arbitrary limit was imposed on the change in the apex angle of any triangle during the mapping process. This tended to dampen out severe changes in the shape of a triangular element, and a preliminary result is shown in Figure 3.7. This is free from overlapping but deficiencies are still evident in that the boundary is very irregular. The edge of the mesh was deliberately drawn near the edge of the actual stamping and hence a realistic map would be much smoother at the boundary.

These results suggest that there are two possible handicaps associated with the model under consideration. Firstly, it is obvious that the imposed equal area hypothesis is likely to be too restrictive. Secondly, it is recognised that the imposed proportional deformation appears to restrict one of the principal directions to lie along the diagonal. This is unlikely to occur in actual forming processes, and

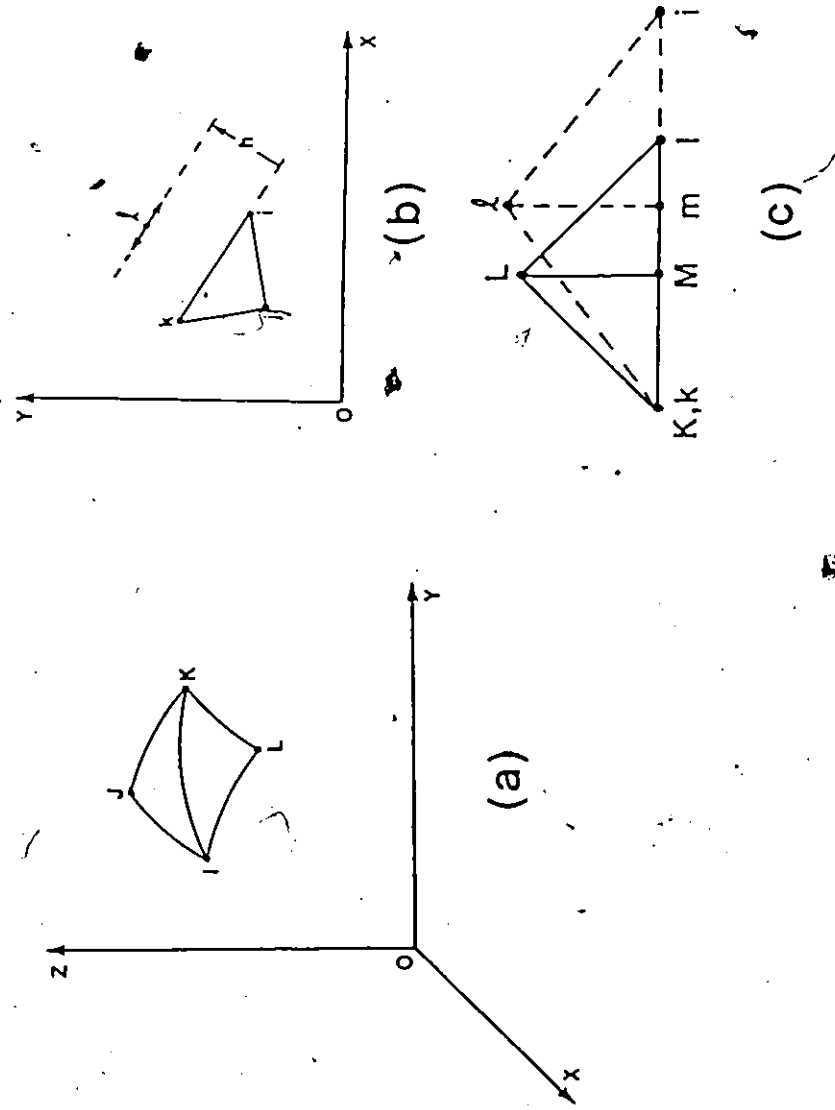


Figure 3.5: (a) Quadrilateral element on the curved surface
 (b) Locating the fourth node in the plane surface
 (c) Illustrating the assumed proportional deformation

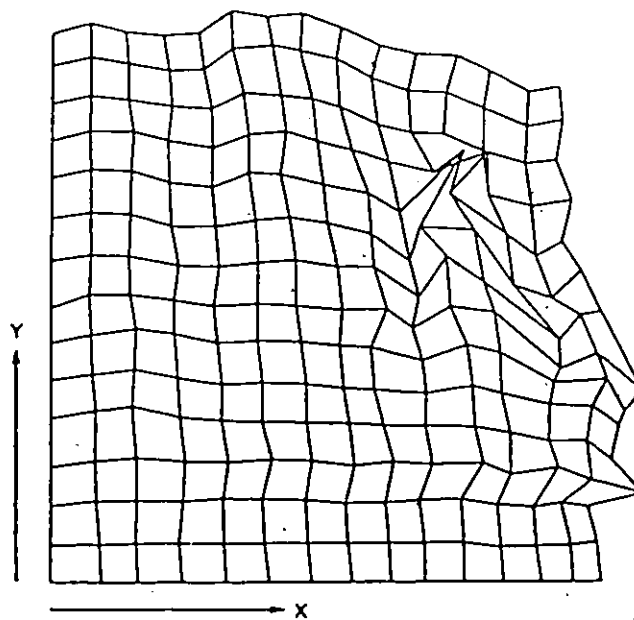


Figure 3.6: Transformation of the mesh in Fig. 3.4 onto the flat plane, overlapping of some elements occurs with the proportional deformation strategy.

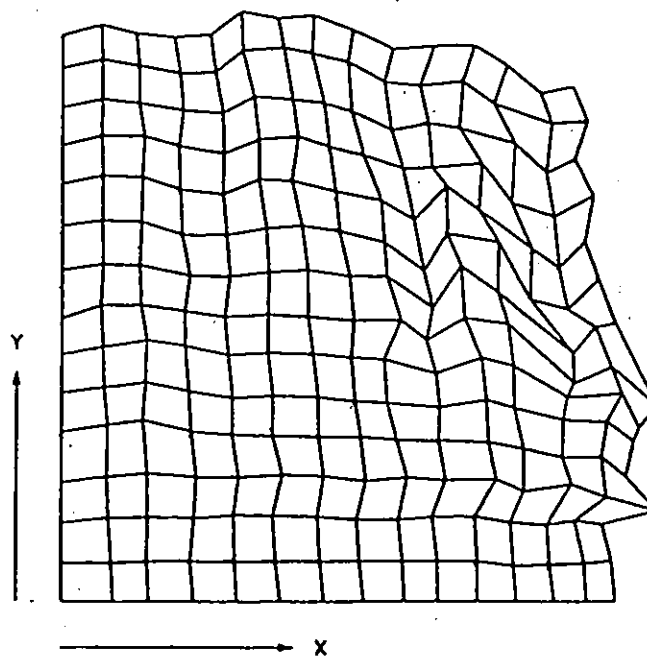


Figure 3.7: An improved transformation into the flat plane.

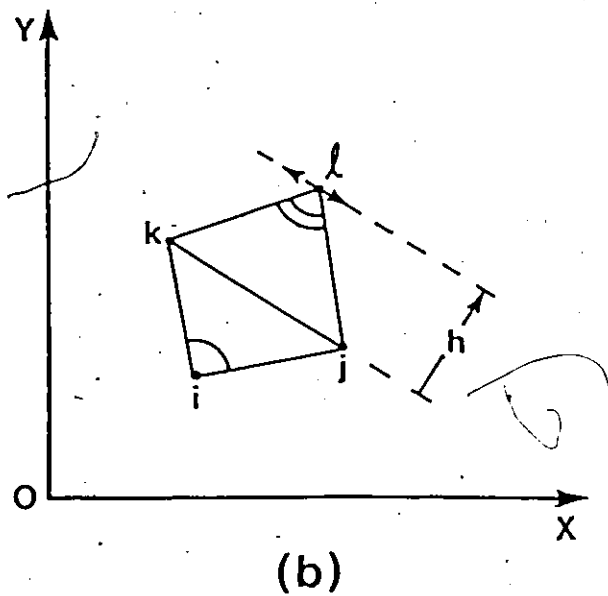
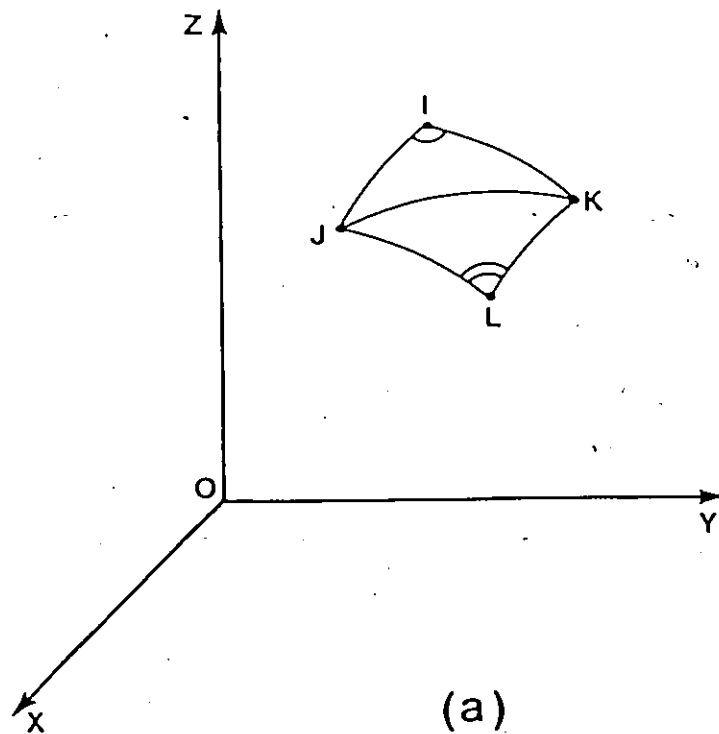


Figure 3.8: (a) A facet on the curved surface
 (b) Diagram showing the assumed proportional change of angles.

therefore other approaches were developed to provide the tool designers with a system based on a more appropriate strategy.

(2) Proportional Change of Angles

Many features that have already been discussed in part (1) will be retained, and in particular the equal area hypothesis. Again the element IJKL is assumed to represent two triangular facets on a curved surface shown in Figure 3.8(a) and in this instance the mapping has proceeded up to the point where the lower triangle IJK of the quadrilateral is located onto the flat plane XOY, as shown in Figure 3.8(b). The vertical height, h, can be calculated such that the sum of the area of triangles ijk and jkl is equal to the area of the quadrilateral. The only problem is to map the remaining node l on the same plane.

The position of l along the line shown in Figure 3.8(b) is found by relative deformation of the apex angles of the upper and lower triangles of the quadrilateral IJKL with respect to the quadrilateral ijkl on the flat plane. It is postulated from Figure 3.8 that the change of the apex angles of the triangles before and after the deformation will be proportional, such that

$$\frac{\text{Angle KLJ}}{\text{Angle KIJ}} = \frac{\text{Angle klj}}{\text{Angle kij}} \quad (3.2)$$

The new node l on the flat sheet can then be found upon satisfying the previously stated conditions. The rest of the nodal positions can also be obtained in the same manner.

The method has been implemented in Fortran code in which an

iterative routine is involved to search for the location of the fourth node of a quadrilateral. The routine consumes a large amount of computer time and thus the mapping becomes very inefficient. Though this mapping procedure seems to improve upon the technique discussed in the preceding section it is by no means entirely adequate. It was found that in the vicinity of a severe bend or sharp corner, where highly irregular elements are present, it became difficult to identify the position of the fourth node in order to satisfy all the above required conditions.

The occurrence of such a difficulty would imply that large surface area changes are likely to take place in the actual pressing. It indicates that there is a deficiency in the imposed geometric strategy, i.e. the requirements that the deformed and undeformed quadrilateral elements maintain the same surface area, and the mapping process which serves to satisfy this hypothesis. It is also noticed that the irregularity of the hand drawn elements is likely to affect the mapping. It is advisable to employ a finer mesh, particularly for parts with a more complex geometry, in order to provide a better representation of the surface.

(3) Proportional Area Change

In an attempt to modify the constraint of area constancy, the method discussed in this section provides a mapping strategy that would allow for the area of each element to change. Again it is assumed that the mapping process has proceeded up to the point where the triangle ijk

has been located on the flat plane (as shown in Figure 3.8(b)). The remaining node l of the quadrilateral IJKL is now in a position to be transformed onto the 2D plane XOY. The transformation is governed by a proportional change of area rule. It is apparent from Figure 3.8 that the area jkl may be obtained through the relation

$$\frac{\text{Area } jkl}{\text{Area } JKL} = \frac{\text{Area } ijk}{\text{Area } IJK} \quad (3.3)$$

and in this case, the area of the quadrilateral is changed.

The vertical height, h , of the triangle jkl can be calculated from the known magnitude of the area jkl and the position of l along the line shown in the diagram may be identified with the application of the procedure of proportional deformation as described in part (1).

This technique was applied to part of the industrial stamping shown in Figure 3.3(b). It generates a blank which is similar to that of Figure 3.6, and therefore any improvement in the mapping process is not immediately obvious. The overlapping of elements also occurs in the same region as on Figure 3.6, but to a lesser extent. The overlapping of the elements is reduced since a large change in the area of a triangular element of a quadrilateral has been compensated for by the same amount of area changes in the opposite triangle and therefore this smooths out some of the oscillations. It is interesting to observe that the unacceptable instabilities occurred in a region where the trial stamping showed severe wrinkling.

The non-conforming elements indicates that there is a deficiency in the imposed geometric rule; again the assumed proportional

deformation appears to give rise to severe distortions in the sharp bends or other abrupt geometric changes in the stamping. Nonetheless this technique may serve as a warning system at the preliminary design stage to indicate regions where the stampings are likely to fail by wrinkling.

(4) Intersection Method

So far no consideration has been given to the effect that the mapping of an element may have on the deformation of the neighbouring quadrilateral elements. It is the aim of the present method to take into account of the contribution of the local deformation of neighbouring elements and hopefully this procedure will smooth out the distortions on the whole sheet and a reasonable blank shape can then be attained.

Suppose that the boundary nodes have already been transformed onto the flat plane XOY, this provides a starting point in which the lower triangle ijk of the quadrilateral shown in Figure 3.9(a) is known. The remaining problem is to map the node L onto the flat sheet. In this technique three quadrilaterals will be considered, the element IJKL and two other adjacent elements, one on the right and one on the left of the element IJKL are also involved in the determination of the location of L on the flat blank. The elements in question are shown in Figures 3.9(a) - (e). Again the vertical height, h_1 , of the triangle jkl can be calculated for the area of the triangle JKL to be unchanged during deformation; a line paralleled to the base of the triangle along which

the position of l_1 lies may then be constructed. This provides a possible solution of the third node of the triangle under consideration, but not a unique position for l_1 . If attention is now focussed on the adjacent triangle JML of the neighbouring element, a similar construction can be made where the height h_2 is determined by the equal area hypothesis. Likewise for the adjacent triangle KNL to provide the distance h_3 .

As can be seen the mapping technique will, in general, yield three possible solutions for the position of the fourth node of a quadrilateral. Since a single position of the node L is sufficient to solve the problem, hence we must select the most probable one. In order to do so a triangle $l_1 l_2 l_3$, as illustrated in Figure 3.9(e), is constructed. It is obtained by the extension of the three parallel lines discussed previously; these lines would intersect and meet at possible nodes l_1 , l_2 and l_3 . Thus a triangle which contains all possible solutions to the node L is established. Any positions within which will provide a possible solution to the mapping process. For simplicity it is assumed for the present time that the centroid of the triangle $l_1 l_2 l_3$ is the most probable location of the fourth node of the quadrilateral under consideration. This determines the position of the node L and the transformation of the rest of the elements are performed in the same manner.

It is observed that the area of the quadrilateral would change slightly upon identifying the nodal position of L. However, continuity of thickness changes across the sheet is not maintained, i.e. the

thickness between one element to the next may be different depending on the severity of the deformation or the surface geometry of a stamping.

The above mentioned mapping procedures were implemented in Fortran code and the technique was applied to the industrial pressing shown in Figure 3.3(b). The mapping technique does not appear satisfactory in regions where severe bends appeared in the actual stamping. In the vicinity of the bends, elements on the flat sheets tend to spread out away from the bends in order to accommodate sharp changes in geometry which arise in the sheet. At some points where elements are squeezed beyond the state where elements can be mapped without interference between neighbouring elements, overlapping of elements occur. It appears that the mapping process is unable to smooth out the deformation in the neighbourhood of the problem area. This is perhaps due to the fact that the location of the fourth node of an element is dependent not only on the element itself but also on the deformation of the neighbouring elements. Therefore, a small oscillation in one element may eventually affect other elements and this becomes a serious problem (instability) for the mapping process. Nonetheless, as mentioned, such an instability of the mapping may serve as a warning signal to problem areas where the sheet would fail by wrinkling or tearing. This point has to be verified by experience.

This strategy emerges from the original work developed by Professor S.G. Wang of University of British Columbia.

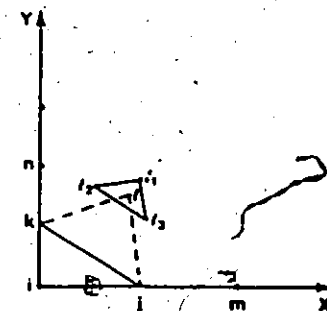
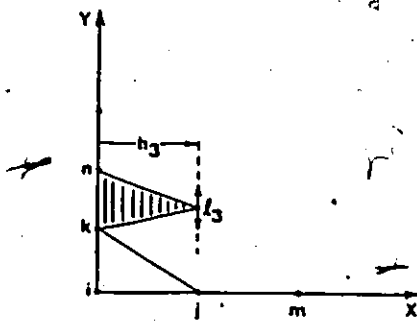
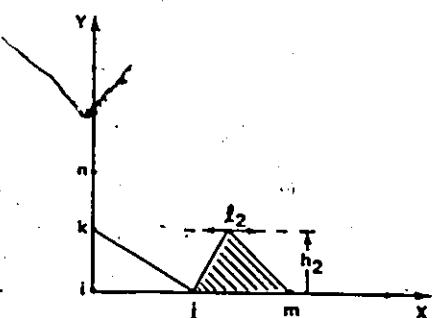
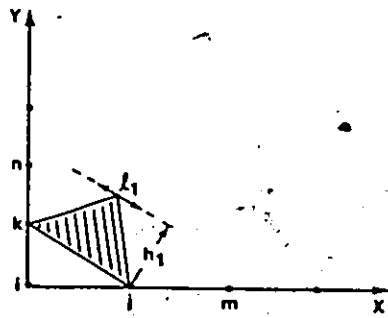
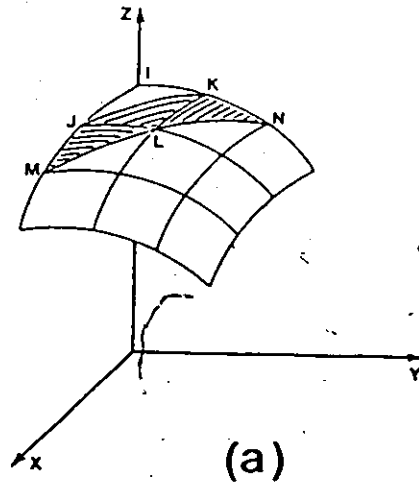


Figure 3.9(a)-(e): Diagrams illustrating the sequential mapping procedures of the fourth node L by the intersection method.

(5) Area Criterion

In light of the difficulties discussed in part (4), the method described herein is proposed in an attempt to provide a simple modified mapping procedure which is physically sound and realistic. This new approach retains many features that have been examined previously. The mapping technique is very similar to that described in the above section, the exception is that the modelling is focussed solely on a single quadrilateral, and does not involve neighbouring elements. However, the location of the fourth node is achieved in a like manner to that described in the preceding section.

It is assumed that the mapping process has progressed up to the element IJKL, as illustrated in Figure 3.10(a), and that the triangle ijk is mapped onto the flat plane as shown in Figures 3.10(b)-(e). Lines which are parallel to the base lines jk, ij and ik can be determined entirely by considering the area of the corresponding triangles JKL, IJL and IKL respectively; the vertical heights, h_1 , h_2 and h_3 of these triangles can then be calculated. They define the offset distances of each possible location of the node L from the base of the triangles. Upon extending these parallel lines the triangle $l_1 l_2 l_3$ is formed, the vertices of which would provide three possible solutions to the position of the fourth node L on the flat sheet. The detailed step-by-step mapping of the node has already been described in full in part (4). As before we select the centroid of the triangle as the location of the node L on the flat blank. The mapping of the rest of the elements is conducted in a like manner.

The method appears to function well when applied to the industrial pressing in Figure 3.3(b). The result of the mapping procedure is given in Figure 3.11, the uneven edges at the upper right hand corner of the blank suggest that the mapping process still is not entirely representative of an actual deformation process. It generates however a map which could be changed by various adjustment procedures by the designer. The upper right corner illustrated in Figure 3.11 suggests that the metal should be allowed to flow inward more to avoid fracture in the stamping. It is interesting to observe that in the actual stamping a portion of material has been held back after forming and the pressing has physically failed by tearing in this region. The uneven elements at the top and right hand boundaries also suggest that in the actual operation draw beads might be added on the boundaries to inhibit too much inflow of material in order to control wrinkling of the sheet during deformation.

The predictions of the current mapping technique reveal certain features displayed in the actual stamping. In the strategy no restrictions have been imposed on the inflow of the material at the boundaries. The actual physical restraint in the part is imposed by draw beads etc. in the stamping operation. Consequently the predicted inflow of the material in certain regions will be larger than that which occurs in practice. This is a further constraint which the experienced die designer could incorporate in the mapping strategy.

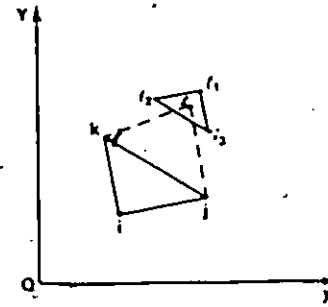
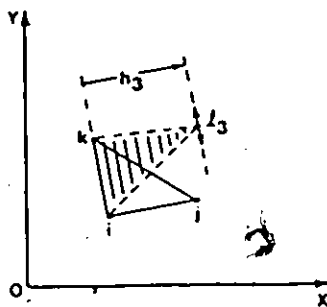
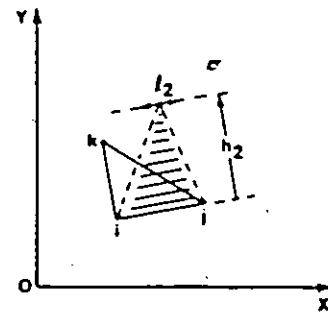
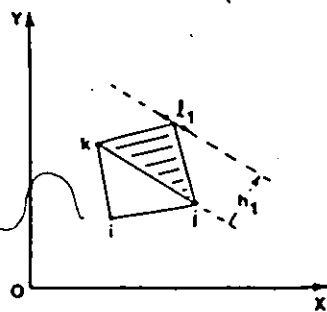
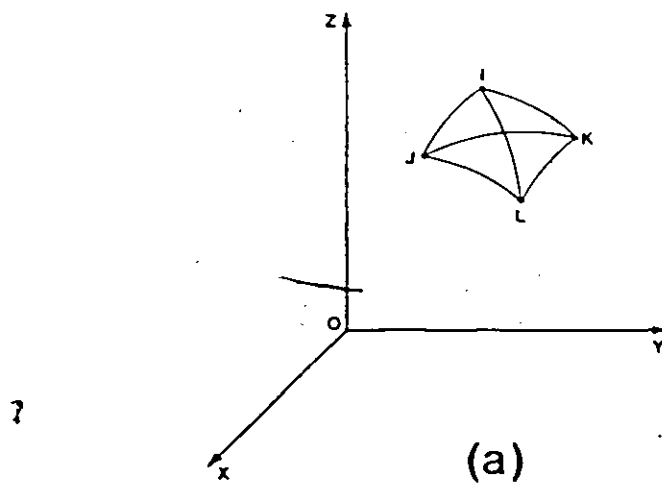


Figure 3.10:(a)-(e). Diagrams indicating transformation procedures for finding the most probable position of the node L using the method of area criterion.

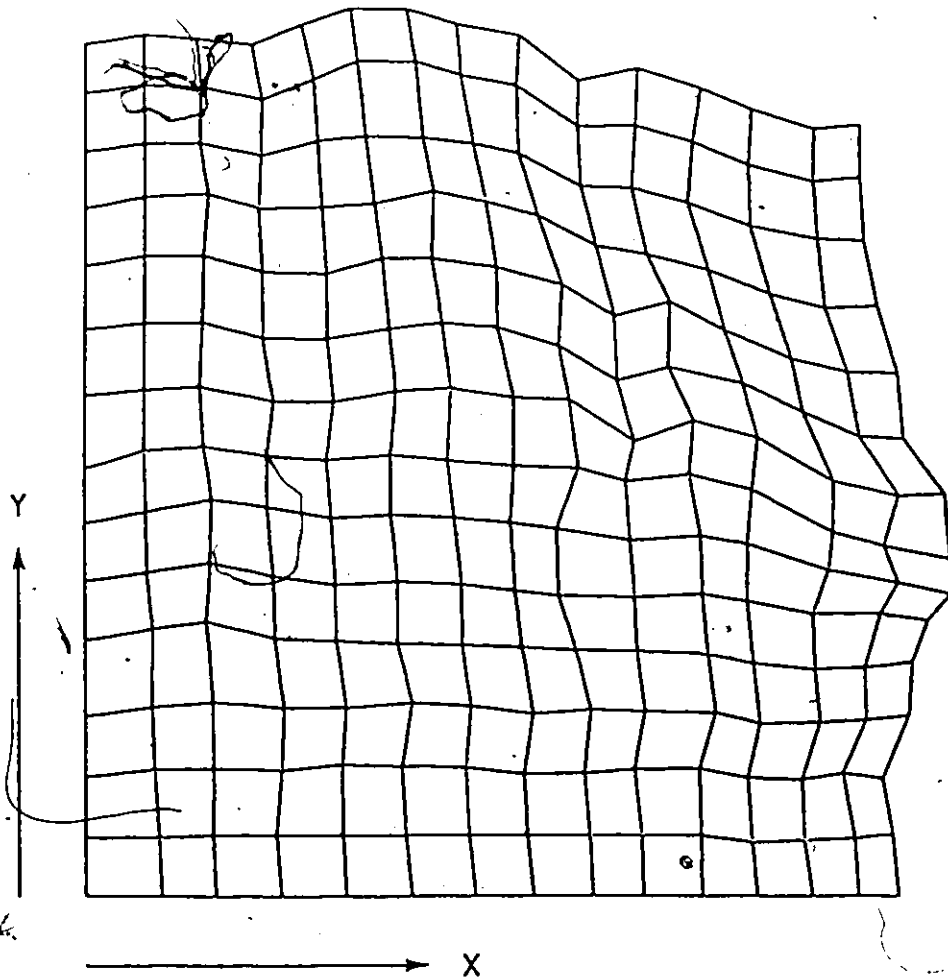


Figure 3.11: The resulting transformation of the surface in Fig 3.4 which is obtained by applying the method of area criterion.

3.3.3 Comments on Mapping Strategies

It is shown in this section that many strategies exist for element-by-element mapping of a mesh drawn on a surface of complicated shape. Instabilities have been found to occur in some methods in regions of large strain.

A strategy which approximates to the equal area hypothesis was found to be the most suitable. In this strategy three vertices of a quadrilateral are known and three locations for the fourth vertex are established. These form, in general, a triangle and the procedure adopted is to locate this vertex at the centroid of this triangle.

The various mapping strategies described in the preceding sections have been shown to effect the resulting blank shape when they are applied to an actual sheet metal stamping. The fifth strategy, named the Area Criterion, appeared to be the most appropriate. It is worthwhile investigating whether this particular method would still show advantages over the other techniques when applied to a simple test case.

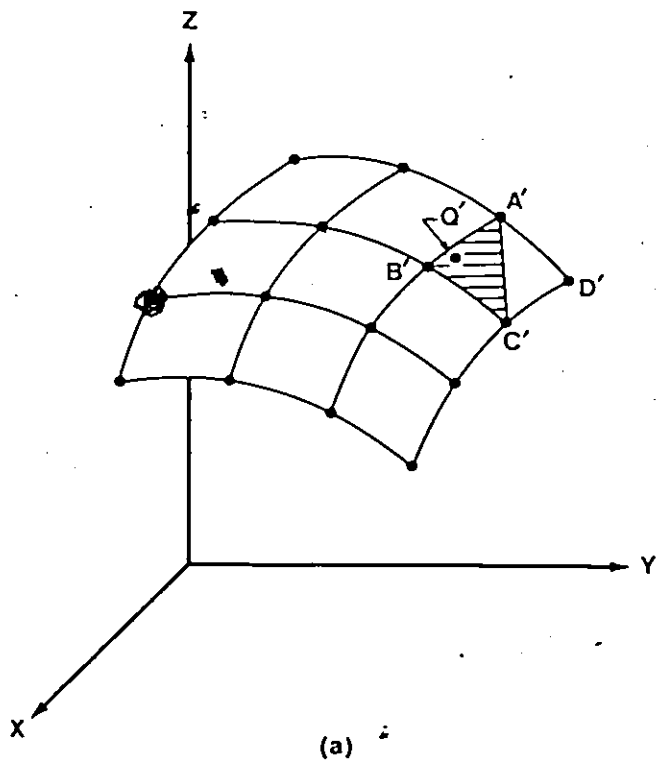
The requirements of the test case are that it should involve large strains and displacements and that an exact analytical solution of the deformation problem should be easily obtained. This would provide a "correct" solution against which the actual mapping could be compared. In the present work the test case considered is the forming of a hemispherical shell from a flat circular disc. The exact blank shape is generated analytically, the result of which is compared with the blank developed by the mapping procedure. Various types of mesh are also employed in the test case to ascertain the sensitivity of the result to

the grid geometry. The study has demonstrated that the mapping procedure, namely the area criterion, performs well and it is recommended that a reasonably regular grid mesh should be constructed, and that the mesh should be made finer in regions of abrupt geometry changes on the stamping. Further details can be found in Appendix C.

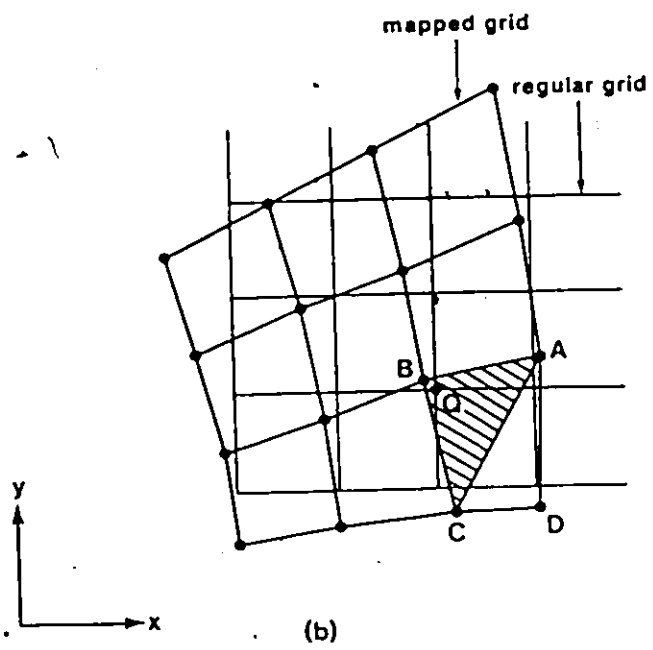
3.4 Remapping - A Theoretical Consideration

A method has already been described in section 3.3.2 in which an irregular grid drawn on a specified surface of general shape is mapped onto a flat sheet following some geometric rule. Tool designers are accustomed to thinking in the opposite way, i.e., how a regular grid marked on the flat blank would appear when the sheet is deformed to the final shape. To accommodate this, a method will be developed for superimposing a regular grid on the flat blank and mapping this back onto the deformed surface. The technique is based on interpolation from the known displacements of neighbouring nodes of the irregular grid. The method provides a visualization of a geometrically possible deformation mode of a flat blank in a stamping process, and is part of a computer-aided die design system which can be used by an experienced tool designer.

The mapping method can best be described by a simple illustration as shown in Figure 3.12, where the location of a regular mesh point Q, established on the flat plane, has to be positioned on the deformed surface of the stamping. The relocation of point Q is obtained in the following way. As explained previously the surface of the actual



(a)



(b)

Figure 3.12: (a) Illustrating the position of a remapped point on the surface.
(b) Diagram indicating the irregular grid points developed by mapping and the superposed regular mesh.

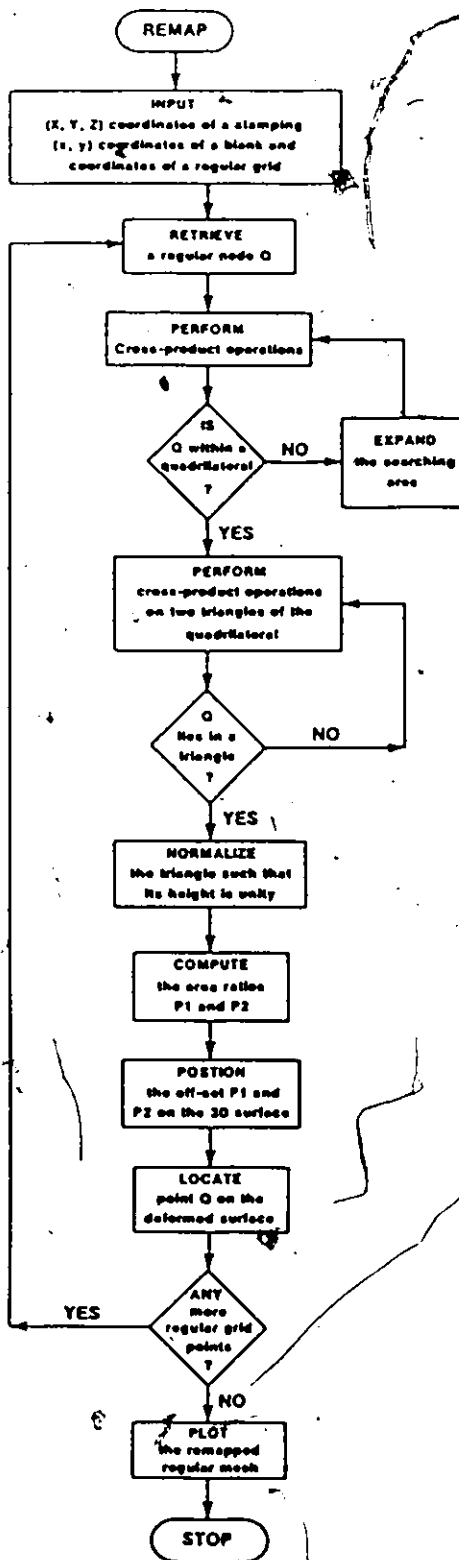


Figure 3.13: A flow chart showing the strategy involved in the remapping procedure.

stamping, or a model of the stamping, has been characterised by measuring the nodes of some topological grid. Hence points on the surface, such as A',B',C' and D' in Fig. 3.12(a), have been digitized and their spatial coordinates recorded. The selected mapping strategy then locates each surface node in the flat plane, the four aforementioned nodes are shown as A,B,C and D respectively in the flat plane, see Fig. 3.12(b). In general the mapping technique produces an irregular two-dimensional grid, and this is also shown schematically in Fig. 3.12(b). A regular square or rectangular is then superimposed on the irregular grid, and the regular grid is also illustrated in Fig. 3.12(b).

The next step is to remap the nodes of the regular grid back to generate a deformed surface. If Q is a typical nodal point of the regular mesh as shown in Fig. 3.12(b), then following the remap strategy, the point will be located as Q' on the deformed surface as illustrated in Fig. 3.12(a). A computer program called "REMAP 1" has been developed to accomplish this task, and Fig. 3.13 shows a flowchart of the strategy involved. Obviously the remapping of Q to Q' is going to involve some degree of approximation as to the actual location of Q' on the deformed surface. Hence there will be some erosion of the actual surface due to the remapping technique.

The problem of concern is to find the three-dimensional coordinates of Q' given the two-dimensional coordinates of Q. Two steps are taken to solve this problem:-

- 1) Find the triangle defined by points on the blank in which a typical

point Q of the regular grid lies.

The point Q must be tested to determine whether it is within or outside the quadrilateral ABCD, as shown in Figure 3.14, by applying a vector cross-product rule. It makes use of the fact that the area of a triangle equals half the vector cross-product of its sides, and is positive or negative according to the direction of sweeping of the enclosed angle as determined by the right-hand rule. A point is said to be within a quadrilateral if the vector cross-products of the sides of the quadrilateral all possess the same sign. For instance, in Figure 3.14, Q is within the quadrilateral ABCD and therefore the vector cross-products $\overline{QA} \times \overline{QD}$, $\overline{QD} \times \overline{QC}$, $\overline{QC} \times \overline{QB}$, $\overline{QB} \times \overline{QA}$ all have the same sign. However, a sign change of any one of these products is sufficient to indicate Q does not lie inside the quadrilateral being considered, then other quadrilaterals are tried until the quadrilateral that contains Q is found. Once the quadrilateral containing point Q is located, it is possible to find which triangle of the quadrilateral that Q is in by repeating the same sort of procedures as before. Now the point Q can then be transformed onto the surface of the stamping.

- 2) Deduce where this typical point Q would move to in space, namely to point Q' on the deep draw panel using an inverse transformation of the deformation rule with linear interpolation.

For the purpose of illustration, it is assumed that point Q lies in triangle ABC as shown in Figure 3.15(a). The problem is normalized by taking the heights of ΔABC to be unity, while the triangles ΔQAB and ΔQAC are used to define the parameters P1 and P2. The parameters P1 and

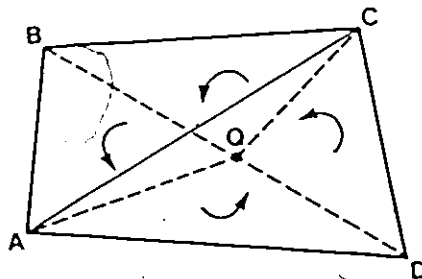


Figure 3.14: The existence of Q within the quadrilateral $ABCD$ is determined by a vector cross-product rule.

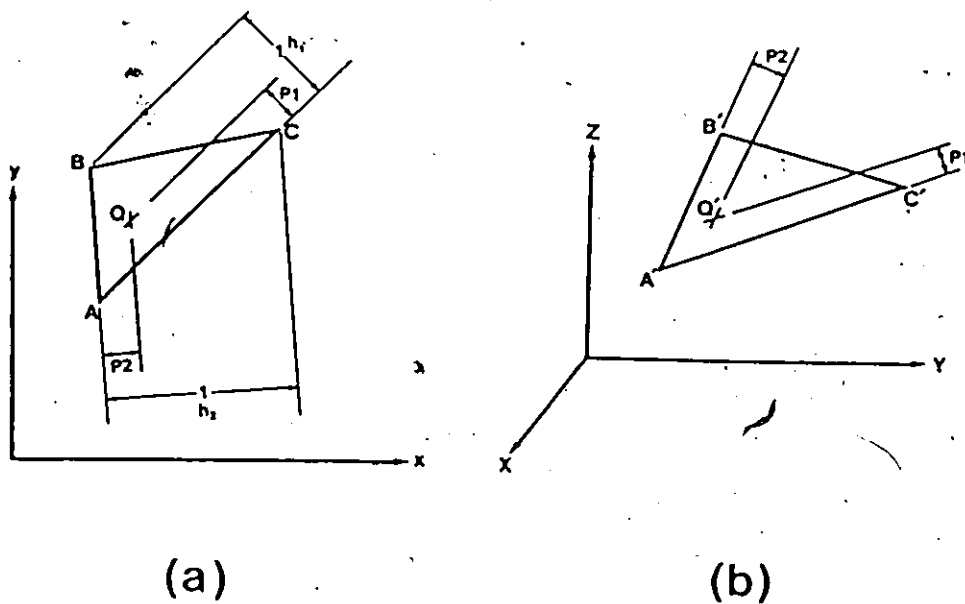


Figure 3.15: (a) Indicating the position of Q and the parameters used to define Q .
 (b) The position of Q' is determined by the corresponding area ratios $P1$ and $P2$ in space.

P2 are area ratios which are less than unity by normalization, thus the height of ΔQAC equals P1. Likewise, it is true for the area ratio P2 which represents the height of ΔQAB .

Now it is logical to assume that these area ratios will also apply to the spatial triangle formed by points A', B' and C' of the original panel. Since A', B' and C' are known points, the area ratios (P1 and P2) can be used to locate point Q' on the surface corresponding to the point Q on the blank, see Figure 3.15(b).

Suppose that the perpendicular height from Q' to side A'B' is P2 and from Q' to A'C' is P1. The parameters, P1 and P2, define the offset distance of two lines which are parallel to the base of the triangles $\Delta Q'A'B'$ and $\Delta Q'A'C'$ respectively. Upon extending these parallel lines, the location of Q' is found at the point of intersection. The geometric interpretation of the above procedures is illustrated in Figure 3.15.

The remapping of the rest of the element is conducted in a like manner. The above two procedures are part of the program "REMAP 1". Details of the program, along with a complete listing, are to be found in an internal McMaster report prepared by the present author. For complete details the reader is referred to this report [17].

3.4.1 General Comments

This section has dealt with the remapping of a regular grid to create the surface of the part. After the remapping process, the surface is represented by triangular facets whose vertices are the nodal points of the regular mesh. As mentioned in the preceding discussion

the surface created by the remapping operation is likely to be an erosion of the shape of the original stamping (or model). This arises because of the degree of approximation involved in locating the nodes of the overlaid regular mesh with respect to those of the original irregular mesh during the remapping operation. However, both the present stamping and from studies performed on other comparable stampings (one of which will be discussed in this Chapter), the remapping technique usually provided a part whose shape differed very little from the starting stamping or model.

Further details of the remapping strategy can be found in an internal McMaster University report written by Chu and Soldaat [18].

3.5 Adjustment

The element-by-element mapping method discussed in the preceding sections transfers an array of three dimensional coordinates to a two dimensional array. While the remapping strategy converts a two dimensional array back to a three dimensional array to create a surface. These mapping and remapping strategies satisfy, in an approximate manner, the rule of constant surface area, and as a consequence they are sometimes referred to as homalographic transformations.

As emphasised earlier the mapping strategy can provide a geometrically possible transformation but it does not necessarily correspond, even approximately, to the deformation experienced by the actual component. Consequently the designer must have other means of modifying the solution in the light of his own experience. While

several methods are no doubt available the two main techniques of adjustment are mentioned below.

The first is to alter the shape of the component and/or tooling in order to make the component easier to form. Many options are available, it could be through a shape change by providing extra material in a region which was splitting or tearing [19]. The design of the binder and draw beads in conjunction with the shape of the tooling can aid in the inflow of the material to overcome tearing or restrain the flow of the material to overcome both wrinkling and slackness of the part, i.e. certain regions of the part have not been deformed plastically. It is not the function of the present study to design the tooling for the creation of a sheet metal component. The objective of the work is to provide an aid to the designer and let him or her be able to test the consequences of changes in design etc. both quickly and easily. The other kind of adjustment which can readily be executed is to adjust the shape of the flat sheet after the initial mapping operation. Note that the stretching or contracting of regions of the flat sheet leads to a departure from the constant surface area hypothesis. This form of adjustment can again be likened to modifications in the binder and draw beads. Here there is no question of altering the shape of the actual part. The original irregular grid (following the mapping strategy) is adjusted in the flat plane. As described in the section on remapping, a regular grid can be overlaid on the irregular (adjusted) grid and the nodes of the regular grid remapped to form the surface. The transformation will now of course depart from

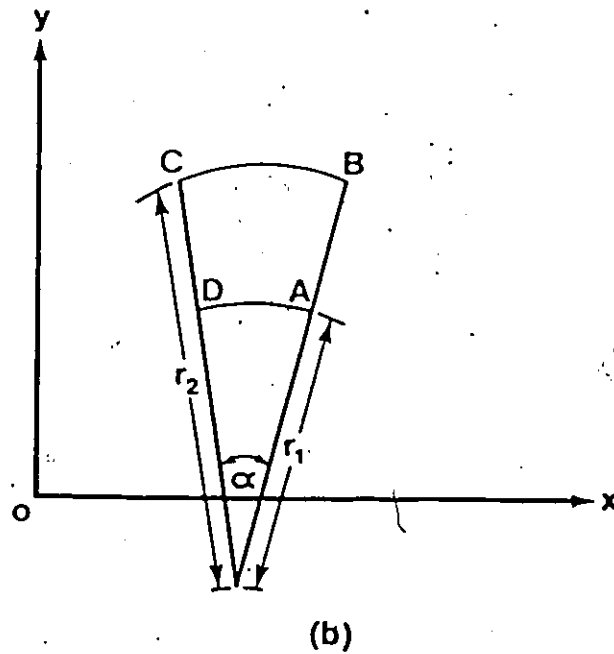
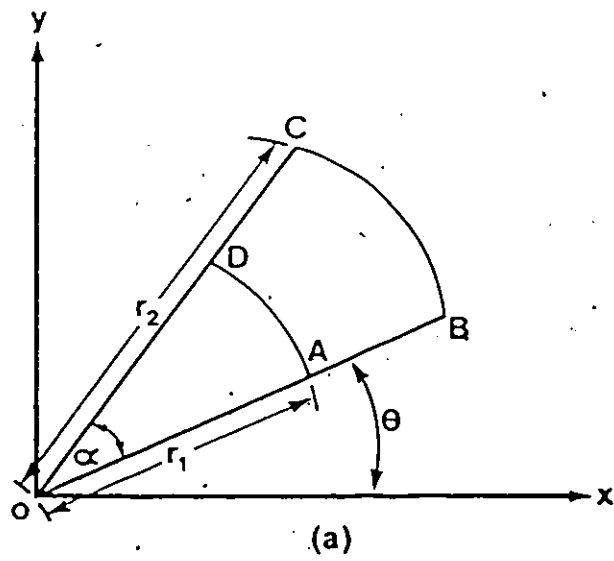


Figure 3.16: Schematic representation of adjustment methods.

- (a) Adjustment of a flat blank performed in a desired direction to the x axis.
- (b) Adjustment of an arbitrary region over the surface of a blank.

the equal area hypothesis, but the surface geometry of the part is retained.

Some procedures devoted to the adjustment of the irregular grid before remapping, are described herein.

It is illustrated in Figure 3.16(a) that an area ABCD, determined by arc lengths AD and BC and an angle of sweep α , defines a region where surface adjustment is performed. The angle, θ , allows the designer to choose a desirable location. A technique was also developed to permit the local distortion of a region within the irregular grid is required as shown in Figure 3.16(b). The former method allows the designer to perform radial adjustments only and the latter is a more general one which permits surface modification to be done in an arbitrary way. These methods allow the tool designer to smooth out strain distributions achieved from the initial mapping of the physical component. In conjunction with his own experience, the designer is able to arrive at a solution which is physically possible although it may not be an optimum one. A number of computer subroutines implemented in Fortran code are available in order to perform surface adjustment on the flat sheet. Some methods of adjustment have been performed on the hemispherical shell test case and the details can be found in Appendix C. In the present work adjustment has not been carried out on an industrial stamping. There would be no difficulty in carrying out some arbitrary form of adjustment, but it really needs the experience of a tool designer to equate the act of adjusting the flat sheet with modifications to the draw bead and binder configuration. Notwith-

standing any advantages that may occur from adjustment, confidence has first to be established with the mapping and remapping methods. This can only be achieved by applying the technique to many different industrial stampings. It is the view of the author that the adherence, in the first instance, to mapping by the equal surface area hypothesis may prove to be very useful. On a number of stampings examined by the author, portions of the component which were evidently difficult to form, e.g. the suggestion or presence of wrinkles on the part and domains where thinning was severe; these were also the regions that caused some problems when performing equal area mapping. Thus the designer is served with a warning, on the basis of homolographic mapping, that there may be some difficulty in forming the part. Alterations to the design of the part or a departure from homolographic mapping can then be introduced.

3.6 The Evaluation of Finite Strain

The mapping, remapping and adjustment techniques described in the preceding sections provide the tool designer with a computer aided package for analysing the forming of sheet metal stampings. The consequence of these various strategies on the resulting strain distribution in the part can also be predicted. The predicted strains may not correspond to those arising in an actual formed part, but they provide the designer with additional information prior to any press shop trials. The theory of finite strain, based on a homogeneous deformation mode, has been outlined in Section 2.2. This section describes in

greater detail how the principal strains are determined when the quadrilateral elements are irregular, as opposed to the hypothetical square grid as discussed in Section 2.2.

Figure 3.17 shows two arbitrary triangular elements. Figure 3.17(b) shows a triangular element on the deformed surface, e.g. the hand scribed grid, and Fig. 3.17(a) shows the same element, say after the mapping strategy. An arbitrary orthogonal set of reference axes is constructed, the vertex of the undeformed triangle coincides with the origin of the axes as shown in Fig. 3.17(a).

It has already been discussed in Chapter 2 that the coordinates (x,y) of a node can be expressed as a linear function. Hence

$$x = F_{11}X + F_{12}Y \quad (3.4)$$

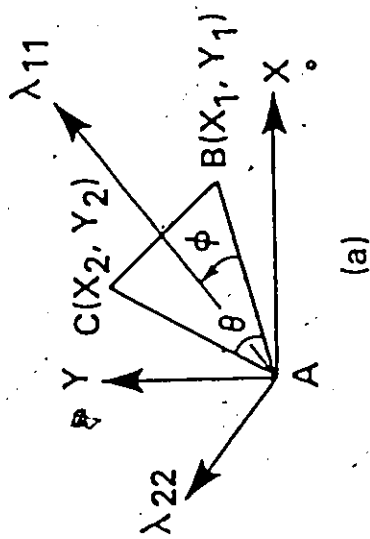
$$y = F_{21}X + F_{22}Y$$

or

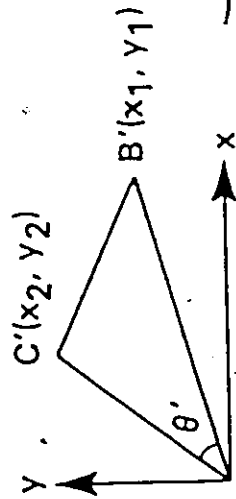
$$\bar{x} = F \cdot X \quad (3.5)$$

In general, $F_{12} \neq F_{21}$, but the four coefficients in (3.4) are constants over the region when homogeneous deformation occurs. The coefficients can be evaluated from the coordinates of three points before and after deformation, typically points A, B and C of Figure 3.17(a).

The coefficients of equation (3.4) can be determined with reference to Figure 3.17.



(a)



(b)

LEGEND

θ - INITIALLY UNDEFORMED ANGLE

θ' - DEFORMED ANGLE

ϕ - PRINCIPAL ORIENTATION

$\lambda_{11}, \lambda_{22}$ - PRINCIPAL STRETCHES

Figure 3.17: (a) Element ABC in the initially undeformed configuration.
 (b) The same element in (a) in the deformed configuration.

$$x_1 = F_{11}X_1 + F_{12}Y_1$$

$$y_1 = F_{21}X_1 + F_{22}Y_1$$

(3.6)

$$x_2 = F_{11}X_2 + F_{12}Y_2$$

$$y_2 = F_{21}X_2 + F_{22}Y_2$$

or, in the matrix form, equation (3.6) yields

$$\begin{Bmatrix} x_1 \\ x_2 \\ y_1 \\ y_2 \end{Bmatrix} = \begin{bmatrix} X_1 & Y_1 & 0 & 0 \\ X_2 & Y_2 & 0 & 0 \\ 0 & 0 & X_1 & Y_1 \\ 0 & 0 & X_2 & Y_2 \end{bmatrix} \begin{Bmatrix} F_{11} \\ F_{12} \\ F_{21} \\ F_{22} \end{Bmatrix} \quad (3.7)$$

The inversion of this matrix will result in the values of the four coefficients

$$\begin{Bmatrix} F_{11} \\ F_{12} \\ F_{21} \\ F_{22} \end{Bmatrix} = D \begin{bmatrix} Y_2 & -Y_1 & 0 & 0 \\ -X_2 & X_1 & 0 & 0 \\ 0 & 0 & Y_2 & -Y_1 \\ 0 & 0 & -X_2 & X_1 \end{bmatrix} \begin{Bmatrix} x_1 \\ x_2 \\ y_1 \\ y_2 \end{Bmatrix} \quad (3.8)$$

where $D = 1/(X_1Y_2 - X_2Y_1)$.

As already mentioned, in section 2.2 that, independent of the selected axes, the coefficients can be combined in a particular way to always yield the same components of a symmetric second order tensor, \underline{C} ,

known as Green's deformation tensor such that

$$\underline{C} = \underline{F}^T \cdot \underline{F} \quad (3.9)$$

Upon expanding the above equation, the components of the symmetric tensor are given by

$$\begin{aligned} C_{11} &= F_{11}^2 + F_{21}^2 \\ C_{12} &= C_{21} = F_{11} F_{12} + F_{21} F_{22} \\ C_{22} &= F_{12}^2 + F_{22}^2 \end{aligned} \quad (3.10)$$

Hence the principal values of the elongation ratios squared, the orientation of the principal axes and the principal logarithmic strains in the initial referential configuration are derivable respectively from

$$\begin{aligned} \lambda_{11}^2, \lambda_{22}^2 &= \frac{C_{11} + C_{22}}{2} \pm \sqrt{\left(\frac{C_{11} - C_{22}}{2}\right)^2 + C_{12}^2} \\ \tan 2\theta &= \frac{2C_{12}}{(C_{11} - C_{22})} \end{aligned} \quad (3.11)$$

and

$$\epsilon_{11}, \epsilon_{22} = \ln(\lambda_{11}, \lambda_{22})$$

The strain calculations just described are simply another aid for the designer. The complete program package including the mapping, remapping routines etc. is exemplified in Appendix D through a number of flow charts. An explanation of the purpose of each subroutine is given in Appendix E.

As already indicated the usefulness of the model can only be established after applying it to a number of industrial panels. In the following section one further example of the model is provided, as applied to an industrial stamping.

3.7 Modelling of an Automobile Inner Panel

An inner deck-lid of a mid-size vehicle was selected for this study a photograph of which is shown in Figure 2.4; the left- and right-hand sides of the panel are symmetric. An array of square elements was scribed on the metal blank prior to forming, and measurements made on the deformed and undeformed grids determine the strains distributed on the surface of the component. Details of experimental strain evaluations on the surface of the panel have been previously described in Chapter 2.

3.7.1 Mesh Generation and Boundary Conditions

An intersecting pair of grid lines (preferably orthogonal lines) has to be established on the surface before the mapping can proceed. These are lines of symmetry or dividing lines, such that points can move along these lines but not across them. On the deformed panel of Fig. 2.4 these lines, marked X and Y are settled by inspection. The designer has to decide upon the location of these boundary lines when marking the grid on the surface, and in addition he decides whether any change in line length has occurred between the nodes along these lines. The nodal position of the elements are thus known along these boundary lines in the flat plane and locating these is the first step in the mapping process.

A grid of quadrilateral elements was drawn arbitrarily on the deformed panel using a marker pen, forming an array of equal number of rows and columns, i.e. the elements are topologically rectangular. A

photograph of half of the original panel is shown in Figure 3.18, which was removed from the original stamping for the convenience of digitizing. The grid of lines marked on the surface of the component is clearly visible. (It is observed from the photograph that additional pieces of sheet metal were "added-on" to the boundaries of the panel such that the hand-drawn grid may be extended beyond the trim line. These additional pieces of metals were simply bolted onto the peripheral of the deformed part.) It will be appreciated that in order to control the panel during forming, the sheet must extend beyond the boundary of the final part to provide material for controlling tension and restraining the edges. With any moderately sophisticated computer-graphics system, this may be achieved very easily. However, advanced computer graphics have not been employed in the current study.

The mesh shown in Figure 3.18 was measured with the aid of a milling machine. It will be noticed that the area under investigation embraces the most severely distorted regions of the stamping. For convenience the gridded domain was subdivided into two regions. Each comprises a grid size of 30 x 25 which is approximately 750 nodes. A computer plot of part of the resulting mesh (left-hand side of Figure 3.18) is illustrated in Figure 3.19; the diagram provides a visual check on the digitizing.

The displacement boundary conditions in the flat plane are specified in the same manner as described in section 3.3.1(b) along the planes of symmetry XOZ and YOZ, and hence the position of the boundary nodes is readily established. The elements can now be mapped into a

flat plane using the method of the area criterion described previously; the transformation is shown in Figure 3.20. A regular mesh is shown overlaid on the resulting blank in Figure 3.21, and remapped onto the part surface. The resulting remap is shown in Figure 3.22. For completeness, the same analysis is also performed on the right-hand side of the panel as illustrated in Figure 3.18, and Figure 3.23, is the corresponding computer plot. Figure 3.24 is the resulting blank obtained from the mapping procedure; as before a regular mesh is superimposed on the irregular grid, see Figure 3.25, and is remapped to form the part surface as shown in Figure 3.26.

3.7.2 Discussion

The result of the mapping procedure for the complete stamping illustrated in Figure 3.18, is shown in Figure 3.27. The uneven edges of the blank suggest that the modelling is not very realistic; nevertheless, the practical importance of this is that the developed flat shape could be considered as an initial blank. This blank, at least theoretically, can be made to conform to the surface in Figure 3.18 in such a way that the area criterion imposed previously is satisfied. It should be noted that the blank generated is not the only one since it has been demonstrated in Appendix C that the mesh size and shape is likely to play an important role when attempting to represent the surface geometry of a complex pressing. It can be seen from Figure 3.18 that the hand-drawn elements are relatively coarse and irregular. These produce large errors in the calculations of the basic variables of a triangle, particularly in the regions of high strain gradient.

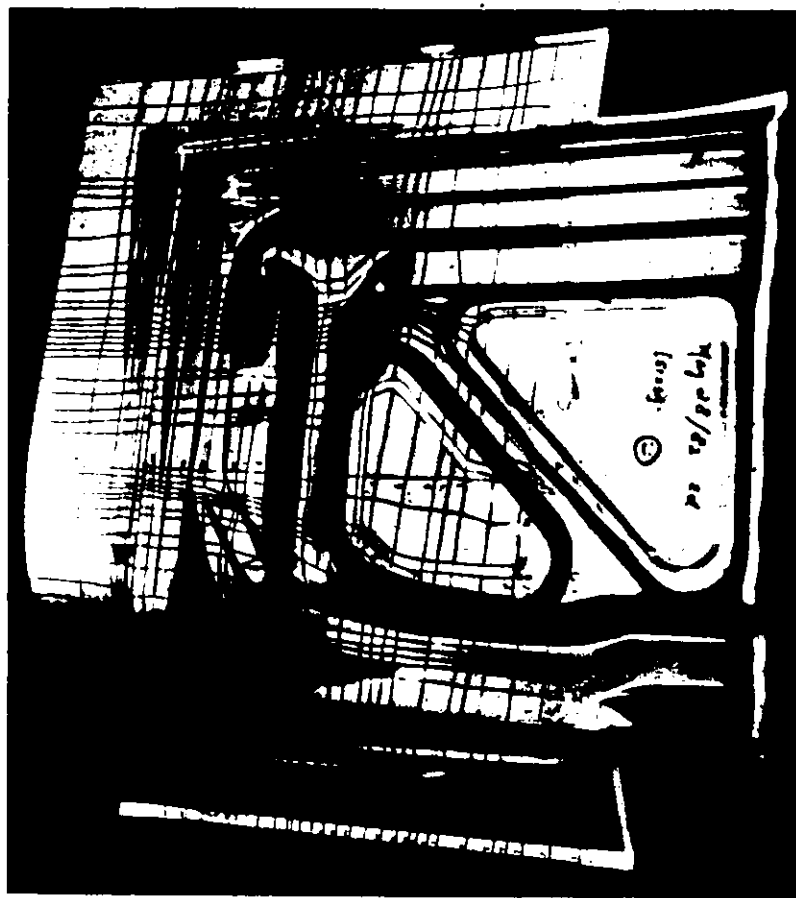


Figure 3.18: A photograph of part of an industrial stamping in Fig. 2.4 onto which an irregular mesh was constructed with a marker pen.

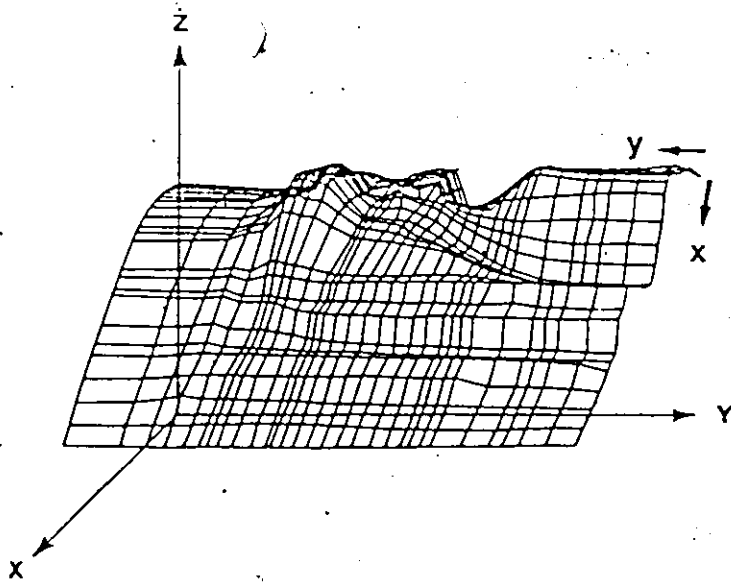


Figure 3.19: Isometric projection of the left-hand irregular mesh shown in Fig. 3.18.

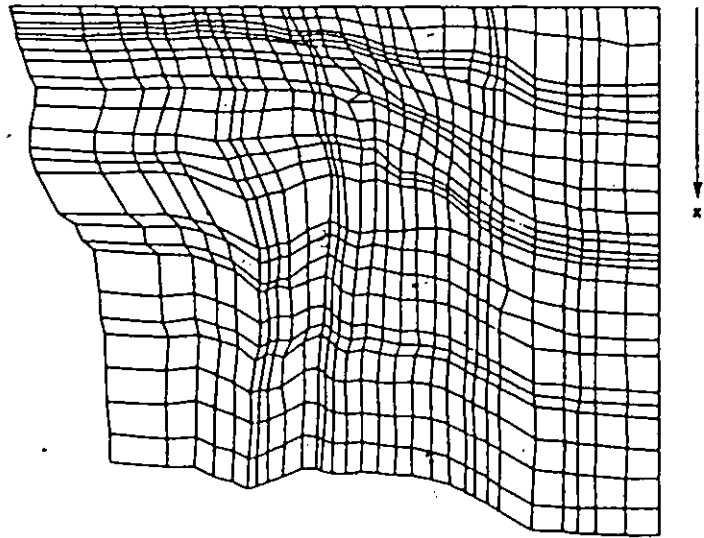


Figure 3.20: "Constant area" mapping of the element in Fig. 3.19 onto a plane.

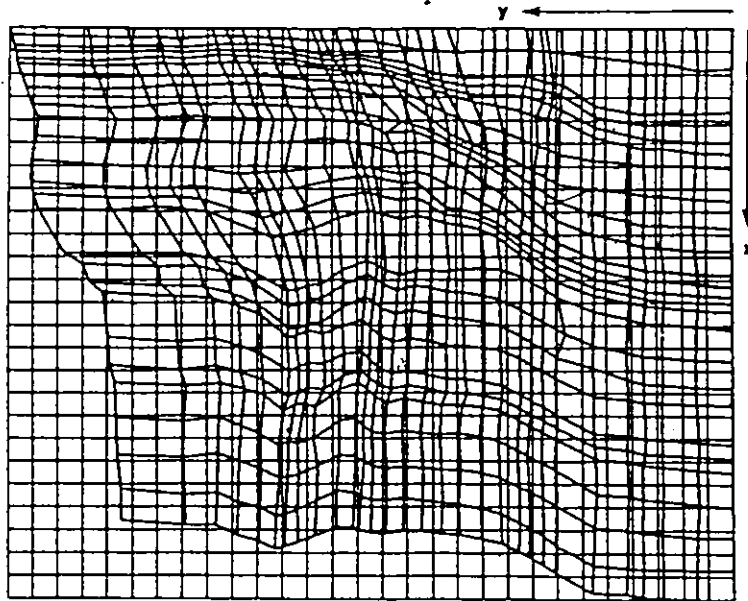


Figure 3.21: Superimposing an array of rectangular elements on the resulting map in Fig. 3.20.

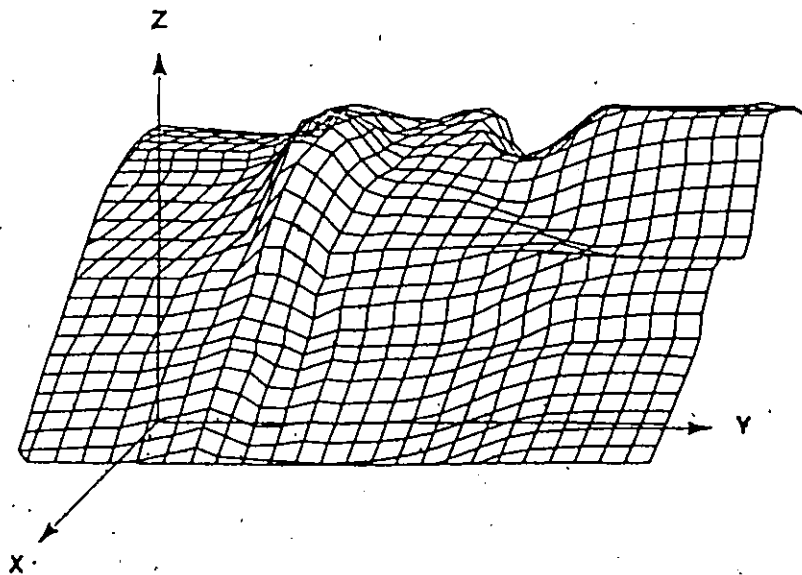


Figure 3.22: Remapping of the regular mesh onto the part surface.

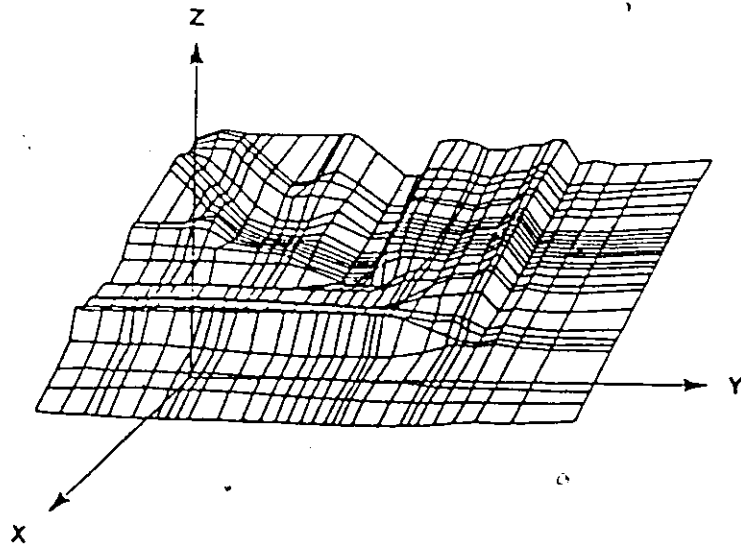


Figure 3.23: A computer plot of the right-hand irregular mesh on the surface of the deck-lid in Fig. 3.18.

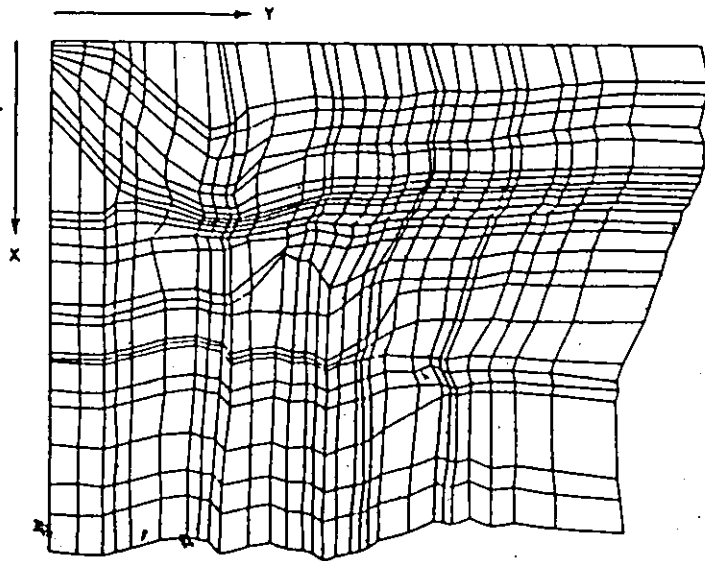


Figure 3.24: The mapping of "constant area" irregular patches onto a plane.

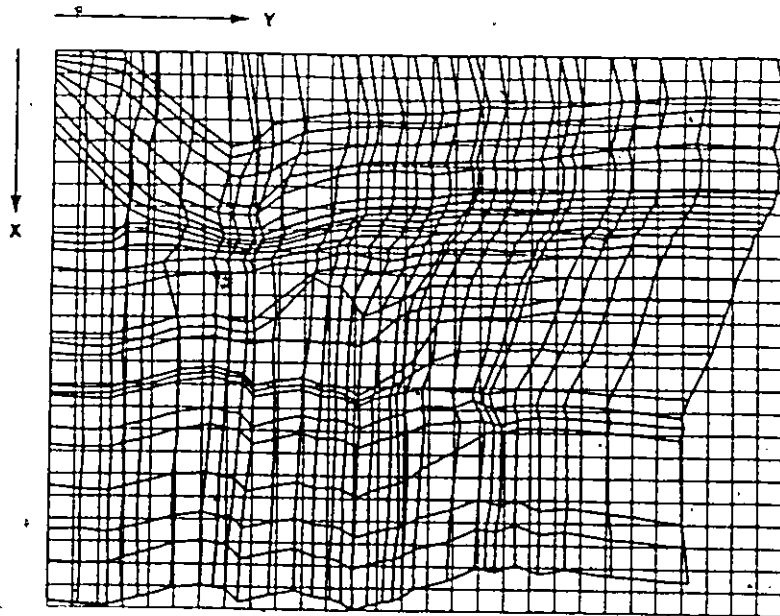


Figure 3.25: Overlapping of a regular mesh on the blank with equal number of elements.

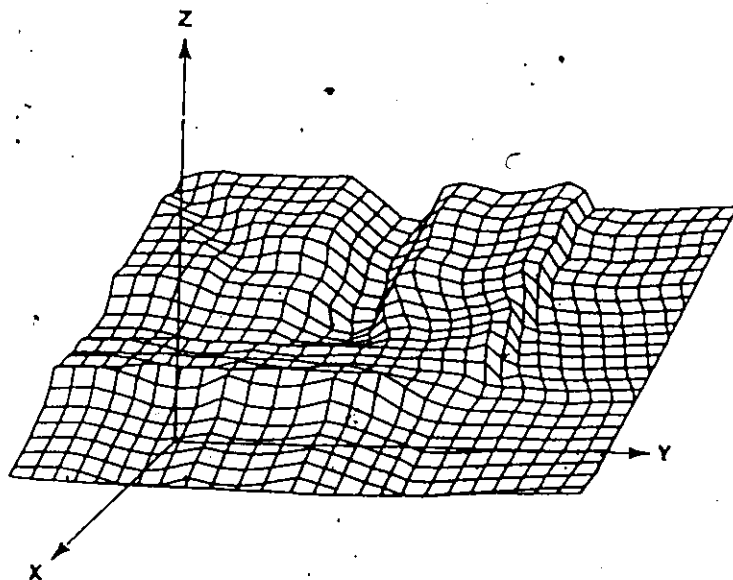


Figure 3.26: Remapping of the regular elements in Fig. 3.25 onto the part surface.

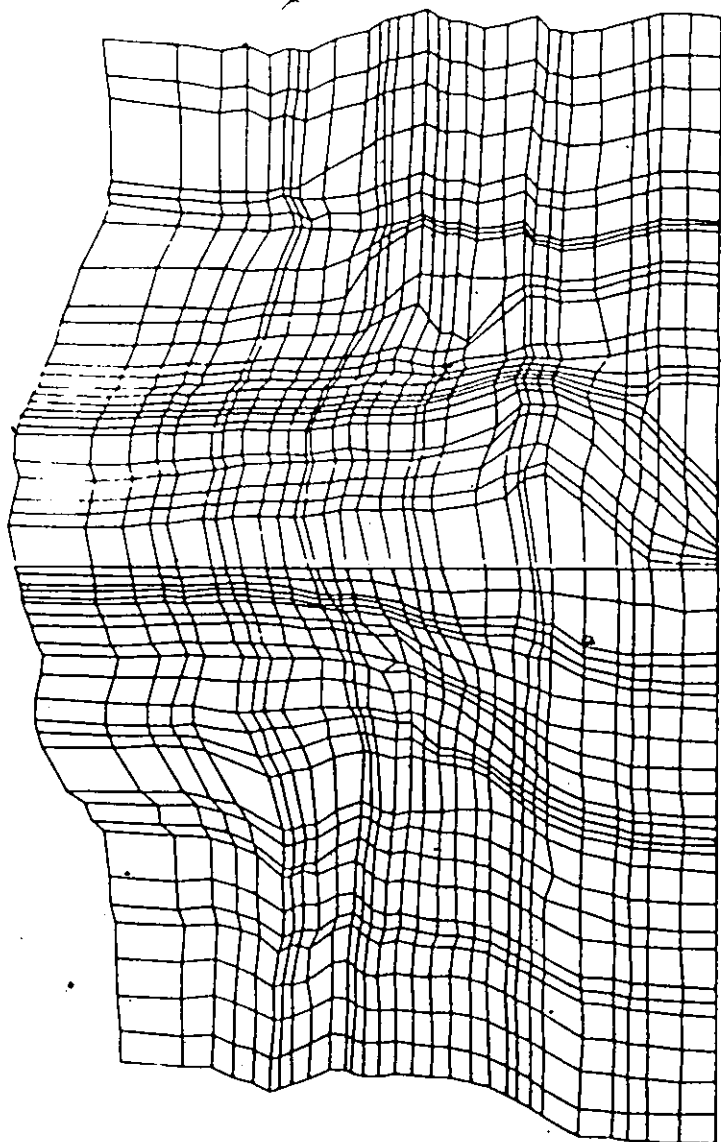


Figure 3.27: The entire resulting transformation of the hand drawn irregular mesh in Fig. 3.18 onto a flat plane.

The surface obtained by remapping of the regular grid mesh (see Figs. 3.22 and 3.26) is a smoothed version of the part surface since the remapped nodes of the regular mesh do not represent precisely the original surface, particular in region of drawing-in. The erosion of the surface becomes more significant if a coarse mesh is used to represent the part surface, a corner or bend cannot be defined accurately by plane triangular elements and that points within the triangles do not lie on the actual part surface after remapping and hence sharp corners will be eroded away. Better results might have been obtained if smaller elements had been employed in areas where sharp bends were present; however, a finer mesh may become very impractical and difficult to measure. An examination of the resulting remap grids provide a good indication of how the sheet should form to achieve the constant area deformation. For the purpose of clarity, the results of the remapping shown in the above figures were also transferred to the actual stamping and as already mentioned in Chapter 2 that holes were drilled through the two identical panels in order to provide some local reference positions. These drilled holes were again utilized here to establish the remapped points on the part surface. With nodes of the hand drawn irregular mesh as reference, then regular grid points were manually located on the surface of the panel shown in Figure 3.18 and the relative positions of these points with respect to drilled holes established. Knowing the relative locations of the nodes the resulting remapping could then be constructed on the second panel where positions of drilled holes were marked. The resulting transformation is illus-

trated in Figure 3.28 and the following photographs show some interesting features. In Figure 3.28, there is a region indicated by the arrow where the shape of the part creates a local increase in area. To satisfy this, material must be fed in from the edge. One cannot push on the edge of the sheet but in this case, the tool designer has provided draw beads near the corners to restrain the sheet here and these beads are omitted in the middle to encourage feeding in the region indicated. The direction of material flow is clearly illustrated by the deformation of the regular mesh shown in the photograph and because the remap approximates a constant area transformation the material inflow is greater than what has actually happened. The remapped grid also provides a guide line to the designer such that he may decide upon where draw beads should be imposed on the sheet for controlling tension.

The stamping has not been trimmed and was formed originally from a rectangular sheet. If the deformed mesh accurately modelled the actual deformation, grid lines at the edge would be parallel to the edge of the metal. This is approximately so as illustrated in Figure 3.29 and measurement around the whole region modelled showed that the edge of the mapped grid departed by, at most, 4% of the blank width from the actual metal edge.

The strain distributions measured by the usual circle grid method on the actual part and those computed from the mapping process are compared in Figure 3.30. This shows the contours of effective strain and while it may be seen that the character of the strain distribution and magnitudes in the actual and modelled cases differ, the regions of



Figure 3.28: Photograph of the deck lid onto which the regular grid in Figs. 3.22 and 3.26 has been transferred. (The features in the region indicated have a large surface area.)

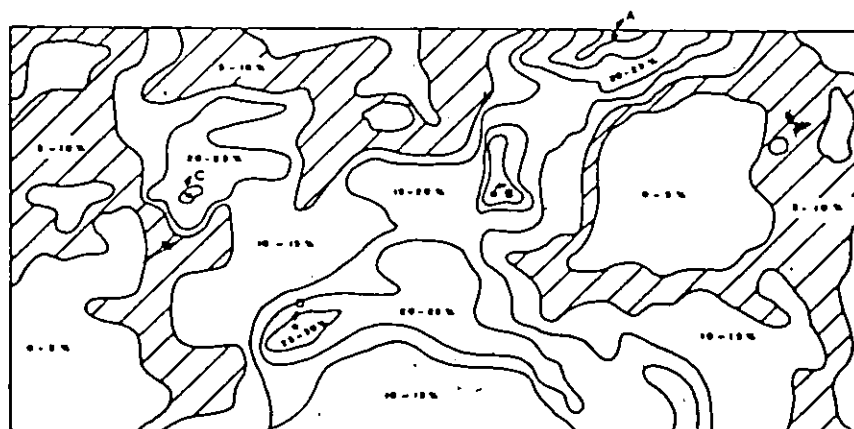


Figure 3.29: Photograph showing the approximate agreement between the regular mesh and the edge of the stamping produced from a rectangular blank.

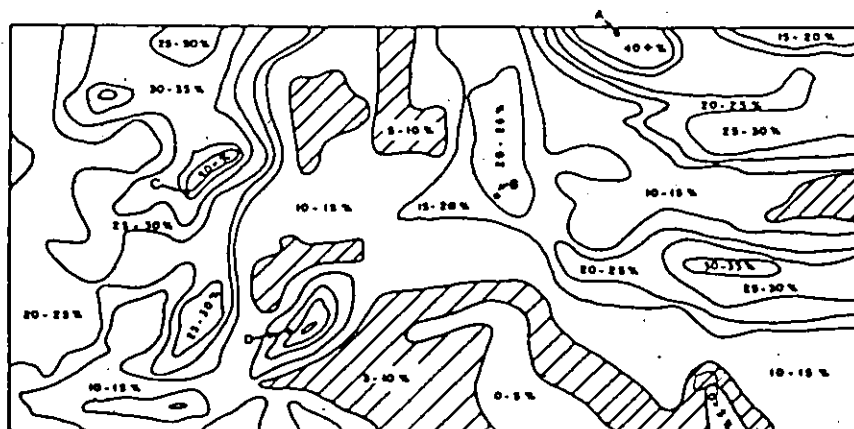


(a)

Figure 3.30: (a) Photograph of an automotive inner deck-lid panel showing positions of peak strain for comparison.



(b)



(c)

Figure 3.30: (b) Contours of effective strains obtained from measurement of 0.2 in diameter grid circles on the panel.
 (c) Contours of effective strains computed from the remapped regular mesh illustrated in Fig. 3.28 (region of points of peak strain, A to D are given in (a)).

peak strains in both cases coincide. The designer can impose adjustments on the strain distribution in order to obtain a physically more feasible design.

3.8 Conclusions

Experience needs to be obtained to determine the usefulness of the modelling technique, however it has been shown that a geometrically admissible transformation can be produced between a flat sheet and a formed part using the method of constant area patches. Computation times for the mapping and remapping procedures are relatively small. In the present case, it required about 35 seconds on the McMaster Cyber 170/730 Central Computer to provide the results shown in Figures 3.27 and 3.28. It suggests that the technique is suitable for an interactive die design system.

The method is purely geometric and does not take account of equilibrium or of material properties. The mapping is guided by arbitrary instructions from the designer but even without adjustment, the results obtained on a complicated stamping appear to be very useful. In the hands of an experienced tool designer, it is expected that this will become a useful method of improving the speed and accuracy of tool design and will reduce the cost of tooling try-out and development.

The predictions of the current die design technique reveal certain physical features occurred in the actual pressing. In the present study, restrictions have not been imposed on the movement of the material at the boundaries, such as draw beads and the like in the

stamping operation. Consequently, the predicted inflow of the material in certain regions will be larger than that which actually occurs in practice. This is a constraint which the designer could incorporate by performing adjustment on the regular grid mesh before applying the remapping process. By exercising this, the analysis done by the designer is performed as if draw beads were added on certain selected areas of the part. This creates tensions and restricts the inflow of the material of the sheet, thus providing better control of the flow of the material.

CHAPTER 4

ON THE RATES OF STRESS AND STRAIN MEASURES IN FINITE DEFORMATION

4.1 Introduction

In plasticity any strain determined solely from the initial and final shape of any observable element cannot be regarded as a state parameter. The material state depends not only on the change in shape, but also on the path along which the shape evolved [5,6]. For rate-independent solids, the assumption of isotropic hardening can lead to a simple relationship between the current representative stress (a measure of the size of the yield surface) and the integral of the representative strain increment, $\int d\bar{\epsilon}$. As is well known $d\bar{\epsilon}$ is a multiple of the second invariant of the plastic strain increment tensor. This is an Eulerian description of the strain, since the components are measured with respect to the current configuration. The strain increment comprises an elastic and a plastic part, and a number of investigators, see Refs [20-23], have discussed how these parts should be decomposed. The point is not pursued here.

In sheet metal forming processes, the deformed component can experience large deformations, which may be essentially inhomogeneous in nature. However, in order to obtain a simple measure of strain, the investigator is anticipating that the straining will occur by homogeneous deformation over a small local neighbourhood. Under this postulation a square element will deform into a parallelogram, a circle

into an ellipse and a sphere into an ellipsoid. The assumption of linear mapping is also embodied in theoretical studies of the geometry of deformation, it is merely a matter of scale as to whether the domain of inspection is considered infinitesimal or finite in extent. This presents no problems from a theoretical point of view, but in practice the elements are finite and inhomogeneous straining may arise within the boundary of a single element.

If the straining takes place by pure homogeneous deformation (pure stretching), the deformation gradient tensor is symmetric and there exists within a deforming cell an orthogonal triad which remains orthogonal throughout the deformation history. Without ambiguity this triad represents the principal axes, and they remain fixed in space* while all other line elements rotate. From the components of the deformation gradient tensor, the orientation and magnitude of the principal stretches is readily determined. The total representative strain is then a function of the natural logarithm of the principal stretches. In pure stretch processes, it is sufficient to measure solely the initial and final shape of a grid element in order to evaluate the principal stretches. It is for the case of pure homogeneous deformation that Hill [24-26] proposed the tensor logarithm as a conjugate strain measure in his work on constitutive inequalities.

When the straining occurs by homogeneous deformation the deformation gradient tensor, say F , is unsymmetric. However, an orthogonal

* The superposition of a rigid body rotation on the deformation by some other agency is not considered.

triad can still be identified in the initial configuration (the Lagrangian state) which is also orthogonal in the final (the Eulerian state) configuration. It must be emphasized that this triad has not remained orthogonal throughout the deformation history, it undergoes rotation and it is a moot point whether the name principal should be ascribed to this triad.

When \underline{F} is unsymmetric, this causes some problems in the evaluation of the strain, and recourse is made to techniques to devise a symmetric tensor. The polar decomposition theorem allows \underline{F} to be expressed as either $\underline{F} = \underline{R} \cdot \underline{U}$ or $\underline{F} = \underline{V} \cdot \underline{R}$. The tensors \underline{U} and \underline{V} represent pure deformation and are referred to as the right and left stretch tensor respectively, while \underline{R} provides a rigid body rotation and $\underline{R}^T = \underline{R}^{-1}$. It follows that $\underline{U}^2 = \underline{F}^T \cdot \underline{F}$ and $\underline{V}^2 = \underline{F} \cdot \underline{F}^T$, and it is deemed that the eigenvectors of \underline{V}^2 define the orientation of an orthogonal triad in the current configuration and those of \underline{U}^2 define the orientation of the same triad in the initial configuration. To the associated strain ellipsoids, Hill [25,26] has ascribed the name Eulerian (for the current strain ellipsoid) and Lagrangian (for the initial strain ellipsoid).

The above method of decomposition is an artifice. Real deformation processes do not occur, in general, by some combination of pure stretch and rigid body rotation or vice-versa. Nevertheless, the above theorem is unique mathematically and since the tensor \underline{F} may be regarded as a smooth and continuous function over a sufficiently small neighbourhood of interest, the polar decomposition could be applied to a

wide range of practical problems. The components of \underline{F} are functions of time and spatial position. However, in principle if \underline{F} is known, in the above sense, the deformation is uniquely defined. It follows from the polar decomposition theorem that either one of the pure stretch tensors \underline{U} and \underline{V} when acting alone will give the same shape change as \underline{F} . The same change in shape does not imply identical straining modes as discussed in Chapter 2. Sowerby and Chakravarti [6] have demonstrated that pure homogeneous deformation (pure stretch) processes minimise the accumulated representative strain, $\bar{\epsilon}$, vis à vis the homogeneous deformation mode (unsymmetrical \underline{F}) which produces the same shape. This fact would not be realised through any of the aforementioned schemes which produce a symmetric tensor.

The difference in representative strain when the actual deformation, \underline{F} , is replaced by the multiplicative decomposition, $\underline{F} = \underline{R} \cdot \underline{U} = \underline{V} \cdot \underline{R}$ depends on the extent of the deformation. For infinitesimal deformation increments, no distinction will be revealed, because the antisymmetric part of the deformation is ignored when defining infinitesimal strains. In numerical schemes such as finite element methods, the error is likely to be negligible for small deformation steps. In fact, it may not be necessary to attempt to distinguish between homogeneous deformation and pure stretch in practical sheet metal forming operation, at least as far as representative strain is concerned. As already illustrated in Chapter 2, a simple calculation for the simple shear process, and also when the shape change is achieved by pure stretch, demonstrates there is about 10 percent difference in

the representative strain based on a shear displacement of 1.5. This would represent a large strain in sheet forming and an accumulated $\bar{\epsilon}$ of about unity. It will be realized that in real forming process the straining path is usually unknown, and therefore if an estimate of the strain is required the only recourse is to assume a pure stretch mode.

As already mentioned, when the process is one of pure stretch, the logarithmic (natural) strain is an appropriate strain measure. Furthermore, for the pure stretch mode the material derivative of the tensor logarithm, i.e., $(\dot{\ln U})$, is equal to the rate of deformation tensor, D . Such a simple expression does not hold when the deformation gradient tensor, F is unsymmetric, but Gurtin and Spear [27] derived a relationship for arbitrary homogeneous deformation modes. Similar results are developed in the present chapter, but a different analytical approach is adopted. The utility of the resulting expressions in any numerical scheme has still to be demonstrated. The expressions involve the spin of the triad of the Eulerian and Lagrangian ellipsoids. The spins of the ellipsoids have been developed by Biot [28] and more recently by Hill [25,26] when an infinitesimal deformation step is superimposed on finite stretches, and similar calculations are repeated here but from a different standpoint. In turn, the Lagrangian and Eulerian rates of strain are related to the corresponding spins.

Another aspect of the present Chapter is concerned with the choice of an appropriate stress rate to be used in constitutive equations for materials undergoing finite deformation. It has long been realized that when a material element experiences large deformation, the

components of stress vary as a result of material rotation. These changes occur even in the absence of additional strain. Apparently, Zaremba [29,30] was the first to discover that when computing the rate of change of stress it is necessary to account for the effect of material rotation. Since then alternative definitions of stress rate have been introduced by many investigators [31-34]. Yet, many seem to have ignored the case when material axes become strongly skewed owing to finite deformation and rotation. Recently, Dienes [35] has discussed this phenomenon and proposed a stress rate tensor to account for the skewing effect.

In finite deformation different "rotation" tensors can be defined. Consequently a wide choice of objective stress rates is available for adoption in constitutive equations. It is of interest to ascertain the influence of the stress rate on the evolution of the stresses in a deforming body. In this chapter a number of different stress rates are proposed and these can be shown to be objective. The utility of the resulting expressions is demonstrated for the case of a hypoelastic material undergoing finite deformation in simple (rectilinear) shear.

4.2 Some Theoretical Fundamentals

For simplicity, the analytical framework will be expressed in direct tensor notations in which the tensor can be referred to its

A material is said to be hypoelastic if the components of stress rate are homogeneous linear function of the components of the rate of deformation.

basis. Second order tensors are indicated by an underscore tilde on a letter while vectors are indicated by a superposed bar on a letter. Some basic equations describing the deformation process are outlined below.

4.2.1 Deformation Gradient

The deformation of an infinitesimal neighbourhood $d\bar{x}(t)$ in the deformed body V as shown in Figure 4.1 may be related to the initially undeformed body by a linear affine mapping of the form (the Lagrangian description).

$$d\bar{x}(t) = \underline{\underline{F}}(t) \cdot d\bar{X} \quad (4.1)$$

where $d\bar{x}(t)$ and $d\bar{X}$ denote the current and initial positions of material points and $\underline{\underline{F}}(t)$ is the deformation gradient tensor which is defined as

$$\underline{\underline{F}}(t) = \frac{\partial \bar{x}(t)}{\partial \bar{X}}, \quad (4.2)$$

and its transpose is given by

$$\underline{\underline{F}}(t)^T = \frac{\bar{x}(t) \partial}{\partial \bar{X}} \quad (4.3)$$

At any given time, t , $\underline{\underline{F}}(t)$ is a 3×3 matrix (for a three dimensional case) whose determinant is strictly positive and hence admits the polar decomposition

$$\underline{\underline{F}}(t) = \underline{\underline{R}}(t) \cdot \underline{\underline{U}}(t) = \underline{\underline{V}}(t) \cdot \underline{\underline{R}}(t) \quad (4.4)$$

In the above equation $\underline{\underline{U}}(t)$ and $\underline{\underline{V}}(t)$ represent pure deformations and are referred to as the right and left stretch tensors respectively, while $\underline{\underline{R}}(t)$ is an orthogonal tensor characterizing the rigid body rotation

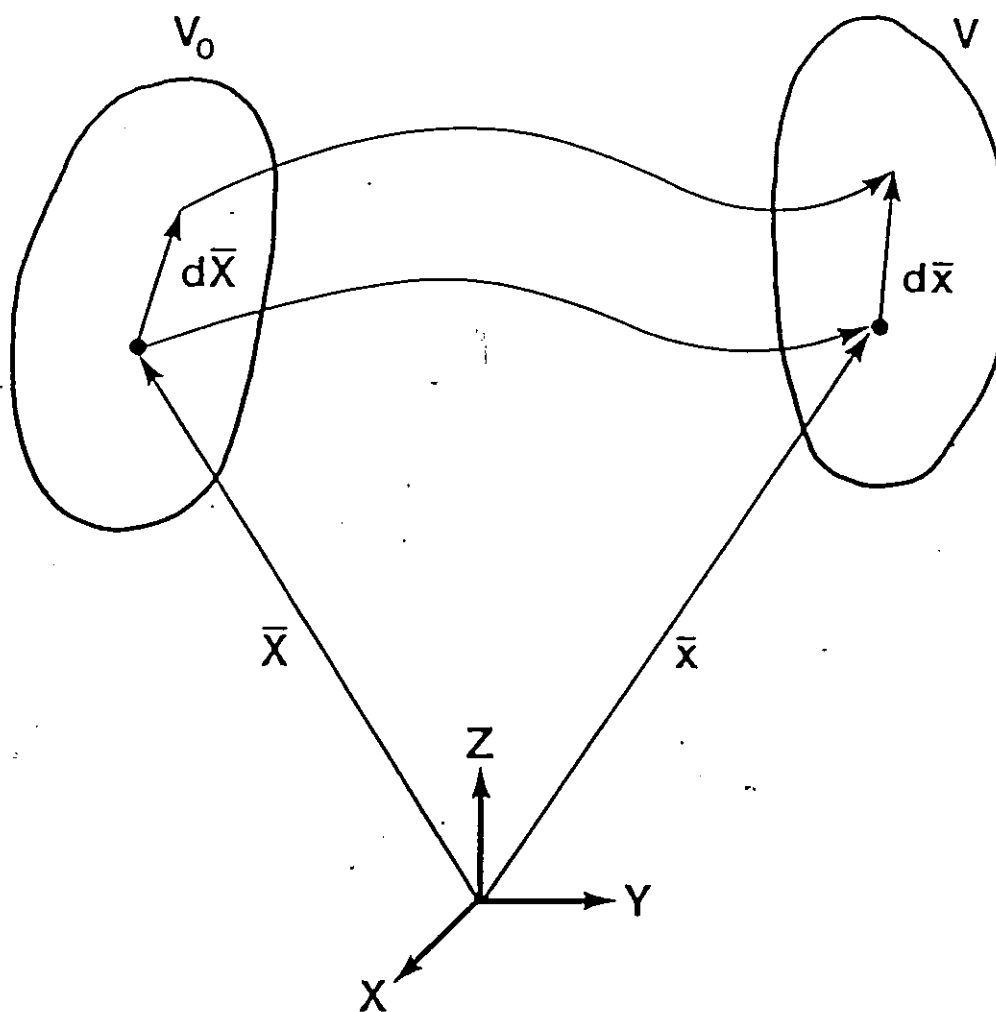


Figure 4.1: Diagram illustrating the deformation of the vector $d\bar{X}$.

where

$$\underline{R}(t)^T = \underline{R}(t)^{-1}$$

and

$$\underline{R}(t) \cdot \underline{R}(t)^T = \underline{1} \quad (4.5)$$

where $\underline{1}$ is an identity tensor. It follows from (4.4) and (4.5) that

$$\underline{U} = \underline{R}^T \cdot \underline{V} \cdot \underline{R} \quad (4.6)$$

and omitted hereinafter is the notation indicating the dependence of these tensors on time. Furthermore \underline{U} can be expressed as

$$\underline{U} = \underline{P} \cdot \underline{\lambda} \cdot \underline{P}^T \quad (4.7a)$$

or

$$\underline{\lambda} = \underline{P}^T \cdot \underline{U} \cdot \underline{P} \quad (4.7b)$$

where $\underline{\lambda}$ is the diagonal tensor (matrix) of \underline{U} whose components are the principal stretch values (eigenvalues). The entity \underline{P} is another orthogonal tensor, $\underline{P}^{-1} = \underline{P}^T$, with the unit eigenvectors (principal directions) of \underline{U} as columns of the matrix. It can be shown [6,36] that

$$\ln \underline{U} = \underline{P} \cdot \ln \underline{\lambda} \cdot \underline{P}^T \quad (4.8)$$

This relation suggests that the components of a tensor logarithm transform exactly like ordinary tensor transformation.

4.2.2 Velocity Gradient

Utilizing the concept of material time derivative, the Eulerian description of the process is given by

$$d\bar{v} = \underline{L} \cdot d\bar{x} \quad (4.9)$$

where \underline{L} is the spatial velocity gradient tensor and is equal to

$$\underline{L} = \dot{\underline{F}} \cdot \underline{F}^{-1} \quad (4.10a)$$

and

$$\underline{L} = \underline{D} + \underline{W} . \quad (4.10b)$$

The instantaneous rate of change of elements in the deformed configuration is usually defined in terms of the rate of deformation tensor (stretching tensor) \underline{D} . It is the symmetric part of the velocity gradient tensor, and the antisymmetric part \underline{W} is termed the spin tensor. Hence

$$\begin{aligned} \underline{D} &= (\underline{L} + \underline{L}^T)/2 \\ \underline{W} &= (\underline{L} - \underline{L}^T)/2 . \end{aligned} \quad (4.11)$$

Equation (4.9) can be solved explicitly to reveal (4.1), if the components of \underline{L} are constants in the chosen time interval. In a similar manner to (4.7) it is formally possible to write

$$\underline{F} = \underline{P} \cdot \underline{A} \cdot \underline{P}^{-1} \quad \text{or} \quad \underline{A} = \underline{P}^{-1} \cdot \underline{F} \cdot \underline{P} \quad (4.12)$$

where \underline{A} is the diagonal tensor of the eigenvalues of \underline{F} and \underline{P} the associated tensor of the eigenvectors. Note in this case \underline{F} is not symmetric and hence the eigenvalues need not be real nor are the eigenvectors orthogonal. It has already been discussed in Chapter 2 that (4.10a) could be integrated as

$$\underline{L}^* = \int \underline{L} dt = \ln \underline{F} ,$$

and in view of (4.8) and (4.12)

$$\underline{L}^* = \underline{P} \cdot (\ln \underline{A}) \cdot \underline{P}^{-1} . \quad (4.13)$$

The solution to the right hand side of the above equation has been given in Chapter 2 for finite homogeneous deformation processes for the special case when the components of \underline{L} are constants, i.e. a homogeneous velocity field. In practice the components of \underline{L} are not known directly.

Hence the components of \underline{L}^* , in (4.13), are expressed in terms of the components of \underline{F} , since it is these latter quantities which are usually determined following some deformation step. Typically this is accomplished by measuring a grid of lines which have been previously marked on the surface of the component or workpiece.

In Ref. [6] a proposal is made for making the \underline{L}^* matrix symmetric, and then calculating the resulting representative strain. The technique is shown to be equivalent to splitting up the finite deformation into a large (infinite) number of incremental steps, to calculate at each step the representative strain increment and to sum these for the total representative strain.

When \underline{F} is symmetric, the components of \underline{L}^* are given by the transformation of a diagonal matrix whose components are the principal natural (logarithmic) strains. This will be apparent by recognising that the right hand side of (4.13) is now identical to (4.8).

4.3 Some Basic Measures of Stress and Strain

Some fundamental definitions of appropriate measures of stress, strain and their rates, which may be employed in the basic formulation of finite deformation problems for either elastic or elastic-plastic solids are presented herein. Often it is convenient to choose an Eulerian stress measure which is associated with an Eulerian strain or the rate of deformation tensor \underline{D} . The stress and the associated strain is usually called a conjugate pair.

4.3.1 Conjugate Variables

Consider the possibility of having various stress and strain pairs all giving the same rate of work per unit volume of material.

Define the rate of work done by the Cauchy stress per unit current volume of material as

$$\dot{w}(\underline{\sigma}) = \underline{\sigma} : \underline{L} = \underline{\sigma} : \underline{D} \quad (4.14)$$

where $\underline{\sigma}$ is the Cauchy stress tensor.

Observe that the rate of internal work per unit reference volume remains unchanged from (4.14) if we write

$$\dot{w} = J \underline{\sigma} : \underline{L} = \underline{\tau} : \underline{L}, \quad (4.15)$$

where $J = \rho_0 / \rho$ is called the Jacobian; ρ_0 and ρ are the densities in the undeformed and deformed configuration respectively. In the above $\underline{\tau}$ is the Kirchhoff stress tensor, which is related to the Cauchy stress as follows

$$\underline{\tau} = J \underline{\sigma} \quad (4.16)$$

Some well-known conjugate stress and deformation measures satisfying equations (4.15) are summarized below, see Refs. [24, 37] for further details. It can be shown that

$$\underline{I} : \dot{\underline{F}} = \underline{S} : \dot{\underline{E}} = \underline{t} : \dot{\underline{e}} = \underline{\tau} : \underline{D} \quad (4.17)$$

where the pseudo-stress tensors are

$$\begin{aligned} \underline{I} &= \underline{F}^{-1} \cdot \underline{\tau} && - \text{the first Piola-Kirchhoff stress tensor;} \\ \underline{S} &= \underline{F}^{-1} \cdot \underline{\tau} \cdot \underline{F}^{-T} && - \text{the second Piola-Kirchhoff stress tensor;} \\ \underline{t} &= \underline{F}^T \cdot \underline{\tau} \cdot \underline{F} && - \text{the covariant Kirchhoff stress tensor;} \end{aligned}$$

and

$$\underline{E} = (\underline{F}^T \cdot \underline{F} - \underline{1})/2 \quad - \text{Green's strain tensor;}$$

$\underline{\underline{\epsilon}} = (\underline{\underline{1}} - \underline{\underline{E}}^{-1} \cdot \underline{\underline{E}}^{-T})/2$ - the Almansi strain tensor.

4.3.2 Stress Rates

The material time rate of change of a tensor $\underline{\underline{\xi}}$ is given by

$$\dot{\underline{\underline{\xi}}} = \frac{\partial \underline{\underline{\xi}}}{\partial t} + \bar{\underline{\underline{v}}} \cdot \frac{\partial \underline{\underline{\xi}}}{\partial \bar{\underline{\underline{x}}}} \quad (4.18)$$

where $\bar{\underline{\underline{v}}} = \bar{\underline{\underline{v}}}(\bar{\underline{\underline{x}}}, t)$ is the spatial description of the velocity field and the material rate operator (spatial description) is expressed as

$$\frac{d}{dt} = \frac{\partial}{\partial t} + \bar{\underline{\underline{v}}} \cdot \frac{\partial}{\partial \bar{\underline{\underline{x}}}} \quad (4.19)$$

The above relationships are helpful when analyzing various types of stress rates. For any arbitrarily chosen region the conservation of mass requires that $\dot{m} = 0$, and this condition can be expressed by the equation of continuity,

$$\dot{\rho} + \rho \frac{\partial \cdot \bar{\underline{\underline{v}}}}{\partial \bar{\underline{\underline{x}}}} = 0 \quad (4.20)$$

When analyzing stress rates, it is necessary to evaluate the material rate of change of the density ratio ρ_0/ρ , where ρ_0 is the initial density and independent of position. In view of equations (4.19) and (4.20), we obtain

$$\left(\frac{\rho_0}{\rho}\right) \cdot = \frac{\rho_0}{\rho} \frac{\partial \cdot \bar{\underline{\underline{v}}}}{\partial \bar{\underline{\underline{x}}}}$$

or

$$\dot{J} = J(\underline{\underline{L}} : \underline{\underline{1}}) \quad (4.21)$$

Consider taking the material rate of change of the first

Piola-Kirchhoff stress such that

$$\dot{\underline{T}} = J\dot{\underline{F}}^{-1} \cdot \{ \dot{\underline{\sigma}} - \underline{L} \cdot \underline{\sigma} + \underline{\sigma}(\underline{L} : \underline{1}) \}, \quad (4.22)$$

while the material derivative of the second Piola-Kirchhoff stress tensor results in

$$\dot{\underline{S}} = J\dot{\underline{F}}^{-1} \cdot \{ \dot{\underline{\sigma}} - \underline{L} \cdot \underline{\sigma} - \underline{\sigma} \cdot \underline{L}^T + \underline{\sigma}(\underline{L} : \underline{1}) \} \cdot \underline{F}^{-T}. \quad (4.23)$$

Many more stress rates can be formulated, other possible measures are those which are observed in coordinate system which deforms and moves together with the material i.e., the convected coordinates. For completeness some well-known measures of stress-rates are given below without proof, for further details the readers are referred to Ref. [38]. The Cauchy stress rate is defined as

$$\dot{\underline{\sigma}}^+ = \dot{\underline{\sigma}} - \underline{L} \cdot \underline{\sigma} - \underline{\sigma} \cdot \underline{L}^T, \quad (4.24)$$

while the Jaumann or co-rotational stress-rate is

$$\dot{\underline{\sigma}}^{\nabla} = \dot{\underline{\sigma}} + \underline{\sigma} \cdot \underline{W} - \underline{W} \cdot \underline{\sigma}. \quad (4.25)$$

The Truesdell stress rate is expressed as

$$\dot{\underline{\sigma}}^* = \dot{\underline{\sigma}} - \underline{L} \cdot \underline{\sigma} - \underline{\sigma} \cdot \underline{L}^T + \underline{\sigma}(\underline{L} : \underline{1}). \quad (4.26)$$

A family of objective stress-rates, when evaluated with the current state as reference (i.e., $\dot{\underline{E}}$ momentarily equal to \underline{D}), has been proposed by Hill [24] such that

$$\dot{\underline{\sigma}}^{\Delta} = \frac{D\underline{\sigma}}{Dt} - m(\underline{\sigma} \cdot \underline{D} + \underline{D} \cdot \underline{\sigma}), \quad (4.27)$$

where

$$\frac{D\underline{\sigma}}{Dt} \equiv \dot{\underline{\sigma}} + \underline{\sigma} \cdot \underline{W} - \underline{W} \cdot \underline{\sigma},$$

is the Jaumann-Zaremba, or material co-rotational rate of Kirchhoff

stress $\underline{\tau}$ and m is any real scalar.

4.3.3 Principle of Material Frame Indifference

Constitutive equations must be invariant under changes of frame of reference. That is two observers in different coordinate system observe the same stress in a given body, even in relative motion with respect to each other. The principle of material frame-indifference is also called the principle of objectivity.

Consider a motion of the body B in the starred frame which differs from the motion of the same body in the unstarred frame by a superimposed rigid body rotation and translation at time t , as shown in Figure 4.2. Thus

$$\bar{\mathbf{p}}^* = \bar{\mathbf{c}}(t) + \underline{\mathbf{Q}}(t) \cdot \bar{\mathbf{p}} \quad (4.28)$$

where $\bar{\mathbf{p}}^*$ and $\bar{\mathbf{p}}$ are position vectors with respect to two different frames. $\bar{\mathbf{c}}(t)$ is the relative position vector connecting the origins of the two frames, and $\underline{\mathbf{Q}}(t)$ is an orthogonal tensor rotating frame (*) into the orientation of the unstarred frame. $\underline{\mathbf{Q}}(t)$ satisfies the conditions

$$\underline{\mathbf{Q}}^T = \underline{\mathbf{Q}}^{-1}, \quad \underline{\mathbf{Q}} \cdot \underline{\mathbf{Q}}^T = \underline{\mathbf{1}} \quad \text{and} \quad \det \underline{\mathbf{Q}} = 1.$$

Assuming that the two frames had the same reference configuration at time t_0 such that $d\bar{\mathbf{X}}^* = d\bar{\mathbf{X}}$, the transformation formula for the deformation gradient $\underline{\mathbf{F}}$ under a change of frame at time t has the form

$$\underline{\mathbf{F}}^* = \underline{\mathbf{Q}} \cdot \underline{\mathbf{F}}, \quad (4.29)$$

and owing to the uniqueness of polar decomposition of equation (4.4) it follows that

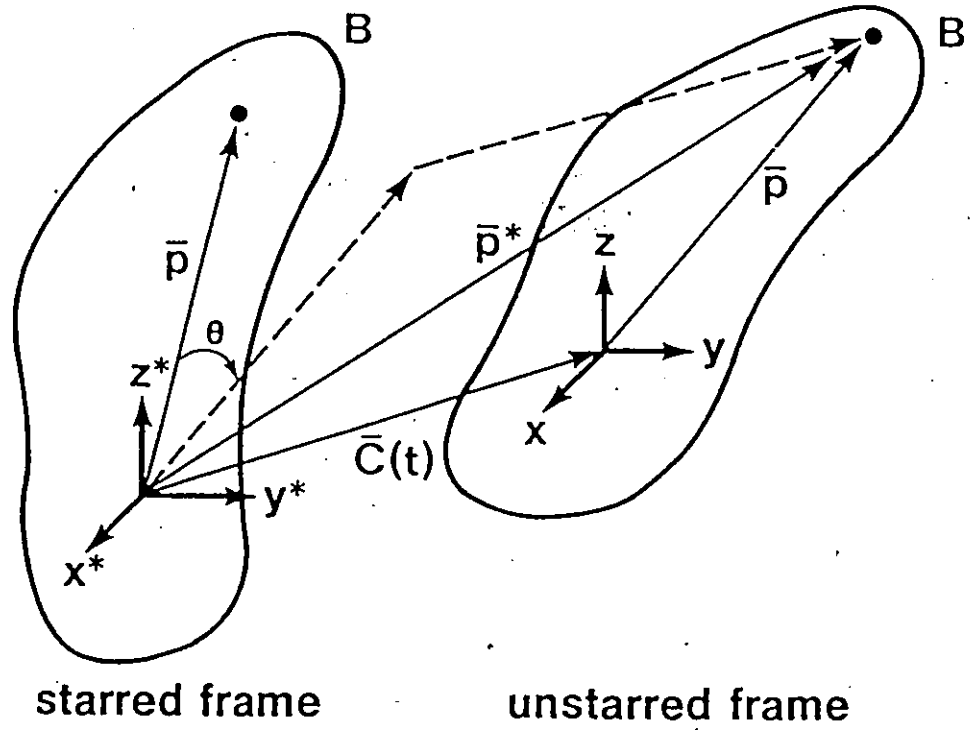


Figure 4.2: Schematic illustration of two reference frames.

$$\underline{R}^* = \underline{Q} \cdot \underline{R} \quad (4.30)$$

and

$$\underline{U}^* = \underline{U}. \quad (4.31)$$

In general a second order tensor $\underline{\xi}$ is frame indifferent if it satisfies the transformation law

$$\underline{\xi}^* = \underline{Q} \cdot \underline{\xi} \cdot \underline{Q}^T. \quad (4.32)$$

4.4 Method Of Analysis

4.4.1 Spins of the Strain Ellipsoids

Hill [25,26] has considered the rotation of the Lagrangian and Eulerian strain ellipsoids owing to an infinitesimal deformation step superimposed on the existing stretches, denoted by $\lambda_1, \lambda_2, \lambda_3$. In order to be able to make a distinction between the two ellipsoids the prior process must have been one of homogeneous deformation as opposed to pure homogeneous deformation, i.e. pure stretch. The axes of the Lagrangian ellipsoid are defined as being the ground state directions of the embedded orthogonal triad which are the current axes of the Eulerian ellipsoid. An infinitesimal deformation is then superimposed on the current Eulerian ellipsoid and the ensuing rotation calculated i.e. the change in orientation between the axes of the new and current ellipsoid. It is to be noted that the orthogonal triad which forms the axes of the new ellipsoid, was not an orthogonal set immediately before the increment.

As an illustration for rotation about the 1-axis Hill, op. cit., superimposes a symmetric deformation gradient, say $d\underline{\eta}$, where

$$d\eta = \begin{bmatrix} 1 & dn_{23} \\ dn_{32} & 1 \end{bmatrix} \quad (4.33)$$

and all the components are referred to the 2 and 3 axes of the ellipsoid. The rotation is calculated to first order as

$$\delta\phi_{1E} = \frac{\lambda_2^2 + \lambda_3^2}{\lambda_2^2 - \lambda_3^2} dn_{23} \quad (4.34)$$

for $\lambda_2 \neq \lambda_3$. The rate of rotation is

$$\dot{\phi}_{1E} = \frac{\lambda_2^2 + \lambda_3^2}{\lambda_2^2 - \lambda_3^2} \dot{\epsilon}_{23} \quad (4.35)$$

where $\epsilon_{23} = \epsilon_{32}$ are components of the Eulerian rate of deformation tensor, D . When the incremental deformation is not pure stretch then (4.35) must be augmented by the rigid body rotation $1/2 (\epsilon_{32} - \epsilon_{23})$.

Similarly the rotation of the Lagrangian ellipsoid about its own axes, due to the superposition of $d\eta$, is

$$\delta\phi_{1L} = \frac{(2\lambda_2 \lambda_3)}{\lambda_2^2 - \lambda_3^2} dn_{23} \quad \text{or} \quad \dot{\phi}_{1L} = \frac{(2\lambda_2 \lambda_3)}{\lambda_2^2 - \lambda_3^2} \dot{\epsilon}_{23} \quad (4.36)$$

with similar expressions for the rate of rotation about the 2 and 3 axes.

(a) Lagrangian Strain Ellipsoid

The deformation just described is that of a small strain superimposed on a large prior deformation. If the total deformation is characterized by E , where

$$\underline{F} = d\underline{\eta} \cdot \underline{\lambda} = \underline{R} \underline{U} = \underline{V} \cdot \underline{R}, \quad (4.37)$$

then the rotations given in (4.34) and (4.36) can be calculated precisely. As an illustration consider evaluating the rotation about the 1-axis of the chosen reference frame. From (4.37)

$$\underline{F} = \begin{bmatrix} F_{22} & F_{23} \\ F_{32} & F_{33} \end{bmatrix} = \begin{bmatrix} 1 & \eta_{23} \\ \eta_{32} & 1 \end{bmatrix} \begin{bmatrix} \lambda_2 & 0 \\ 0 & \lambda_3 \end{bmatrix} = \begin{bmatrix} \lambda_2 & \eta_{23}\lambda_3 \\ \eta_{32}\lambda_2 & \lambda_3 \end{bmatrix} \quad (4.38)$$

Define the components of the rotation tensor \underline{R} , in the 2-3 plane as

$$\underline{R} = \begin{bmatrix} \cos \theta & -\sin \theta \\ \sin \theta & \cos \theta \end{bmatrix} \quad (4.39)$$

and it is then easy to show that

$$\tan \theta_1 = \frac{F_{32} - F_{23}}{F_{22} + F_{33}} = \frac{\eta_{23} (\lambda_2 - \lambda_3)}{(\lambda_2 + \lambda_3)} \quad (4.40)$$

Thus the rigid body rotation is small and

$$\tan \theta_1 = \theta_1 = \frac{\eta_{23} (\lambda_2 - \lambda_3)}{(\lambda_2 + \lambda_3)} \quad (4.41)$$

The orientation of the principal axes of the Lagrangian strain ellipse, in the 2-3 plane, is calculated from the components of the stretch tensor \underline{U} where

$$\tan 2\phi_{1L} = \frac{2U_{23}}{U_{22} - U_{33}} = \frac{2(F_{33}F_{32} + F_{22}F_{23})}{(F_{22}^2 - F_{33}^2) + (F_{32}^2 - F_{23}^2)} \quad (4.42)$$

This is also a very small angle, hence

$$\phi_{1L} = \frac{F_{33}F_{32} + F_{22}F_{23}}{(F_{22}^2 - F_{33}^2) + (F_{32}^2 - F_{23}^2)} \quad (4.43)$$

which is identical to (4.36) if the second order quantity $(F_{32}^2 - F_{23}^2)$ is ignored. See also Appendix F for more details.

(b) Eulerian Strain Ellipsoid

The rotation of the Eulerian ellipse, to use Hill's terminology, in the 2-3 plane is sum of equations (4.41) and (4.43)

$$\phi_{1E} = \phi_{1L} + \theta_1, \quad (4.44)$$

which to first order can be shown to be identical to (4.34).

Alternatively the rotation can be found from

$$\tan 2\phi_{1E} = \frac{2V_{23}}{V_{22} - V_{33}} = \frac{2(F_{22}F_{32} + F_{33}F_{23})}{(F_{22}^2 - F_{33}^2) - (F_{32}^2 - F_{23}^2)}, \quad (4.45)$$

where for small angles

$$\phi_{1E} = \frac{F_{22}F_{32} + F_{33}F_{23}}{(F_{22}^2 - F_{33}^2) - (F_{32}^2 - F_{23}^2)}. \quad (4.46)$$

It will be apparent that equations (4.42) and (4.45) define the orientation of the eigenvectors of $\underline{F}^T \cdot \underline{F}$ and $\underline{F} \cdot \underline{F}^T$ respectively. For a detailed derivation of the above equations the readers are referred to Appendix F.

4.4.2 Choice of Strain and Strain Rate Measures

A variety of deformation or strain measures can be generated from the tensors \underline{U} and \underline{V} and these are usually classified as being Lagrangian and Eulerian respectively, in description. Hill [25,26] has proposed a general class of strain measures where the principal values are defined

as

$$\epsilon_1 = f(\lambda_1), \text{ with } f(1) = 0 \text{ and } f'(1) = 1,$$

and $f(\lambda_1)$ is any smooth monotonic function. In particular when

$$f(\lambda_1) = (\lambda_1^{2m} - 1)/2m$$

the most commonly used strain measures are revealed. Hill, op. cit., claims that logarithmic strain measures (when $m=0$) can be advantageous in certain constitutive inequalities, but points out that a number of researchers have considered that such measures can give rise to analytical difficulties. Stören and Rice [39] adopted the logarithmic measure in their formulation of deformation-theory models, but concluded that no simple relationship existed between the time rate i.e. $(\ln U)$ and the rate of deformation tensor D . However, Hill, op cit, had established a relationship between $(\ln \lambda)$ and a function of D .

We develop below a general relationship between the logarithmic strain rate and the rate of deformation tensor. The analysis has been performed in an alternative manner by Gurtin and Spear [7].

From (4.4), (4.5) and (4.10a) it follows that

$$\begin{aligned} \underline{L} &= (\dot{\underline{R}} \cdot \underline{U} + \underline{R} \cdot \dot{\underline{U}}) \cdot (\underline{U}^{-1} \cdot \underline{R}^{-1}) \\ &= \dot{\underline{R}} \cdot \underline{R}^T + \underline{R} \cdot (\dot{\underline{U}} \cdot \underline{U}^{-1}) \cdot \underline{R}^T, \end{aligned} \quad (4.47)$$

likewise

$$\underline{L}^T = \underline{R} \cdot \dot{\underline{R}}^T + \underline{R} \cdot (\underline{U}^{-1} \cdot \dot{\underline{U}}) \cdot \underline{R}^T. \quad (4.48)$$

Now

$$\begin{aligned} \underline{D} &= 1/2 (\underline{L} + \underline{L}^T) \\ &= 1/2 [\underline{R} \cdot (\dot{\underline{U}} \cdot \underline{U}^{-1}) + \underline{U}^{-1} \cdot \dot{\underline{U}}] \cdot \underline{R}^T, \end{aligned} \quad (4.49)$$

and

$$\begin{aligned} \underline{W} &= 1/2 (\underline{L} - \underline{L}^T) \\ &= 1/2 [\underline{R} \cdot (\underline{\dot{U}} \cdot \underline{U}^{-1} - \underline{U}^{-1} \cdot \underline{\dot{U}}) \cdot \underline{R}^T] + \underline{\dot{R}} \cdot \underline{R}^T. \end{aligned} \quad (4.50)$$

Similar expressions to (4.47) - (4.50) can be derived involving the left stretch tensor \underline{v} . The quantity $\underline{\dot{R}} \cdot \underline{R}^T$ may be interpreted as the angular velocity of the material, see the discussion by Dienes [19]. It is clear from (4.50) that, in general, the angular velocity is distinct from the spin tensor \underline{W} .

From (4.8) the time derivative of $\ln \underline{U}$ is

$$(\ln \underline{U})^\cdot = \underline{\dot{P}} \cdot \underline{P}^T \cdot (\ln \underline{U}) - (\ln \underline{U}) \cdot \underline{\dot{P}} \cdot \underline{P}^T + \underline{P} \cdot \underline{\dot{\lambda}} \cdot \underline{\lambda}^{-1} \cdot \underline{P}^T,$$

Hence

$$\underline{P} \cdot \underline{\dot{\lambda}} \cdot \underline{\lambda}^{-1} \cdot \underline{P}^T = (\ln \underline{U})^\cdot + (\ln \underline{U}) \cdot \underline{\dot{P}} \cdot \underline{P}^T - \underline{\dot{P}} \cdot \underline{P}^T \cdot (\ln \underline{U}) \quad (4.51)$$

The entity $\underline{\dot{P}} \cdot \underline{P}^T$ is another skew symmetric tensor representing the rate of rotation of the principal axes of \underline{U} , i.e. the spin of the Lagrangian ellipsoid. The right hand side of (4.51) can be regarded as a co-rotational rate of $(\ln \underline{U})$, say $(\ln \underline{U})^\circ$, relative to the principal axes of \underline{U} . Such that

$$(\ln \underline{U})^\circ = (\ln \underline{U})^\cdot + (\ln \underline{U}) \cdot \underline{\dot{P}} \cdot \underline{P}^T - \underline{\dot{P}} \cdot \underline{P}^T \cdot (\ln \underline{U})$$

then equation (4.51) becomes

$$\underline{P} \cdot \underline{\dot{\lambda}} \cdot \underline{\lambda}^{-1} \cdot \underline{P}^T = (\ln \underline{U})^\circ. \quad (4.52)$$

It can be shown that

$$\underline{\dot{U}} \cdot \underline{U}^{-1} = \underline{\dot{P}} \cdot \underline{P}^T + (\ln \underline{U})^\circ - \underline{U} \cdot \underline{\dot{P}} \cdot \underline{P}^T \cdot \underline{U}^{-1} \quad (4.53)$$

and

$$\underline{U}^{-1} \cdot \underline{\dot{U}} = \underline{P} \cdot \underline{\dot{P}}^T + (\ln \underline{U})^\circ + \underline{U}^{-1} \cdot \underline{\dot{P}} \cdot \underline{P}^T \cdot \underline{U}, \quad (4.54)$$

where

$$\underline{\underline{P}} \cdot \underline{\underline{\dot{P}}}^T = - \underline{\underline{\dot{P}}} \cdot \underline{\underline{P}}^T.$$

It follows from (4.49) that

$$\begin{aligned} \underline{\underline{D}} &= \underline{\underline{R}} \cdot (\ln \underline{\underline{U}})^{\circ} \cdot \underline{\underline{R}}^T - 1/2 (\underline{\underline{F}} \cdot \underline{\underline{\dot{P}}} \cdot \underline{\underline{P}}^T \cdot \underline{\underline{F}}^{-1} - \underline{\underline{F}}^{-T} \cdot \underline{\underline{\dot{P}}} \cdot \underline{\underline{P}}^T \cdot \underline{\underline{F}}^T) \\ &= \underline{\underline{R}} \cdot (\ln \underline{\underline{U}})^{\circ} \cdot \underline{\underline{R}}^T - \text{sym} (\underline{\underline{F}} \cdot \underline{\underline{\dot{P}}} \cdot \underline{\underline{P}}^T \cdot \underline{\underline{F}}^{-1}). \end{aligned} \quad (4.55)$$

Similarly, it can be shown that

$$\underline{\underline{D}} = (\ln \underline{\underline{V}})^{\circ} - \text{sym}(\underline{\underline{F}} \cdot \underline{\underline{\dot{P}}} \cdot \underline{\underline{P}}^T \cdot \underline{\underline{F}}^{-1}) \quad (4.56)$$

while

$$\underline{\underline{W}} = \underline{\underline{R}} \cdot \underline{\underline{R}}^T + \underline{\underline{R}} \cdot \underline{\underline{\dot{P}}} \cdot \underline{\underline{P}}^T \cdot \underline{\underline{R}}^T - \text{unsym} (\underline{\underline{F}} \cdot \underline{\underline{\dot{P}}} \cdot \underline{\underline{P}}^T \cdot \underline{\underline{F}}^{-1}). \quad (4.57)$$

It can easily be seen from (4.47) and (4.53) the velocity gradient tensor becomes

$$\begin{aligned} \underline{\underline{L}} &= \underline{\underline{\dot{R}}} \cdot \underline{\underline{R}}^T + \underline{\underline{R}} \cdot \underline{\underline{\dot{P}}} \cdot \underline{\underline{P}}^T \cdot \underline{\underline{R}}^T + \underline{\underline{R}} \cdot (\ln \underline{\underline{U}})^{\circ} \cdot \underline{\underline{R}}^T \\ &\quad - \underline{\underline{F}} \cdot \underline{\underline{\dot{P}}} \cdot \underline{\underline{P}}^T \cdot \underline{\underline{F}}^{-1}. \end{aligned} \quad (4.58)$$

Hill [26] had established a relationship between the logarithmic strain tensor $\ln \underline{\underline{U}}$ and the rate of deformation gradient $\underline{\underline{D}}$. Note that Hill's result is derivable from the present theory and this is demonstrated here. Equation (4.8) is differentiated with respect to time to yield

$$\dot{(\ln \underline{\underline{U}})}^{\circ} = \underline{\underline{\dot{P}}} \cdot \underline{\underline{P}}^T \cdot (\ln \underline{\underline{U}}) - (\ln \underline{\underline{U}}) \cdot \underline{\underline{\dot{P}}} \cdot \underline{\underline{P}}^T + \underline{\underline{P}} \cdot \underline{\underline{\dot{\lambda}}} \cdot \underline{\underline{\lambda}}^{-1} \cdot \underline{\underline{P}}^T. \quad (4.59)$$

In particular Hill, op cit, treats the rotation of the Lagrangian ellipsoid about its own axes for the special case where they coincide with the frame of reference. Consequently

$$\underline{\underline{P}} = \underline{\underline{1}},$$

and

$$\ln \underline{\underline{U}} = \ln \underline{\underline{\lambda}}.$$

In view of these conditions, Equation (4.59) reduces to

$$(\dot{\ln} \underline{U})^* = \dot{\underline{P}} \cdot \underline{P}^T \cdot (\dot{\ln} \underline{\lambda}) - (\dot{\ln} \underline{\lambda}) - \dot{\underline{P}} \cdot \underline{P}^T + \dot{\underline{\lambda}} \cdot \underline{\lambda}^{-1} \quad (4.60)$$

However, the spin of the Lagrangian triad can be evaluated from $\dot{\underline{P}} \cdot \underline{P}^T$, and as an illustration for the spin about the 1-axis

$$\dot{\underline{P}} \cdot \underline{P}^T = \dot{\phi}_{1L} \begin{bmatrix} 0 & -1 \\ 1 & 0 \end{bmatrix} \quad (4.61)$$

where $\dot{\phi}_{1L}$ is defined in (4.36). Upon substituting (4.61) into (4.60) we have the components in the 2-3 plane,

$$(\dot{\ln} \underline{U})^* = \begin{bmatrix} \dot{\lambda}_2/\lambda_2 & \dot{\phi}_L \ln(\lambda_2/\lambda_3) \\ \dot{\phi}_L \ln(\lambda_2/\lambda_3) & \dot{\lambda}_3/\lambda_3 \end{bmatrix} \quad (4.62a)$$

or

$$(\dot{\ln} \underline{\lambda})^* = \begin{bmatrix} (\dot{\ln} \lambda_2)^* & \dot{\phi}_L \ln(\lambda_2/\lambda_3) \\ \dot{\phi}_L \ln(\lambda_2/\lambda_3) & (\dot{\ln} \lambda_3)^* \end{bmatrix} \quad (4.62b)$$

and $(\dot{\ln} \lambda_2)^* = \dot{\lambda}_2/\lambda_2 = \epsilon_{22}$, which is a component of the rate of deformation tensor \underline{D} . The right hand side of (4.62b) gives Hill's result [26]. A detailed proof of equations (4.55) and (4.62) are provided in Appendix F.

4.4.3 Choice of Stress Rate Measures

In finite deformation processes material rotation becomes very significant. As a result of material rotation the stress components will vary, and constitutive equations which involve stress rate must be formulated to compensate for the rotation. A number of stress rates are examined and employed in a constitutive equation describing a hypo-elastic solid. The effect of stress rate on the evaluation of stress in

the deforming solid is demonstrated for the case when the body undergoes simple shear deformation. Dienes [35] has proposed an expression for the measure of stress rate in term of material rotation where the objective stress rate is defined as

$$\hat{\underline{\sigma}} = \underline{\dot{\sigma}} + \underline{\sigma} \cdot \underline{\Omega} - \underline{\Omega} \cdot \underline{\sigma}$$

and

$$\underline{\Omega} = \underline{\dot{R}} \cdot \underline{R}^T$$

For the sake of completeness the above result is derived from a more general standpoint. In addition alternative stress rates are proposed which are a function of the spin of the Lagrangian or Eulerian ellipsoid.

In order to choose a symmetric stress tensor which is conjugate to $\underline{\dot{E}}$ (momentarily equal to \underline{D} in the reference state), it is convenient to consider equation (4.15), i.e. the rate of work done per unit current volume of the material. By employing the velocity gradient $\underline{L} = \underline{D} + \underline{W}$ such that the rate of work equation reduces to

$$\dot{\underline{w}} = \underline{\tau} : \underline{D} \quad (4.63)$$

Rewriting equation (4.55) as

$$\underline{D} = \underline{R} \cdot \underline{\psi} \cdot \underline{R}^T \quad (4.64)$$

where the tensor $\underline{\psi}$ is given in terms of the right stretch tensor \underline{U} as

$$\underline{\psi} = (\ln \underline{U})^0 - \text{sym} (\underline{U} \cdot \underline{\dot{P}} \cdot \underline{P}^T \cdot \underline{U}^{-1}) \quad (4.65)$$

Substituting equation (4.64) into (4.63), the rate of work done becomes

$$\underline{\tau} : \underline{D} = \underline{\tau} : (\underline{R} \cdot \underline{\psi} \cdot \underline{R}^T) \quad (4.66)$$

From the definition of the scalar product of two second order tensors, it can be shown that

$$\underline{A} : \underline{B} = (\underline{A}^T \cdot \underline{B}) : \underline{1} = (\underline{A} \cdot \underline{B}^T) : \underline{1}$$

where \underline{A} , \underline{B} are the general second order tensors and $\underline{1}$ is the identity tensor. Then applying the tensor transformation to (4.66) yields

$$\underline{I}_R : \underline{\Psi} = (\underline{R}^T \cdot \underline{I} \cdot \underline{R}) : \underline{\Psi}$$

and we obtain a conjugate stress tensor \underline{I}_R of the form

$$\underline{I}_R = \underline{R}^T \cdot \underline{I} \cdot \underline{R} \quad (4.67)$$

Taking the time derivative of (4.67), and using the relation $\dot{\underline{R}} \cdot \underline{R}^T = -\underline{R} \cdot \dot{\underline{R}}^T$, it can be found that

$$\begin{aligned} \dot{\underline{I}}_R &= \dot{\underline{R}}^T \cdot (\underline{I} + \underline{I} \cdot (\dot{\underline{R}} \cdot \underline{R}^T) - (\dot{\underline{R}} \cdot \underline{R}^T) \cdot \underline{I}) \cdot \underline{R} \\ &= \underline{R}^T \cdot (\dot{\underline{I}} + \underline{I} \cdot \underline{\Omega} - \underline{\Omega} \cdot \underline{I}) \cdot \underline{R}, \end{aligned} \quad (4.68)$$

where $\underline{\Omega} = \dot{\underline{R}} \cdot \underline{R}^T$ which is a skew symmetric tensor representing the rate of rotation of the material. The quantity in the bracket of (4.68) can be regarded as a co-rotational stress rate such that it is defined as

$$\underline{\overset{\vee}{I}} = \dot{\underline{I}} + \underline{I} \cdot \underline{\Omega} - \underline{\Omega} \cdot \underline{I} \quad (4.69)$$

The time derivative of the Kirchhoff stress tensor is expressed as (see equation (4.21))

$$\begin{aligned} \dot{\underline{I}} &= J\dot{\underline{\sigma}} + J\dot{\underline{\sigma}} \\ &= J\dot{\underline{\sigma}}(\underline{L} : \underline{1}) + J\dot{\underline{\sigma}}. \end{aligned} \quad (4.69a)$$

Upon substituting the above equation into (4.69) and using $\underline{L} = \underline{D} + \underline{W}$, the co-rotational stress rate becomes

$$\underline{\overset{\vee}{I}} = J(\dot{\underline{\sigma}} + \underline{\sigma} \cdot \underline{\Omega} - \underline{\Omega} \cdot \underline{\sigma} + \underline{\sigma}(\underline{D} : \underline{1})). \quad (4.70)$$

The modified Cauchy or co-rotational stress rate may then be defined as

$$\underline{\overset{\vee}{\sigma}}_R = \dot{\underline{\sigma}} + \underline{\sigma} \cdot \underline{\Omega} - \underline{\Omega} \cdot \underline{\sigma} + \underline{\sigma}(\underline{D} : \underline{1}). \quad (4.71)$$

For incompressible material the above expression reduces to that of the result of Dienes, i.e.

$$\underline{\hat{\sigma}} = \underline{\dot{\sigma}} + \underline{\sigma} \cdot \underline{\Omega} - \underline{\Omega} \cdot \underline{\sigma}. \quad (4.72)$$

Analogous to the development of (4.71), an alternative measure of stress rate is proposed, it has the form

$$\underline{\bar{\sigma}} = \underline{\dot{\sigma}} + \underline{\sigma} \cdot \underline{\phi} - \underline{\phi} \cdot \underline{\sigma} + \underline{\sigma} (\underline{D} : \underline{1}), \quad (4.73)$$

where the skew symmetric second order tensor $\underline{\phi}$ may be expressed in terms of the spin of the Lagrangian strain ellipsoid as

$$\underline{\phi} = \underline{\dot{P}} \cdot \underline{P}^T = \underline{\dot{\phi}}_L \begin{pmatrix} 0 & 1 \\ -1 & 0 \end{pmatrix} \quad (4.74)$$

Again for an isochoric deformation (4.73) reduces to

$$\underline{\bar{\sigma}} = \underline{\dot{\sigma}} + \underline{\sigma} \cdot \underline{\phi} - \underline{\phi} \cdot \underline{\sigma}. \quad (4.75)$$

The tensor $\underline{\phi}$ can also be expressed in terms of the rate of rotation of the Eulerian triad and it is evaluated from

$$\underline{\phi} = \underline{\dot{\phi}}_E \begin{pmatrix} 0 & 1 \\ -1 & 0 \end{pmatrix}, \quad (4.76)$$

where $\underline{\dot{\phi}}_L$ and $\underline{\dot{\phi}}_E$ are defined in equations (4.36) and (4.35) respectively.

Anticlockwise rotation is regarded as positive here.

The stress rate $\underline{\bar{\sigma}}$ defined in (4.75) takes into account of the rate of rotation of the principal axes with respect to the material element due to finite deformation. This rate equation in fact contains two different stress rate measures depending on the choice of the rate of rotation tensor $\underline{\phi}$. It will be shown later that such a stress rate seems to be of value when applied to finite deformation problems. Details of the above development can be found in Appendix F.

4.4.4 Frame Indifference Quantities

It is demonstrated in this section that the conjugate variables which have defined previously are frame indifferent, for instance the tensors $\underline{\underline{g}}$ and $\underline{\underline{g}}^*$.

Consider a motion of the continuum which differs from the motion only by a superimposed rigid-body rotation at time t , such that

$$d\bar{x}^* = \underline{\underline{Q}} \cdot d\bar{x}, \quad (4.77)$$

where the orthogonal tensor $\underline{\underline{Q}}$ which rotates one frame to the other is a function of t and satisfies the conditions

$$\underline{\underline{Q}} \cdot \underline{\underline{Q}}^T = \underline{\underline{1}}, \text{ and } \det \underline{\underline{Q}} = 1. \quad (4.78)$$

It follows from the above that the rate of rotation of the starred frame with respect to the frame of reference is defined as

$$\underline{\underline{\omega}} = \dot{\underline{\underline{Q}}} \cdot \underline{\underline{Q}}^T \quad (4.79)$$

and in view of (4.78)

$$\underline{\underline{\omega}} + \underline{\underline{\omega}}^T = \underline{\underline{0}}. \quad (4.80)$$

Upon utilizing equations (4.77) to (4.80), the corresponding tensor quantities in the rotated (*) frame are obtained as follows:

Frame Indifferent Quantities

$$\underline{\underline{V}}^* = \underline{\underline{Q}} \cdot \underline{\underline{V}} \cdot \underline{\underline{Q}}^T$$

$$\underline{\underline{D}}^* = \underline{\underline{Q}} \cdot \underline{\underline{D}} \cdot \underline{\underline{Q}}^T$$

$$\underline{\underline{W}}^* - \underline{\underline{\Omega}}^* = \underline{\underline{Q}} \cdot (\underline{\underline{W}} - \underline{\underline{\Omega}}) \cdot \underline{\underline{Q}}^T$$

Frame Dependent Quantities

$$\underline{\underline{L}}^* = \underline{\underline{Q}} \cdot \underline{\underline{L}} \cdot \underline{\underline{Q}}^T + \underline{\underline{\omega}} \otimes \underline{\underline{E}}$$

$$\underline{\underline{W}}^* = \underline{\underline{Q}} \cdot \underline{\underline{W}} \cdot \underline{\underline{Q}}^T + \underline{\underline{\omega}} \otimes \underline{\underline{E}}$$

$$\underline{\underline{\Omega}} = \underline{\underline{Q}} \cdot \underline{\underline{\Omega}} \cdot \underline{\underline{Q}}^T + \underline{\underline{\omega}} \otimes \underline{\underline{E}}$$

The derivations of the above quantities have not been given in

detail but can be found in many standard texts on continuum mechanics [2-4,37]. For completeness tensor variables which are not frame invariant quantities are also outlined below:

$$\begin{aligned}\underline{U}^* &= \underline{U} ; \ln \underline{U}^* = \ln \underline{U} ; (\ln \underline{U}^*)^\circ = (\ln \underline{U})^\circ \\ (\ln \underline{U}^*)^0 &= (\ln \underline{U})^0 ; \underline{\lambda}^* = \underline{\lambda} \text{ and } \underline{P}^* = \underline{P}\end{aligned}$$

In view of the above tensor variables in the rotated (*) frame it can be shown from equation (4.65) that

$$\underline{\psi}^* = \underline{\psi} \quad (4.81)$$

which is obvious as $\underline{D} = \underline{R} \cdot \underline{\psi} \cdot \underline{R}^T$ such that

$$\begin{aligned}\underline{D}^* &= \underline{R}^* \cdot \underline{\psi}^* \cdot \underline{R}^{*T} \\ &= \underline{Q} \cdot (\underline{R} \cdot \underline{\psi} \cdot \underline{R}^T) \cdot \underline{Q}^T \\ &= \underline{Q} \cdot \underline{D} \cdot \underline{Q}^T\end{aligned} \quad (4.82)$$

is frame invariant.

Some particular constitutive equations include the material time derivative $\dot{\underline{g}}$ of the stress tensor \underline{g} among the constitutive variables. Such equations do not satisfy the principle of material frame-indifference for arbitrary motion, the difficulty lies in the fact that the material derivative $\dot{\underline{g}}$ does not transform according to equation (4.32) under an orthogonal change of the spatial reference frame even though \underline{g} does, i.e. $\dot{\underline{g}}$ is not frame-indifferent, though \underline{g} is. We shall demonstrate that some of the co-rotational stress rates that have been proposed previously are frame invariant. From equation (4.32) \underline{g}^* can be written as

$$\underline{g}^* = \underline{Q} \cdot \underline{g} \cdot \underline{Q}^T. \quad (4.83)$$

When (4.83) is differentiated with respect to time it follows that

$$\dot{\underline{\sigma}}^* = \underline{Q} \cdot \dot{\underline{\sigma}} \cdot \underline{Q}^T + \dot{\underline{Q}} \cdot \underline{\sigma} \cdot \underline{Q}^T + \underline{Q} \cdot \underline{\sigma} \cdot \dot{\underline{Q}}^T, \quad (4.84)$$

since the rate of rotation of the field in the rotated frame is expressed as

$$\dot{\underline{\Omega}}^* = \underline{Q} \cdot \dot{\underline{\Omega}} \cdot \underline{Q}^T + \underline{\omega} \quad (4.85)$$

where $\underline{\Omega} = \underline{\dot{R}} \cdot \underline{R}^T$ and $\underline{\omega} = \dot{\underline{Q}} \cdot \underline{Q}^T$ are skew symmetric tensors. Rearranging equation (4.85) and using $\underline{Q} \cdot \underline{Q}^T = \underline{1}$, gives

$$\dot{\underline{Q}} = \underline{\Omega}^* \cdot \underline{Q} - \underline{Q} \cdot \underline{\Omega} \quad (4.86)$$

and

$$\dot{\underline{Q}}^T = \underline{\Omega} \cdot \underline{Q}^T - \underline{Q}^T \cdot \underline{\Omega}^*.$$

Substituting (4.86) into the equation (4.84), yields

$$(\dot{\underline{\sigma}}^* + \underline{\sigma}^* \cdot \underline{\Omega}^* - \underline{\Omega}^* \cdot \underline{\sigma}^*) = \underline{Q} \cdot (\dot{\underline{\sigma}} + \underline{\sigma} \cdot \underline{\Omega} - \underline{\Omega} \cdot \underline{\sigma}) \cdot \underline{Q}^T$$

or

$$\dot{\underline{\sigma}}^* = \underline{Q} \cdot \dot{\underline{\sigma}} \cdot \underline{Q}^T \quad (4.87)$$

This result permits a wide choice of Jaumann type derivatives all of which are objective. A similar proof can be applied to the stress rate $\dot{\underline{\sigma}}$, as defined in (4.75), by simply replacing $\underline{\Omega}$ with $\underline{\phi}$. In general $\underline{\phi}$, a skew symmetric tensor, is not frame-indifferent. Hence,

$$\dot{\underline{\phi}}^* = \underline{Q} \cdot \dot{\underline{\phi}} \cdot \underline{Q}^T + \underline{\omega}$$

$$\dot{\underline{Q}} = \underline{\phi}^* \cdot \underline{Q} - \underline{Q} \cdot \underline{\phi}$$

and

(4.88)

$$\dot{\underline{Q}}^T = \underline{\phi} \cdot \underline{Q}^T - \underline{Q}^T \cdot \underline{\phi}^*.$$

Upon utilizing equation (4.88), equation (4.84) becomes

$$(\dot{\underline{\sigma}}^* + \underline{\sigma}^* \cdot \underline{\phi}^* - \underline{\phi}^* \cdot \underline{\sigma}^*) = \underline{Q} \cdot (\dot{\underline{\sigma}} + \underline{\sigma} \cdot \underline{\phi} - \underline{\phi} \cdot \underline{\sigma}) \cdot \underline{Q}^T$$

or

$$\dot{\underline{\sigma}}^* = \underline{Q} \cdot \dot{\underline{\sigma}} \cdot \underline{Q}^T. \quad (4.89)$$

Any one of the stress rates that have been discussed previously may be used to formulate a proper constitutive equation whereby the rotational effect of the material has been taken into consideration. As such the components of the stress derived from the constitutive law are frame indifferent, i.e. the stresses of a deforming body observed by different viewers are the same. The utility of the expressions in a numerical scheme will be demonstrated in the next section. The aforementioned theory developed so far forms the fundamental important aspects of material rotations, stress rates and strain measures in finite homogeneous deformation processes.

4.5 Rotations and Stress Rates in Simple Shear

The explicit formulae for the various objective stress rates developed in section 4.4.3 are employed to ascertain the influence of the stress rate on the evolution of the stresses in a deforming body. The rate equations are applied to the flow of a hypoelastic material undergoing simple, rectilinear shear deformation.

The simple shear mode is illustrated in Figure 4.3, the deformation mode has wide-spread engineering applications because it is considered to represent the torsion of a thin walled tube. In Figure 4.3(c), the point C is displaced horizontally a distance S to C'. If the initial length of OC is taken as unity then $OC' = \sqrt{1+S^2}$ while OA does not alter in length. Let γ represent the change in the unit right angle and therefore

$$\tan \gamma = S \quad (4.90)$$

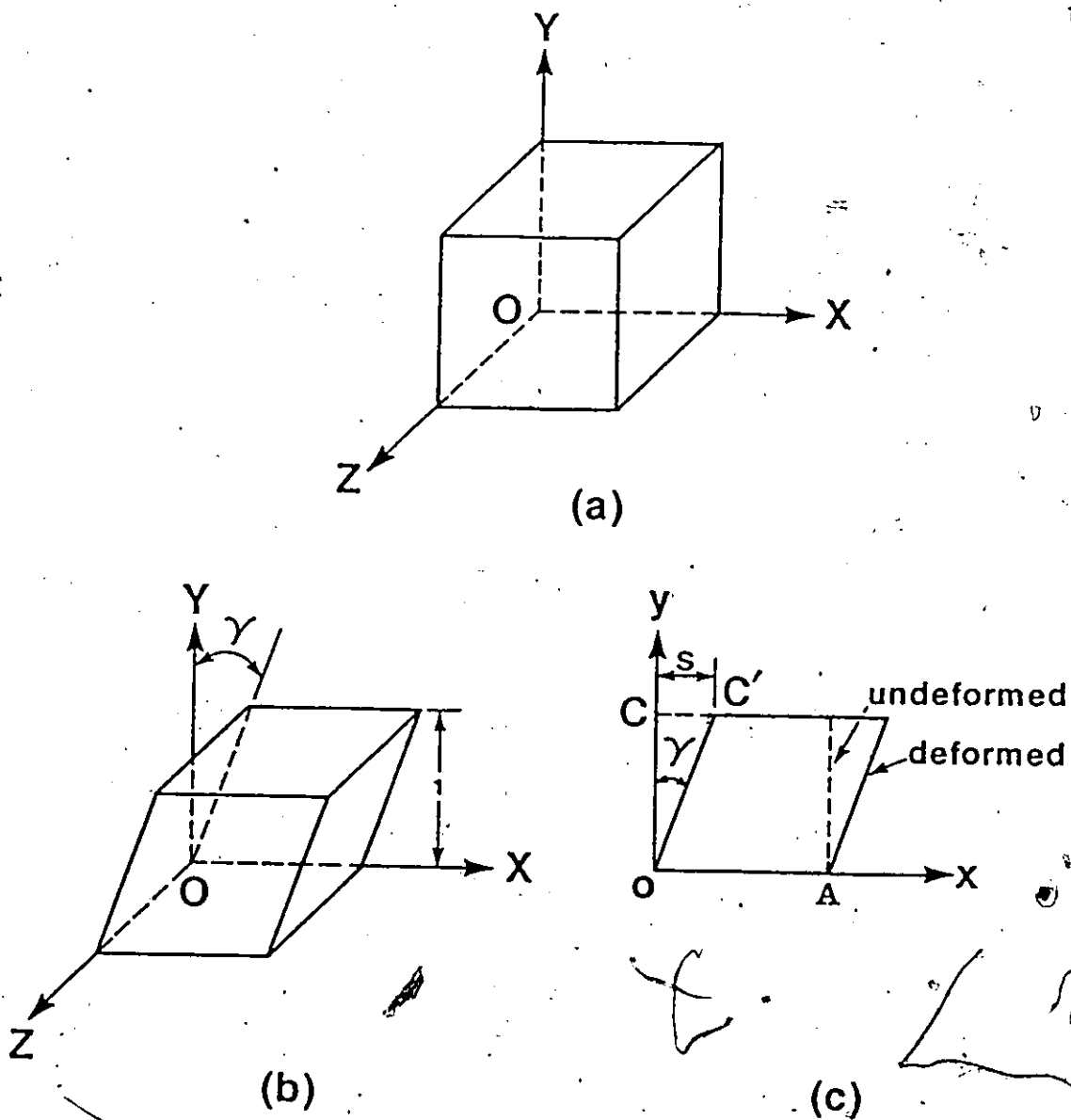


Figure 4.3: Finite simple shear deformation.

- (a) The undeformed unit cube.
- (b) The deformed element.
- (c) The deformed configuration of (b) in two-dimensional space.

The homogeneous deformation is represented by the kinematic relations

$$\begin{aligned} x &= X_0 + SY_0 \\ y &= Y_0 \\ z &= Z_0 \end{aligned} \quad (4.91)$$

For a shear displacement S the deformation gradient tensor is

$$\underline{F} = \begin{bmatrix} 1 & S & 0 \\ 0 & 1 & 0 \\ 0 & 0 & 1 \end{bmatrix} \quad (4.92)$$

The components of the rotation tensor \underline{R} are

$$\underline{R} = \begin{bmatrix} \cos\theta & \sin\theta & 0 \\ -\sin\theta & \cos\theta & 0 \\ 0 & 0 & 1 \end{bmatrix} \quad (4.93)$$

therefore,

$$\underline{\Omega} = \dot{\underline{R}} \cdot \underline{R}^T = \dot{\theta} \begin{bmatrix} 0 & 1 & 0 \\ -1 & 0 & 0 \\ 0 & 0 & 0 \end{bmatrix} \quad (4.94)$$

From equations (4.4), (4.92) and (4.93) it follows that the angle of rotation θ

$$\tan\theta = S/2 \quad (4.95)$$

while from (4.42) the orientation of the principal axes of the Lagrangian ellipsoid is obtained as (anticlockwise from x-axis)

$$\tan 2\phi_L = -2/S. \quad (4.96)$$

Likewise from (4.45) the orientation of the principal axes of the Eulerian ellipsoid is

$$\tan 2\phi_E = 2/S. \quad (4.97)$$

Differentiating (4.95) with respect to time, yields

$$\dot{\theta} \sec^2 \theta = \dot{S}/2 \quad (4.98)$$

$$(\ddot{\theta} + 2 \tan \theta \dot{\theta}^2) \sec^2 \theta = \ddot{S}/2 \quad (4.99)$$

For the simple shear process if the element deforms with constant speed such that $\ddot{S} = 0$ and therefore (4.99) becomes

$$\ddot{\theta} + 2 \tan \theta \dot{\theta}^2 = 0 \quad (4.100)$$

Similarly from (4.96)

$$S^2 \dot{\phi}_L = \dot{S} \cos^2 2\phi_L, \quad (4.101)$$

and with $\ddot{S} = 0$

$$2 \dot{\phi}_L \dot{S} + S^2 \ddot{\phi}_L = -2 \dot{S} \dot{\phi}_L \sin 4\phi_L, \quad (4.102)$$

where the quantity $\dot{\phi}_L$ is defined in (4.36), it is the spin of the Lagrangian ellipsoid.

The velocity gradient tensor can be obtained through (4.10a) such that

$$\underline{L} = \begin{pmatrix} 0 & \dot{S} & 0 \\ 0 & 0 & 0 \\ 0 & 0 & 0 \end{pmatrix} \quad (4.103)$$

The separation of the velocity gradient tensor into the symmetric and antisymmetric parts leads to the rate of deformation tensor

$$\underline{D} = \begin{pmatrix} 0 & \dot{S}/2 & 0 \\ \dot{S}/2 & 0 & 0 \\ 0 & 0 & 0 \end{pmatrix} \quad (4.104)$$

and the spin tensor

$$\underline{W} = \begin{pmatrix} 0 & \dot{S}/2 & 0 \\ -\dot{S}/2 & 0 & 0 \\ 0 & 0 & 0 \end{pmatrix} \quad (4.105)$$

In order to illustrate the main results of the stress calculations, we consider the simplest form of a hypo-elastic material of grade zero with the constitutive equation of the form

$$\underline{\overset{\circ}{\sigma}} = \lambda \text{ trace } (\underline{D}) \underline{1} + 2 \mu \underline{D}. \quad (4.106)$$

In the above equation λ and μ are Lamé's constants, $\underline{1}$ the identity tensor and $\underline{\overset{\circ}{\sigma}}$ an objective stress rate. The stress rates discussed previously are repeated here for convenience. The Jaumann stress rate is defined as

$$\underline{\overset{\nabla}{\sigma}} = \underline{\dot{\sigma}} + \underline{\sigma} \cdot \underline{W} - \underline{W} \cdot \underline{\sigma}, \quad (4.107)$$

while Dienes [35] proposed the following objective rate or equation (4.72)

$$\underline{\overset{\delta}{\sigma}} = \underline{\dot{\sigma}} + \underline{\sigma} \cdot \underline{\Omega} - \underline{\Omega} \cdot \underline{\sigma}. \quad (4.108)$$

Another stress rate proposed in this work is defined as

$$\underline{\overset{*}{\sigma}} = \underline{\dot{\sigma}} + \underline{\sigma} \cdot \underline{\phi} - \underline{\phi} \cdot \underline{\sigma}. \quad (4.109)$$

The above stress rates are employed to ascertain what effect the rotations will have on the resulting stresses.

If (4.107) is substituted into (4.106) we find that

$$\begin{aligned} \dot{\sigma}_{11} - \dot{S} \alpha_{12} &= 0 \\ \dot{\sigma}_{12} + \dot{S}/2 \sigma_{11} - \dot{S}/2 \sigma_{22} &= \mu \dot{S} \\ \dot{\sigma}_{22} + \dot{S} \sigma_{12} &= 0, \end{aligned} \quad (4.110)$$

combining these equations, and noting that $\ddot{S} = 0$, the following

differential equation is obtained

$$\frac{d^2 \sigma_{11}}{dt^2} + \dot{S}^2 \sigma_{11} = \mu \dot{S}^2. \quad (4.111)$$

The above equation can be solved explicitly, and for an initially stress-free state the solution for the stresses is

$$\begin{aligned} \sigma_{11} &= \mu (1 - \cos \dot{S}t) \\ \sigma_{12} &= \mu \sin \dot{S}t \\ \sigma_{22} &= -\mu (\cos \dot{S}t - 1). \end{aligned} \quad (4.112)$$

The above equation predicts that the stresses are periodic and this is physically incorrect. The variation of the non-dimensional stresses (σ_{11}/μ and σ_{12}/μ) with the shear displacement S is shown in Figure 4.4.

It is to be noted that Nagtegaal and De Jong [39] have calculated a periodic variation in stresses for both elastic-plastic and rigid-plastic solids undergoing rectilinear shear based on a kinematic hardening model. The position of the centre of the yield locus was characterised by a shift (or back-stress) tensor \mathbf{g} , and the objective rate of change of this tensor was taken to be the Jaumann derivative. Lee and his co-workers [40] have considered alternative rotation terms (different to any of those employed here) in the objective back stress rate as means of eliminating the oscillation in the stress components. In both Refs. [39 and 40] the results were obtained numerically using a finite element analysis. While the implications of the findings are clear, the numerical scheme tended to mask the precise role of a particular objective stress rate. It is considered that the present work demonstrates the influence in a much more direct and lucid manner.

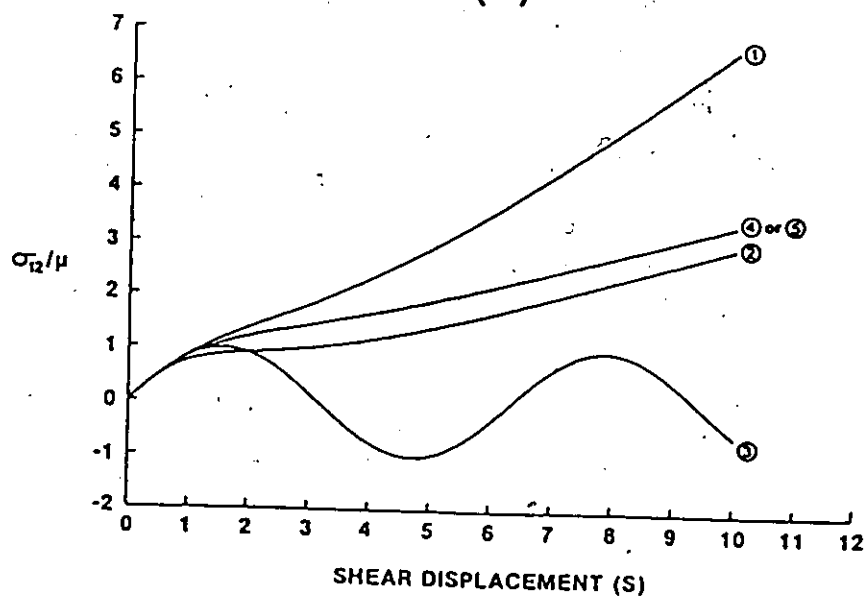
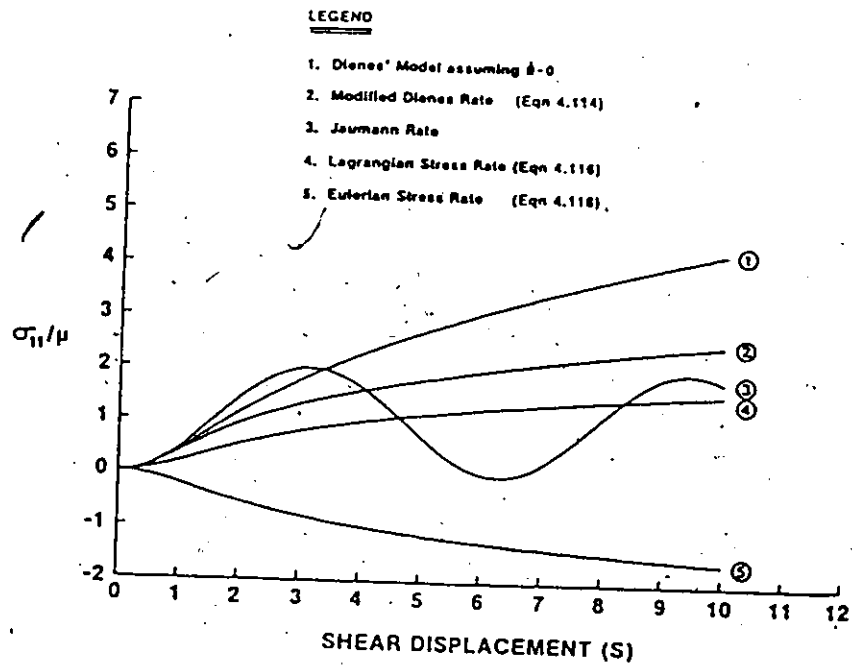


Figure 4.4: Diagram illustrating the variation of non-dimensional stresses with respect to the shear displacement S .

- (a) σ_{11}/μ versus S .
 (b) σ_{12}/μ versus S .

If (4.108) is substituted into (4.106) we find

$$\begin{aligned}\ddot{\sigma}_{11} &= \dot{\sigma}_{11} - 2\Omega_{12}\sigma_{21} = 2\mu D_{11} = 0 \\ \ddot{\sigma}_{12} &= \dot{\sigma}_{12} - \Omega_{12}\sigma_{22} + \sigma_{11}\Omega_{12} = 2\mu D_{12} \\ \ddot{\sigma}_{22} &= \dot{\sigma}_{22} + 2\Omega_{12}\sigma_{12} = 2\mu D_{22} = 0\end{aligned}\quad (4.113)$$

The above equations can be combined to yield

$$\frac{d^2\sigma_{11}}{d\theta^2} + \frac{d\sigma_{11}}{d\theta} 2\tan\theta + 4\sigma_{11} = 4\mu\sec^2\theta \quad (4.114)$$

In solving (4.113) Dienes, op cit, assumed that $\ddot{\theta} = 0$, which is not true if $\ddot{S} = 0$, as can be seen from (4.100). With $\ddot{\theta} = 0$, the $\tan\theta$ term in (4.114) vanishes, and the equation can be solved explicitly [35]. As it stands the equation must be solved numerically, and this was done in the present work. The corresponding shear stress is given by

$$\sigma_{12} = \frac{1}{2} \frac{d\sigma_{11}}{d\theta} \quad (4.115)$$

The variation of the non-dimensional stresses σ_{11}/μ and σ_{12}/μ with S is shown in Fig. 4.4, also illustrated, is the result obtained by Dienes [35] by assuming $\ddot{\theta} = 0$.

Finally conjoining (4.109) with (4.106), and adopting the same procedure leading to (4.113) and (4.114) we obtain the differential equation

$$\frac{d^2\sigma_{11}}{d\phi_L^2} - \frac{d\sigma_{11}}{d\phi_L} 4 \cot 2\phi_L + 4\sigma_{11} = 8\mu \operatorname{cosec}^2 2\phi_L, \quad (4.116)$$

which has to be solved numerically. The shear stress is obtained from

$$\sigma_{12} = \frac{1}{2} \frac{d\sigma_{11}}{d\phi} \quad (4.117)$$

The variation of σ_{12}/μ with S is demonstrated in Fig. 4.4(b).

Rather than use the spin of the Lagrangian ellipsoid in (4.109), which finally leads to (4.116) and (4.117), the spin of the Eulerian ellipsoid could have been adopted. The Eulerian spin tensor, defined by equation (4.76) can be evaluated from (4.97) in a like manner to the Lagrangian spin. The solution of the stresses follows in an identical fashion, and instead of (4.116) and (4.117) the following differential equations are determined

$$\frac{d^2 \sigma_{11}}{d\phi_E^2} - \frac{d\sigma_{11}}{d\phi_E} - 4 \cot \phi_E + 4\sigma_{11} = -8\mu \operatorname{cosec}^2 2\phi_E, \quad (4.118)$$

and

$$\sigma_{12} = \frac{1}{2} \frac{d\sigma_{11}}{d\phi_E}, \quad (4.119)$$

which have to be solved numerically. It transpires that the variation of σ_{12}/μ with S is exactly the same as that obtained when using the Lagrangian spin. For more details of the above derivations the readers are referred to Appendix F.

4.5.1 Discussion

The result of the non-dimensional normal stress σ_{11}/μ versus the shear displacement S is plotted in Figure 4.4(a) while that of the shear stress σ_{12}/μ with S is given in Figure 4.4(b). It is evident from Figure 4.4 that the proposed objective stress rates have a significant influence on the evolution of the stresses. Only the Jaumann rate leads to an oscillation in the normal and shear components of stress, and as

already remarked this is physically unacceptable. However the oscillation does not begin until a relatively large shear displacement has been attained. At small displacement all the objective rates give essentially the same shear stress. In the present examination, the modified Dienes solution provides a much lower stress level and it falls within the domain of the classical Jaumann rate for large strain; notice that the components of stress obtained would be erroneous, if $\ddot{\theta}$ is neglected when $\ddot{S} = 0$, as was done by Dienes. It has already been demonstrated in equation (4.100) that this is inaccurate. Figure 4.4 indicates that the difference in stresses of the two solutions increases when the shear strain is above 100 percent.

The objective rate involving the spin of either the Eulerian or Lagrangian ellipsoid results in a shear stress variation that follows very closely the shear stress derived using the Jaumann rate, up to a shear displacement in excess of unity. Although, the component of the non-dimensional normal stress σ_{11}/μ obtained from the spin of the Eulerian ellipsoid possesses entirely different behaviour from any one of the stress rates described above (see Figure 4.4(a)). Due to large rotation of material element, the rate of rotation of the Lagrangian triad, $\dot{\phi}_L$, counteracts that of the Eulerian strain triad, $\dot{\phi}_E$, such that the same shear stress behaviour reveals, although the direct stresses are completely different.

It is suggested that the stress rates developed in this work may be employed for analyzing problems involving large strain and/or large rotations in order to assess the various components of stress.

4.5.2 Conclusions

The earlier part of this chapter dealt with choice of an appropriate strain measure for pure homogeneous deformation. In keeping with previous proposals, to be found in earlier published work, logarithmic (or natural) strain was deemed to be suitable. As is well known the material time derivation of this strain measure is equal to the rate of deformation tensor. No such simple relationship holds when the deformation occurs by a homogeneous mode i.e. an unsymmetric deformation gradient tensor. However, an attempt has been made to establish relationships between a time derivative of $(\ln U)$ and the rate of deformation tensor, \underline{D} . The resulting expressions are quite complex and their utility in any numerical scheme awaits demonstration.

As mentioned herein a number of different "rotation" tensors can be defined in finite homogeneous deformation. A number of these rotation tensors have been defined in the chapter. Somewhat earlier Hill had evaluated the spin (or rate of rotation) of the so called Lagrangian and Eulerian strain ellipsoids, following a superimposed infinitesimal deformation step on a pre-existing finite deformation mode. Similar calculations have been performed here but from a different theoretical standpoint, and the writer believes the spin terms have been determined in a more straightforward manner.

The existence of different rotation tensors give rise to a number of different objective stress rates, which are all available for adoption in constitutive equations. The latter part of this chapter has dealt with how the choice of a particular stress rate can influence the

evaluation of the stresses in finite deformation process. As an illustration, stress calculations were performed for hypoelastic material undergoing simple (rectilinear) shear the results using the different stress rates are compared with those obtained using the classical Jaumann rate. It transpires that for small strain all the objective stress rates can be employed. However, at strain in excess of unity the Jaumann rate gives rise to unacceptable oscillations in stress. Such oscillations were not present with the other objective stress rates, and in particular those stress rates which were a function of the spin of the Eulerian or Lagrangian strain ellipsoids were shown to be appropriate. Nonetheless the utility of the various stress rates adopted herein in any numerical schemes for analyzing problems involving large strain and/or large rotations awaits further demonstration.

APPENDIX A

The Evaluation of Finite Strain

If we consider the case of pure homogeneous deformation then the deformation gradient tensor is a symmetric second order tensor, say $\underline{F} = \underline{U}$, and the eigenvalues and eigenvectors (the principal stretch ratios and their orientation) can be obtained in the usual way. Consequently it makes no difference whether the components of the tensor are finite or infinitesimal in extent, as to the manner in which the eigenvalues and eigenvectors are determined.

For simplicity a two dimensional deformation mode is considered, such as a thin incompressible membrane being deformed in its own plane. In such a case it is demonstrated below how the eigenvalues and eigenvectors can be evaluated from a Mohr's circle construction, a technique familiar to most engineers.

As already described in Chapter 2 the new coordinates (x,y) of a point are a linear function of the initial coordinates, say (X_0, Y_0) , such that

$$\bar{x} = \underline{F} \cdot \bar{X}_0 \quad (\text{A.1})$$

However, under the pure homogeneous straining mode illustrated in Figure 2.1, the coefficients of \underline{F} in (A.1) are symmetric. A geometric interpretation of the coefficients is available from Figure 2.1 in conjunction with Equation (2.1).

On the basis of the deformation model shown in Figure 2.1, it is

easily verified that

$$\begin{aligned} F_{11} &= 1/2(\lambda_{11} + \lambda_{22}) + 1/2(\lambda_{11} - \lambda_{22})\cos 2\theta \\ F_{22} &= 1/2(\lambda_{11} + \lambda_{22}) - 1/2(\lambda_{11} - \lambda_{22})\cos 2\theta \\ F_{12} = F_{21} &= -\sin 2\theta(\lambda_{11} - \lambda_{22})/2 \end{aligned} \quad (\text{A.2})$$

where λ_{11} , λ_{22} are principal elongation ratios while θ , the principal orientation.

From (A.2) it is apparent that the coefficients are derivable from a Mohr's circle construction. The circle has extreme values λ_{11} , λ_{22} and is of radius $1/2(\lambda_{11} - \lambda_{22})$, see Figure (A.1). The orientation of the principal axes is determined from

$$\tan 2\theta = \frac{2F_{12}}{F_{11} - F_{22}} \quad (\text{A.3})$$

and the principal elongation ratios from

$$\lambda_{11}, \lambda_{22} = \frac{F_{11} + F_{22}}{2} \pm \frac{(F_{11} - F_{22})}{2} \frac{1}{\cos 2\theta} \quad (\text{A.4})$$

or

$$\lambda_{11}, \lambda_{22} = \frac{F_{11} + F_{22}}{2} \pm \sqrt{\left(\frac{F_{11} - F_{22}}{2}\right)^2 + F_{12}^2} \quad (\text{A.5})$$

When interpreting the orientation of the eigenvectors, given by (A.3), using Mohr's circle it is necessary to adopt a sign convention when fixing the "shear" components, F_{12} and F_{21} , on the circle. With reference to Fig. 2.1, when the original right angle, $\angle COA$, decreases both F_{12} and F_{21} are regarded as positive in (A.3) but F_{21} is plotted as negative in Mohr's circle as shown in Fig. (A.1). Just the reverse occurs when the original right angle increases.

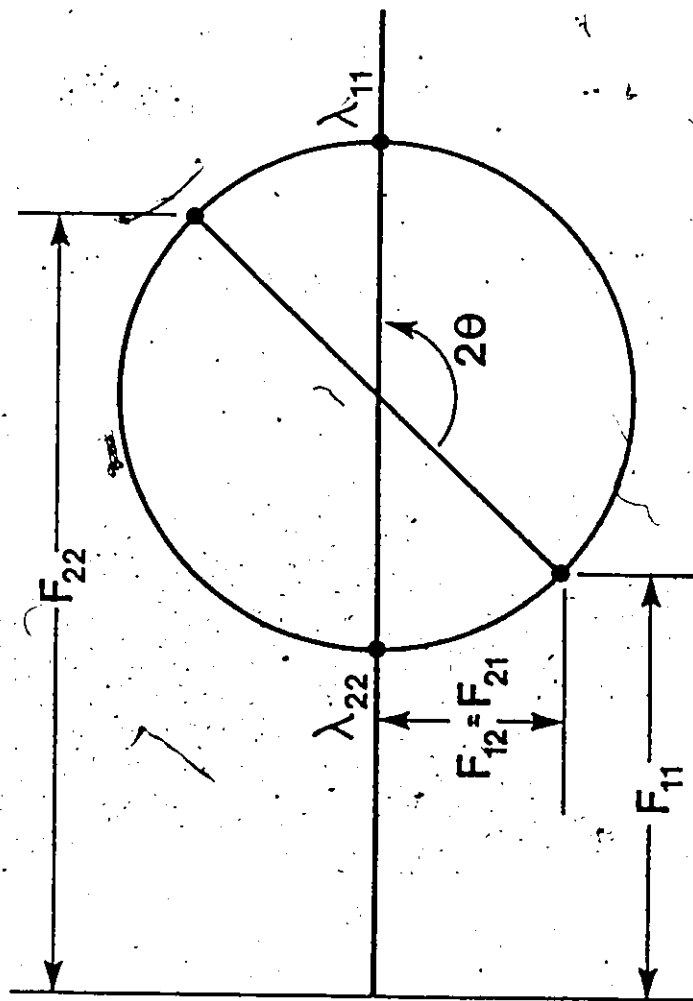


Figure A.1: Mohr circle representation of finite strain.

APPENDIX B

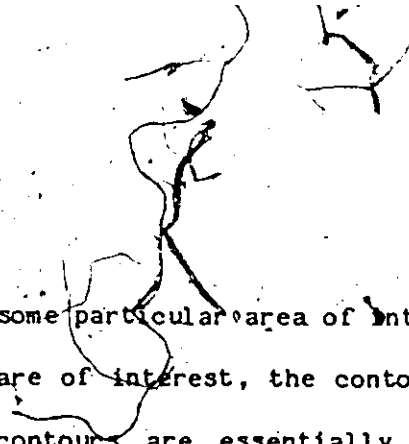
The Plotting of Strain Contours

Introduction

One of the major problems with many numerical techniques, particularly the finite element method, is the voluminous output produced by the analysis and the time required to interpret these results. Quite often the results are obtained at a great many discrete points and this makes the task of reading the results very difficult. The use of the automatic plotter to produce a visual interpretation of the various aspects of the computed data alleviates this difficulty to a great extent. A number of graphical methods may be used, some of which are:

- a) isoclinic lines, or lines of constant principal angle,
- b) strain trajectories, which are the loci of the directions of constant principal strain,
- c) isostrain or strain lines — equal strain contours,
- d) principal surface strain plot, using ϵ_1 and ϵ_2 as coordinate axes. The principal surface strains evaluated within a grid element is represented by one point (or a vector) in this space,
- e) isometric strain plot, in which a strain "surface" is plotted in an isometric view.

Contours of strain level are one of the most convenient types of display. They may be drawn over the whole area of the system or over



some particular area of interest. When regions of high strain gradients are of interest, the contour plot is the most informative. The strain contours are essentially slices of equal magnitude of the surface projected onto the x-y plane. Regions of high strain gradients are easily recognizable as contour lines that bunch together. Some of the methods mentioned above have been discussed in many finite element texts.

As described in section 2.2.2, a new technique for grid strain determinations from a deformed pair of lines has been discussed. These analytical procedures allow for the evaluation of the magnitude and orientation of the strain on the surface of sheet metal stampings although in regions of high strain gradients, elements may exhibit discontinuity in strain from one element to the next across the sheet. In order to facilitate the interpretation of strain on the initial undeformed sheet, two types of averaging of strains of two adjacent elements are employed. In one where a quadrilateral is formed from two defined triangles, the average strain of the two triangles is taken as the strain at the centroid of the quadrilateral. In the ~~second type~~ the strains of all the triangular elements connected to a node are summed and divided by the number of elements as shown in Figure B.1, i.e., the strain at A is equal to one-sixth of the sum of the strains of all six elements surround it. In this work, the latter method is employed for contour display. This technique usually gives a fairly smooth strain distribution, however the boundary nodes and nodes in regions of high strain gradients are not necessarily well smoothed.

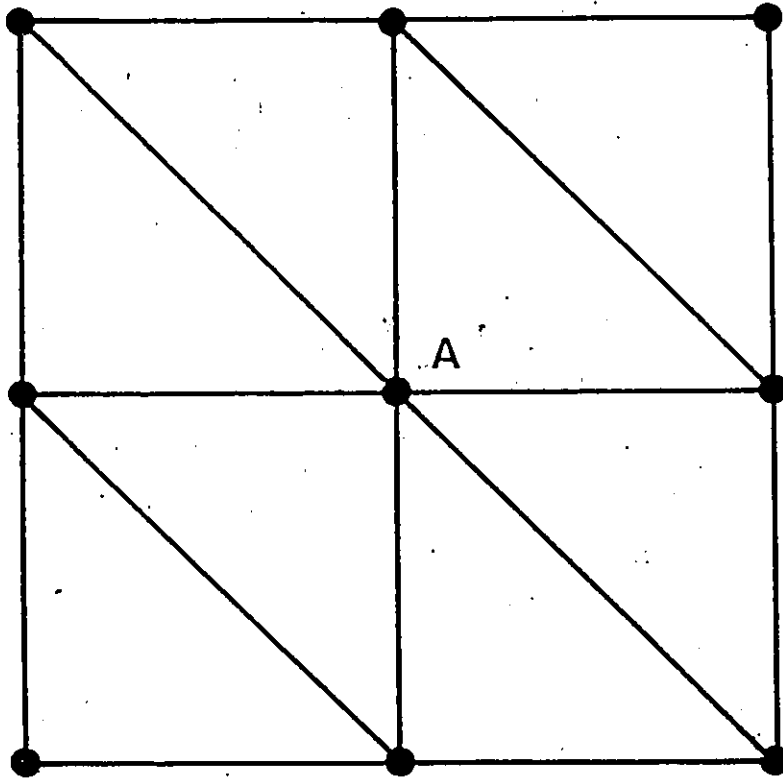


Figure B.1: The strain at A is the mean average of sum of strains of the surrounding elements connected to node A.

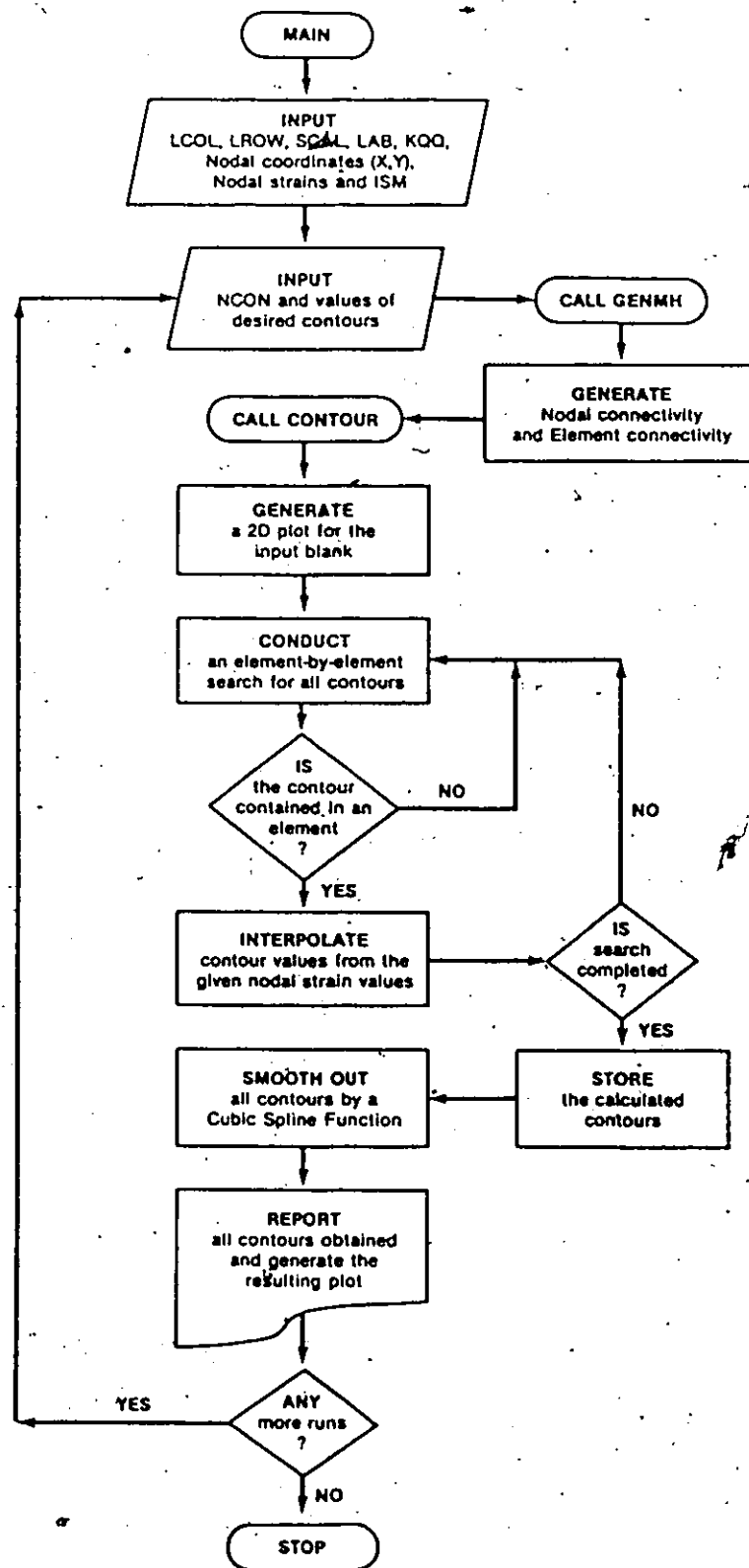


Figure B.2: A flow chart of contour developments.

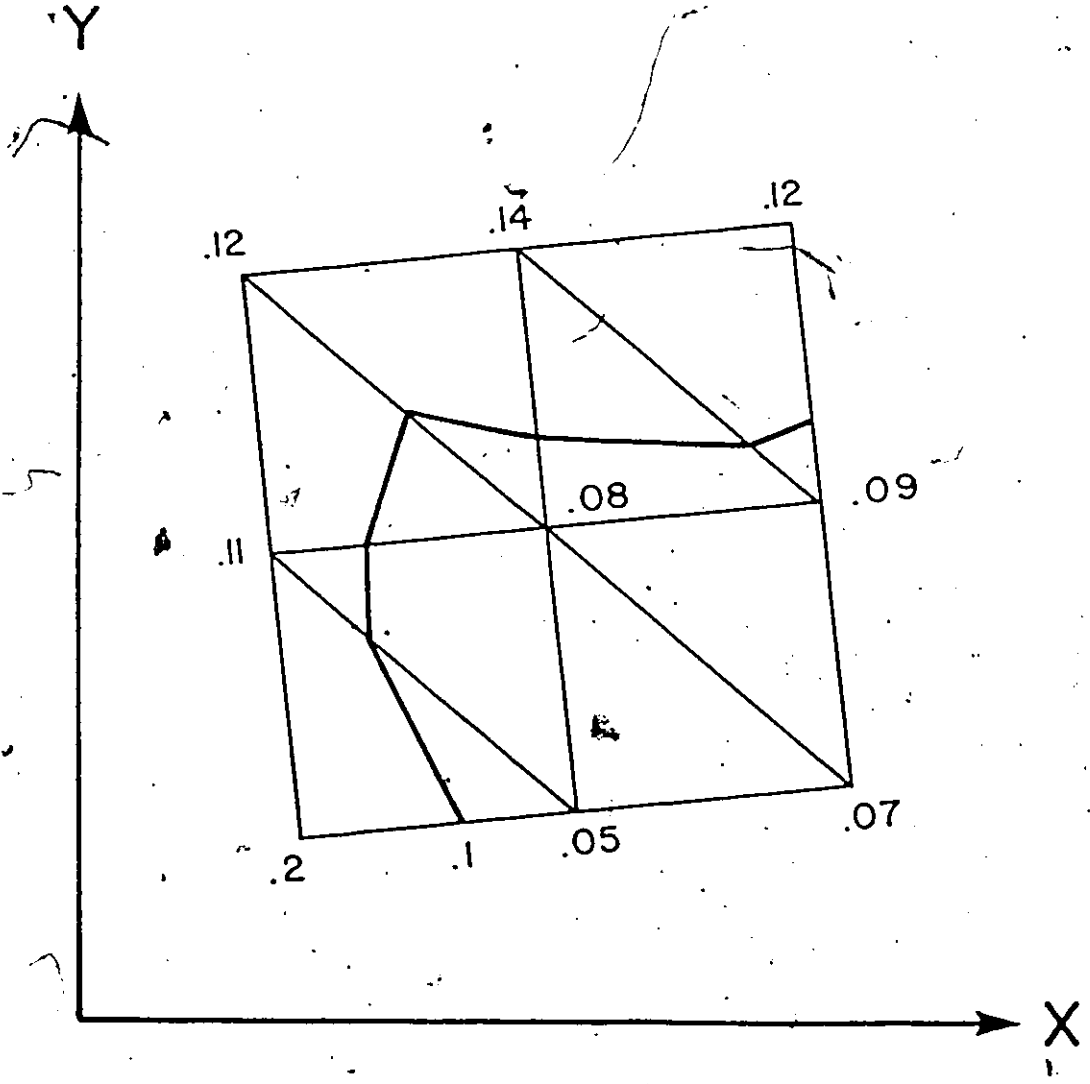


Figure B.3: Diagram showing a contour line formed by straight segments between points.

Nonetheless, with the advance in the use of computer graphics, a visual display of contour lines can be very convenient and helpful. Areas of peak strain are immediately obvious to a part designer, the necessary changes and adjustments to the component under consideration can then be made and a more desirable component may be achieved.

In this Appendix, a contour plotting technique is discussed. Though the present routine provides contour plots only on a 2D plane, the development is general enough that this could be modified to give a 3D contour display. The computer program uses the basic library plotting subroutine PLOT to draw the contours. It has been successfully used on the Versatec and Calcomp plotters. A program listing and user procedures for running the program can be found in a report [41] compiled by the writer. For completeness, a flow chart of the logical development of the routine is given in Figure B.2.

Basic Concept

The basic idea for contour plottings is explained by means of an example as shown in Figure B.3. Values of nodal strain are indicated on the diagram. Suppose that 10% strain contour is required, i.e., strain value of 0.1, the computer will then perform an element-by-element search to establish which element the contour passes through. Once the element is identified, the intersections of the contour with the sides of the element are determined by linear interpolation. This procedure is repeated as many times as there are numbers of elements and the possible intersection points for the required strain contour can be

obtained. For simple contour plotting, all these points are joined together in a successive order by segments of straight lines. The contour will then be piecewise linear as shown in Figure B.3.

Cubic Spline Interpolation

In the present program, a more complicated method, the so-called Cubic Spline method of interpolation and smoothing, is used to smooth the contour. The coordinations (x,y) of the points defining the contour are consecutively stored in arrays. The smoothing is done by connecting these coordinations by a cubic spline function in such a way that the resulting curve possesses continuous first and second derivatives; this ensures that there are no kinks in the contour. The distance along the x-direction, between points defining the contour, are subdivided into smaller intervals and the y intervals are interpolated using the Spline method. The sub-intervals are so close that they give the appearance of a smooth curve when joined up by straight lines. The computer program is also capable of handling multi-valued contours in x.

Given a set of points x_0, x_1, \dots, x_n and a set of corresponding prescribed ordinates y_0, y_1, \dots, y_n , it is possible to best fit each consecutive pair of points $(x_{i-1}, y_{i-1}), (x_i, y_i)$ by a cubic function so chosen that the resulting curve has continuous first and second derivatives. In beam theory, it is well known that the Spline assumes the shape which minimizes its potential energy and that this curve closely approximates the deflected configuration of a simply supported thin beam.

Let us designate M_0, M_1, \dots, M_n as the second derivatives at the node x_i of the function $S(x)$ of the resulting Spline. The second derivative $S''(x)$ is a linear function between the junctions, which interpolates M_i . Therefore, for $x_{i-1} \leq x \leq x_i$ we have

$$S''(x) = M_{i-1} \frac{x_i - x}{h_i} + M_i \frac{x - x_{i-1}}{h_i} \quad (\text{B.1})$$

where $h_i = x_i - x_{i-1}$

Integrating twice we have

$$S'(x) = -M_{i-1} \frac{(x_i - x)^2}{2h_i} + M_i \frac{(x - x_{i-1})^2}{2h_i} + C_i \quad (\text{B.2})$$

$$S(x) = M_{i-1} \frac{(x_i - x)^3}{6h_i} + M_i \frac{(x - x_{i-1})^3}{6h_i} + C_i (x - x_{i-1}) + D_i \quad (\text{B.3})$$

The integrating constants C_i and D_i may be determined by setting $S(x_{i-1}) = y_{i-1}$ and $S(x_i) = y_i$, hence

$$y_{i-1} = M_{i-1} \frac{h_i^2}{6} + D_i$$

$$y_i = M_i \frac{h_i^2}{6} + C_i h_i + D_i$$

solving these equations, we obtain

$$C_i = \frac{y_i - y_{i-1}}{h_i} + (M_i - M_{i-1}) \frac{h_i}{6}$$

$$D_i = y_{i-1} - M_{i-1} \frac{h_i^2}{6}$$

Equations (B.2) and (B.3) become

$$\begin{aligned}
 S(x) = & M_{i-1} \frac{(x_i - x)^3}{6h_i} + M_i \frac{(x - x_{i-1})^3}{6h_i} + (y_{i-1} - \frac{M_{i-1} h_i^2}{6}) (\frac{x_i - x}{h_i}) \\
 & + (y_i - \frac{M_i h_i^2}{6}) (\frac{x - x_{i-1}}{h_i}) \quad (B.4)
 \end{aligned}$$

$$S'(x) = -M_{i-1} \frac{(x_i - x)^2}{2h_i} + M_i \frac{(x - x_{i-1})^2}{2h_i} + \frac{y_i - y_{i-1}}{h_i} - \frac{M_i - M_{i-1}}{6} h_i \quad (B.5)$$

Though the quantities M_i are as yet unknown, the continuity of $S(x)$ and $S''(x)$ are enforced by the choice of the equations described above.

Evaluating $S'(x)$ at the end points of the sub-interval gives

$$\begin{aligned}
 S'_+(x_i) &= M_i \frac{h_i}{2} + \frac{y_i - y_{i-1}}{h_i} - \frac{M_i - M_{i-1}}{6} h_i \\
 &= M_i \frac{h_i}{3} + M_{i-1} \frac{h_i}{6} + \frac{y_i - y_{i-1}}{h_i} \quad (B.6)
 \end{aligned}$$

$$\begin{aligned}
 S'_-(x_{i+1}) &= -M_i \frac{h_{i+1}}{2} + \frac{y_{i+1} - y_i}{h_{i+1}} - \frac{M_{i+1} - M_i}{6} h_{i+1} \\
 &= \frac{y_{i+1} - y_i}{h_{i+1}} - M_i \frac{h_{i+1}}{3} - M_{i+1} \frac{h_{i+1}}{6} \quad (B.7)
 \end{aligned}$$

Since the formula $S(x)$ holds only on the interval $[x_i, x_{i+1}]$, and so the derivatives at the end points are one-sided derivatives. To ensure continuity in $S'(x)$, the following conditions must be imposed at the interior node $S'_-(x_i) = S'_+(x_i) \quad i=2, \dots, n-1$. This follows immediately by equating equations (B.6) and (B.7), yields

$$\frac{h_i}{6} M_{i-1} + \frac{h_i + h_{i+1}}{3} M_i + \frac{h_{i+1}}{6} M_{i+1} = \frac{y_{i+1} - y_i}{h_{i+1}} - \frac{y_i - y_{i-1}}{h_i}$$

Setting $\mu_i = \frac{h_{i+1}}{h_i + h_{i+1}}$ and $\mu_i' = 1 - \mu_i$, we obtain

$$\mu_i' M_{i-1} + 2M_i + \mu_i M_{i+1} = 6 \frac{\frac{y_{i+1} - y_i}{h_{i+1}} - \frac{y_i - y_{i-1}}{h_i}}{h_i + h_{i+1}} \quad (\text{B.8})$$

This is a system of $i-1$ equations to be satisfied by the $n+1$ unknowns M_0, M_1, \dots, M_i . Hence two additional conditions must be specified to uniquely define the interpolating Spline function. It is noticed that by setting the end conditions $M_0 = M_i = 0$ leads to simply supported at the end points. For more general cases

$$M_0 - \theta M_1 = 0, \quad 1 > \theta > 0. \quad (\text{B.9})$$

Nonetheless, it is more convenient to specify the slope at the end of the curve instead. We have, from equations (B.4) and (B.6)

$$S'(x_0) = \frac{y_1 - y_0}{h_1} - \frac{h_1}{3} M_0 - \frac{h_1}{6} M_1 \quad (\text{B.10a})$$

$$S'(x_1) = \frac{y_1 - y_{i-1}}{h_1} + \frac{h_1}{3} M_1 - \frac{h_1}{6} M_{i-1} \quad (\text{B.10b})$$

In general, we employ the end conditions of

$$2M_0 + \mu_0 M_1 = d_0 \quad (\text{B.11a})$$

$$\mu_i' M_{i-1} + 2M_i = d_i \quad (\text{B.11b})$$

Choosing the following sets of combination of μ_0 and d_0 , equation (B.11a) and (B.10a) will be completely satisfied respectively:

$$\mu_0 = -2\theta \text{ and } d_0 = 0 \quad (\text{B.12})$$

$$\mu_0 = 1 \text{ and } d_0 = \frac{6}{h_1} \left[\frac{y_1 - y_0}{h_1} - S'(x_0) \right]$$

Similarly, the condition

$$M_i = \theta M_{i-1}$$

together with equations (B.11b) and (B.10b) are satisfied by the following chosen situations:

$$\mu_i' = -2\theta ; d_i = 0$$

(B.13)

$$\text{and } \mu_i' = 1; d_i = \frac{6}{h_i} \left[S'(x_i) - \frac{y_i - y_{i-1}}{h_i} \right]$$

upon satisfying equation (B.11), the system of simultaneous equations indicated below can now be solved:

$$\begin{aligned} 2M_0 + \mu_0 M_1 &= d_0 \\ \mu_1' M_0 + 2M_1 + \lambda_1 M_2 &= d_1 \\ \mu_2' M_1 + 2M_2 + \lambda_2 M_3 &= d_2 \\ &\vdots \\ \mu_{i-1}' M_{i-2} + 2M_{i-1} + \lambda_{i-1} M_i &= d_{i-1} \\ \mu_i' M_{i-1} + 2M_i &= d_i \end{aligned}$$

A more comprehensive exposition of the theory of splines and their applications can be found in refs. [41-44].

APPENDIX C

The Mapping of a Hemispherical Shell: a Test Case

Introduction

In the early investigation of the mapping process, application of the modelling to a typical car seat stamping indicated that the mapping technique required improvement. Due to the complexity of a stamped shape, it is necessary to derive an alternative means to ascertain what extent the effects of the size and configuration of the hand drawn mesh might have on this computer-aided model. In addition to mapping tests with a real stamping, an artificial test case has been developed in hope of providing a "correct" solution against which the actual mapping could be compared.

In this appendix the forming of a hemispherical shell from a flat, circular disc is described. The exact blank shape is generated for an arbitrarily chosen thickness distribution. The correct result is compared with the blank developed by some of the mapping procedures described in Section 3.3.2 of Chapter 3. Since the mapping follows arbitrary inputs, the results may depend on the configuration of the mesh. Various types of the mesh are employed in the test case to determine the sensitivity of the result to the grid geometry. In the future development of this computer-aided system the designer can impose adjustments on the strain distribution. The test case may serve as a means of vindicating the methods of adjustment, surface modification and

reverse mapping, etc. Examples are given of the remapping and surface adjustment techniques. The details of the investigation can be found in an internal report [17], compiled by the author. The present case study permits future expansion in conjunction with the tool and die designer's experience.

The Test Case

The case considered is the deformation of a flat, circular disc to a hemispherical shell. The deformation is axisymmetric and the thickness around some circle of latitude defined by the angle θ is assumed constant as shown in Figure C.1. The thickness distribution can be defined by some arbitrary relation, for example,

$$t = t_0 + k\theta^2$$

as illustrated in Figure C.2. As the deformation is axisymmetric, the position of a generic point $P(X, Y, Z)$ of the hemisphere can be relocated onto the flat blank by a simple analytical relation. The position vector \vec{r}_0 of the point $p(x, y)$ on the flat blank is related to the angle θ . Consider the volume of a circular element in the hemisphere shown in Figure C.1 and its corresponding volume on the blank. The following equations hold

$$v = \pi r_0^2 t_0 \quad (C.1)$$

$$V = 2\pi r drt \quad (C.2)$$

$$t = t_0 + k\theta^2 \quad (C.3)$$

where v is the volume of an element on the 2D plane, V is the volume of an element on the hemisphere and the position vector $\vec{r}_0 = x_0 \vec{i} + y_0 \vec{j}$.

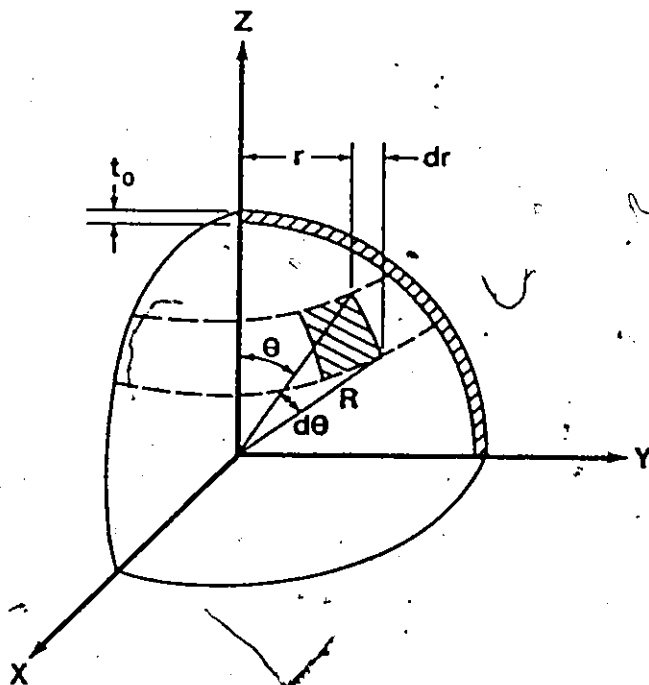


Figure C.1: Schematic of one quarter of the hemispherical shell under consideration.

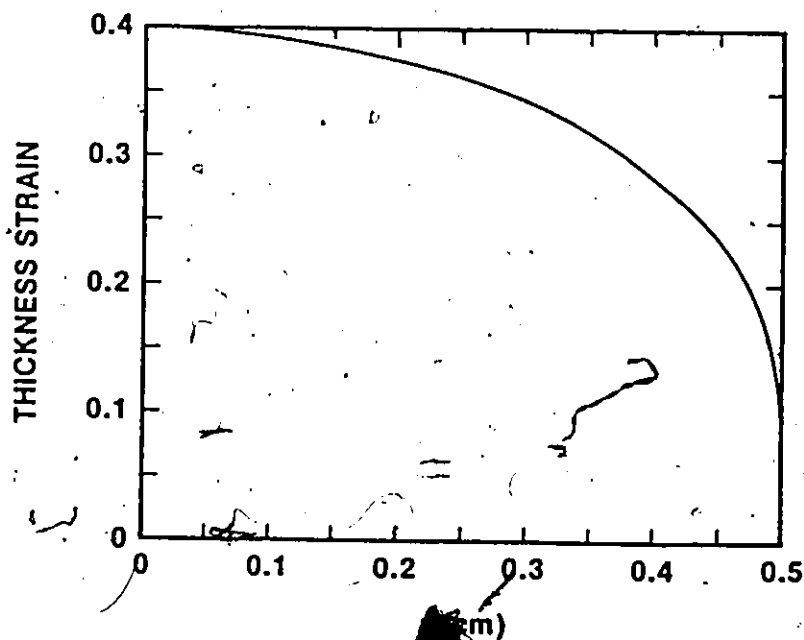


Figure C.2: A typical thickness strain distribution of the hemisphere in Fig. C.1

Upon integrating (C.2) over a circular latitude of angle θ and combining with (C.3), there results

$$\begin{aligned} V &= 2\pi R \sin\theta (Rd\theta) t \\ &= \int_0^\theta 2\pi R^2 (t_0 + k\theta^2) \sin\theta d\theta \\ &= 2\pi R^2 [t_0 - t_0 \cos\theta + 2k\theta \sin\theta - k\theta^2 \cos\theta + 2k\cos\theta - 2k] \end{aligned}$$

The condition of incompressibility yields

$$r_0^2 = \frac{2R^2}{t_0} [t_0 - 2k + 2k\theta \sin\theta + (2k - t_0 + k\theta^2) \cos\theta], \quad (C.4)$$

where

$$r_0^2 = x_0^2 + y_0^2. \quad (C.5)$$

Since each point can only move radially, the coordinate position on the flat blank, x_0, y_0 , satisfies the relation

$$\frac{x}{x_0} = \frac{y}{y_0} \quad (C.6)$$

The solution is completely determined by combining equations (C.4), (C.5) and (C.6).

One-quarter of the hemispherical shell is considered and an irregular mesh of points established on the surface, as illustrated in Fig. C.3. In order to satisfy constraints in the existing mapping process, this mesh consists of rows and columns of equal numbers of elements.

Mapping, Assuming No Change in Thickness of Blank

The example considered here is the deformation of a flat, circular blank into a hemisphere, assuming no change in thickness. The

"correct" (analytical) map for the case is shown in Figure C.4. Each nodal point of the irregular mesh in Figure C.3 is mapped onto the flat plane using the analytical solution. Considering the reverse processes, from the flat blank to the hemisphere, it is obvious that the "constant thickness" process involves compressive strains in the circumferential directions and tensile strains in the radial directions.

In order to execute the various mapping strategies, it is necessary to establish some boundary nodes. As indicated in Figure C.3, XOZ and YOZ planes are planes of symmetry, and displacements perpendicular to these planes vanish. In the present case, the analytical solution is used to establish the position of the nodes on axes of symmetry on the flat blank. The element-by-element techniques can then be used to map elements onto the flat blank. Three mapping techniques will be adopted for the transformation - namely the proportional deformation, the intersection method and the area criterion.

(a) Proportional Deformation

Initially, the hemisphere shown in Figure C.3 is mapped onto a flat plane using the strategy of proportional deformation, the description of the proportional displacement is described in Section 3.3.2 of Chapter 3. The result of the mapping is given in Figure C.5. Superposition of the "correct" blank shape and the mapped solution indicates inadequacies in the mapping procedure. It is apparent that

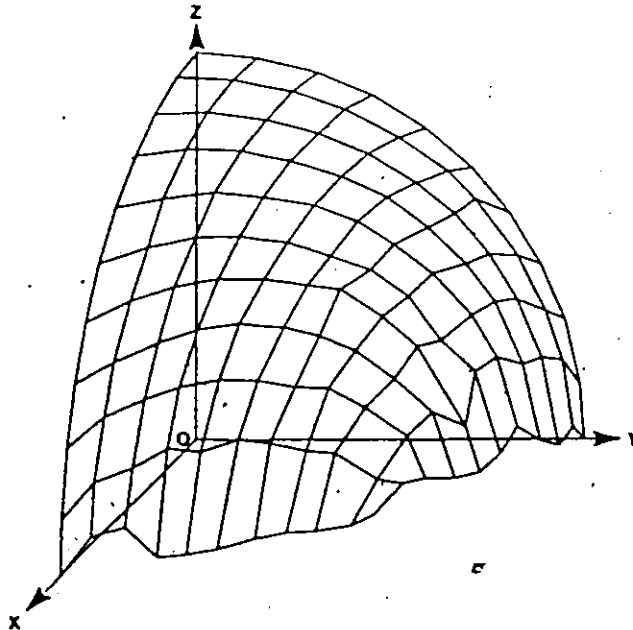


Figure C.3: Arrays of quadrilateral elements on the surface of part of the hemisphere.

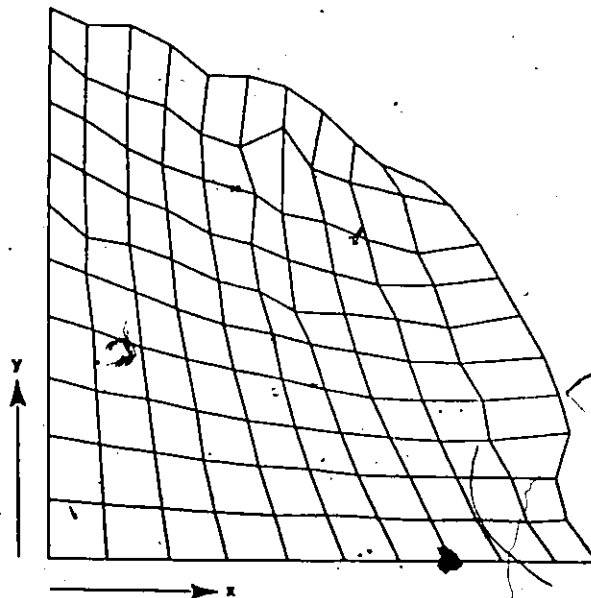


Figure C.4: The "correct" analytical map of the shell surface in Fig. C.3.

the orientation of the element with respect to the "correct" principal direction influences its mapped shape in some inappropriate fashion. The strategies described in the following two sections are aimed at overcoming the shortcomings of the proportional deformation method.

(b) Intersection Method

The intersection method is described in Section 3.3.2, Chapter 3, and the blank developed by this technique is shown in Fig. C.6. It is observed that a simple blank shape could not be generated, and overlapping of some elements occurred. The method does not appear satisfactory in regions where elements are irregular. The position of the fourth node of an element is located by taking into account not only the element itself but also the deformation of the neighbouring elements, hence a small oscillation in one element appears to exert a strong influence on the location of the nodal point. The technique is found wanting and the strategy described in the next Section is shown to be an improvement.

(c) Area Criterion

Again, in this case the analytical solution is used to establish the boundary nodes on the flat plane along the axes of symmetry. The mapping process can now be conducted on each element of the irregular mesh shown in Figure C.3. The location of the fourth node of the element is determined in such a way that the thickness of the resulting element is approximately unchanged. Details of the mapping strategy can

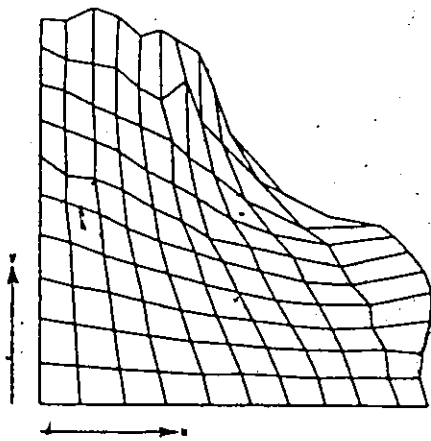


Figure C.5: The resulting blank obtained from the assumed proportional deformation of Fig. C.3.

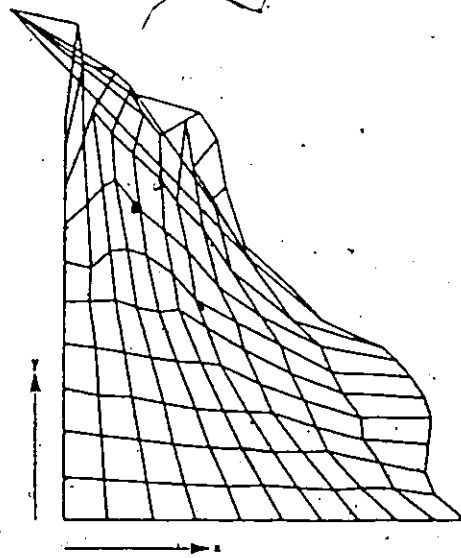


Figure C.6: The resulting map of Fig. C.3. showing collapse of elements occurs with the intersection method.

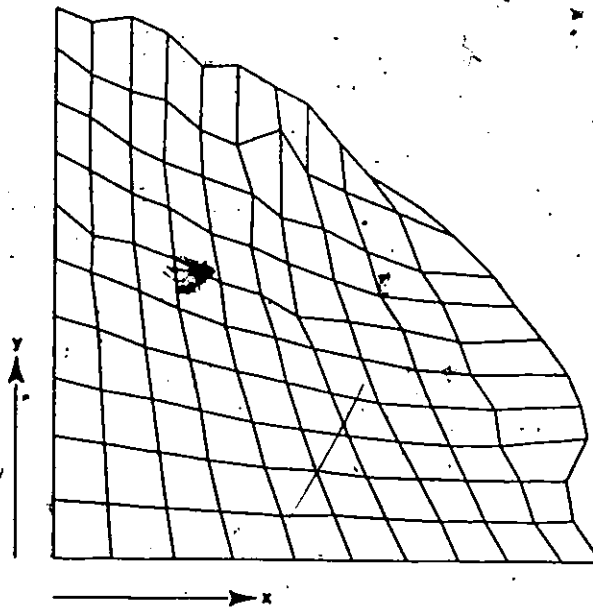


Figure C.7: "constant area" transformation of the hemispherical shell on a flat blank.

be found in section 3.3.2. The blank developed by this technique is shown in Figure C.7.

Upon superimposing of the mapped solution onto the "correct" blank shape excellent agreement between the two results is obtained. The mapping technique does not provide a perfect match, nonetheless this test suggests that the present method appears to function well when applied to the hemispherical shell. Since the input of the irregular grid points is rather arbitrary, the small discrepancy that appeared in the final blank shape indicates that this technique could be dependent on the shape and size of the elements, i.e. the deformation of the sheet is governed by geometry of the stamping and the irregularity of the mesh which is used to represent the surface geometry of the stamping.

Influence of Grid Shape

An artificial mesh of the kind shown in Figure C.8 is employed to ascertain what effect this might have on the mapping process. This mesh is deliberately created in a way that the elements are equally divided on both sides of the 45 degree line of the hemisphere, i.e. the very last element of each row and column always meet at the vertical plane which bisects the angle XOY. Hence, the corner nodes of the last element in each row/column are always situated on the 45° plane. If the mapping procedure is correct these nodes will remain on the angle bisector in the two dimensional blank. The "correct" analytical map is shown in Figure C.9. The hemispherical shell can now be transformed onto the flat blank using the technique of the area criterion.

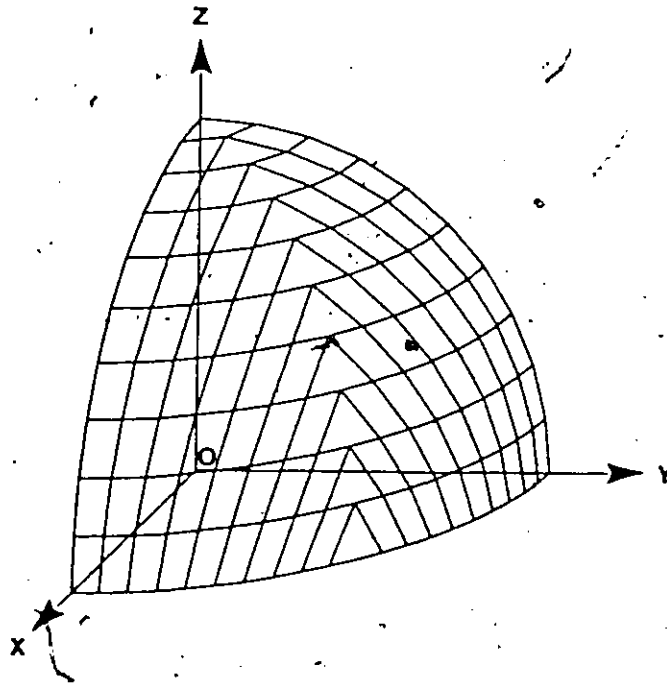


Figure C.8: An artificial mesh as shown is constructed over the surface of the hemisphere.

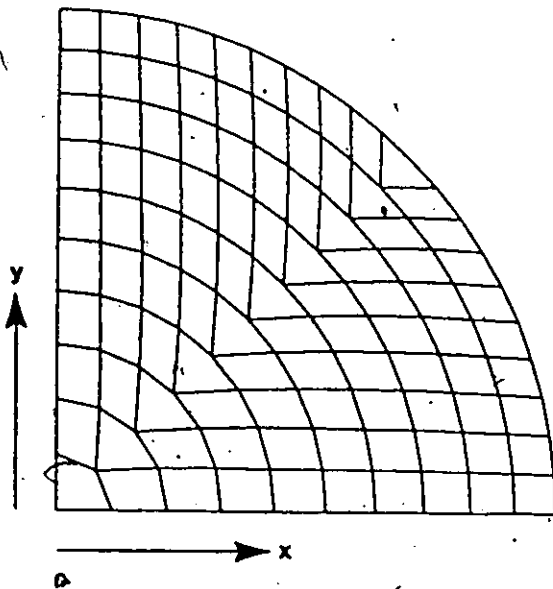


Figure C.9: The "correct" analytical transformation of the mesh in Fig. C.8 on a plane.

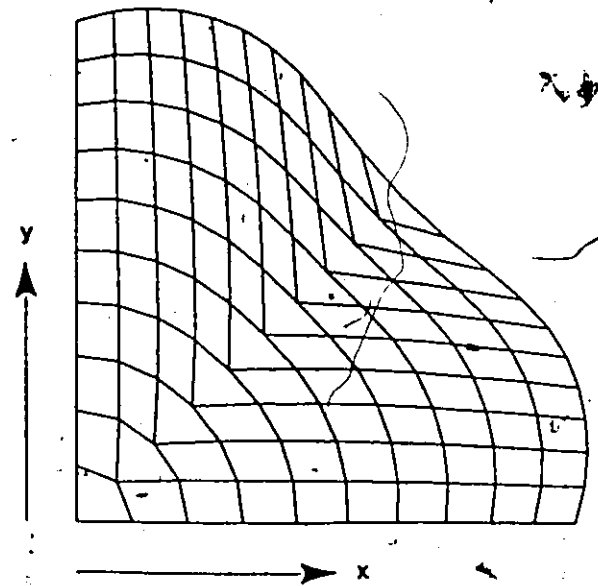


Figure C.10: The resulting map of the surface occurred with the area criterion showing effect of element geometry.

It transpired that the mapping technique is dependent on the shape of the elements used to represent the 3D surface. The result of the mapping is shown in Figure C.10. Note that many of the quadrilateral elements on the 45° line of the 3-D surface are rather ill-conditioned, i.e. two contiguous sides are at such an oblique angle they almost form a straight line. Therefore when these quadrilaterals are sub-divided into triangular elements, one triangle has an exceedingly small surface area. This causes some problems in the mapping process, and as can be seen from Fig. C.10 there is a depression in the mapped shape along the 45° axis. While the mapping has not been very successful with the mesh shown in Fig. C.8, the "test case" of the hemispherical shell has resulted in some valuable conclusions.

It is apparent from the test case that the shape and size of the mesh exerts an influence on the shape of the mapped blank. The effect may be more significant when attempting to represent the surface geometry of a complex stamping. Unless some care is taken when the grid of lines is drawn free hand on the surface of the stamping, some highly irregular shaped quadrilaterals may ensue. Hence they may be ill-conditioned in the manner referred to above, and lead to problems, such as overlapping of elements, in the mapping process. Furthermore since the surface of the stamping is characterised by the nodes of the quadrilaterals, then a rather poor representation of the surface can occur if the mesh is badly drawn. For example, corners, bends, recesses and the like on the stamping can all be eroded depending upon the shape of the mesh. Consequently in regions on the stamping when abrupt

changes in geometry occur, a finer mesh size should be employed to obtain a better representation of the actual surface.

Remapping

The mapping process demonstrated above correlates nodal points between the final part shape and a flat blank. In general the elements on both surfaces are irregular and while the shape of the boundary is clearly indicated, it is not easy to visualize the deformation suffered by each element. For this reason, it is convenient to establish a new mesh which is at least regular in the flat blank. An array of orthogonal lines has been selected and is overlaid on the irregular grid in Figure C.11. Using the displacements established for the irregular grid, the new nodal points corresponding to the regular grid are now mapped onto the polyhedral surface of Fig. C.3 adopting the technique of reverse mapping discussed in Section 3.4.

A new polyhedron is established by facets created by the new nodes and is illustrated in Fig. C.12. It will be appreciated that this surface is a further "erosion" of the initial surface of the real part.

Adjustment

The aforementioned homolographic transformation of surfaces provides the designer with a technique of evaluating the deformation which will be suffered by a sheet formed in the tooling being designed. The solution obtained does not necessarily correspond to the actual deformation and therefore the designer must have further means to modify

the result in hope to achieve a more realistic design.

The adjustment schemes described in Chapter 3 are applied to the blank shape in Fig. C.4 and the results of two different surface modifications are given in Figs. C.13 and C.14. Figure C.13 showing surface adjustment on the blank in a 45° direction with respect to the x-axis while the technique of surface modification applied to a region within the blank shape in Fig. C.4 is demonstrated in Figure C.14. The adjustment generates a new set of nodal displacements which again can be used to perform the remapping process between the adjusted blank and the deformed part. These design procedures can be repeated as many times as it is decided by the die designer. Since the reverse mapping of the new blanks is just another computing exercise hence the remap has not been done here.

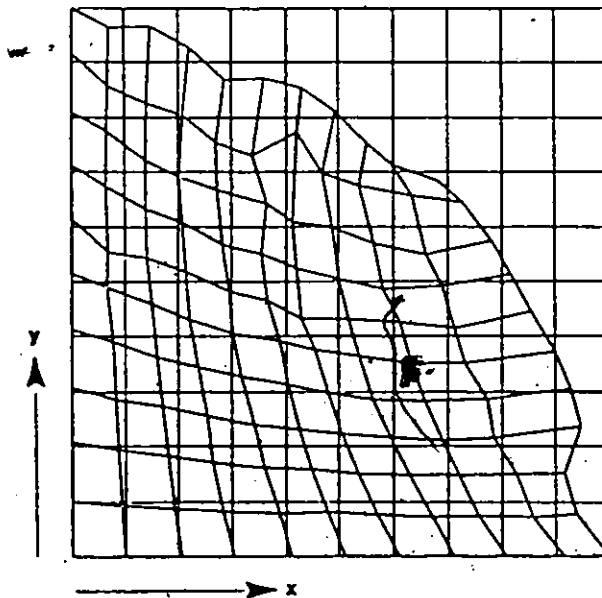


Figure C.11: A regular grid is superimposed on the developed blank shape.

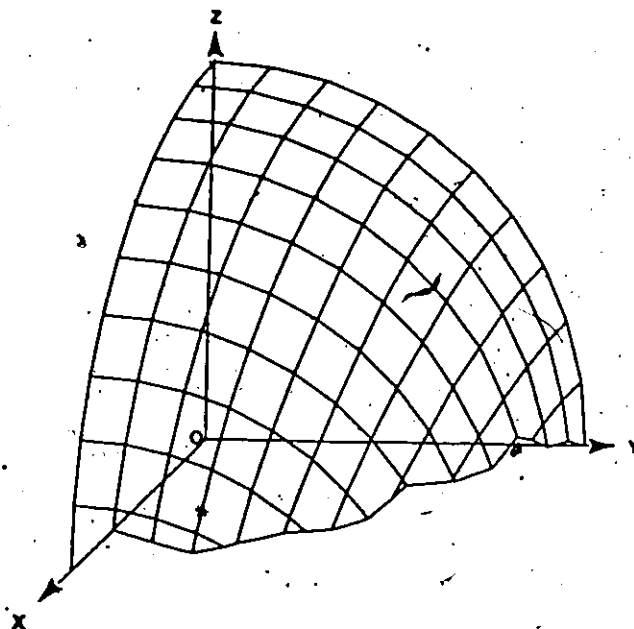


Figure C.12: The resulting polyhedron established on the hemisphere surface using the regular grid in Fig. C.11.

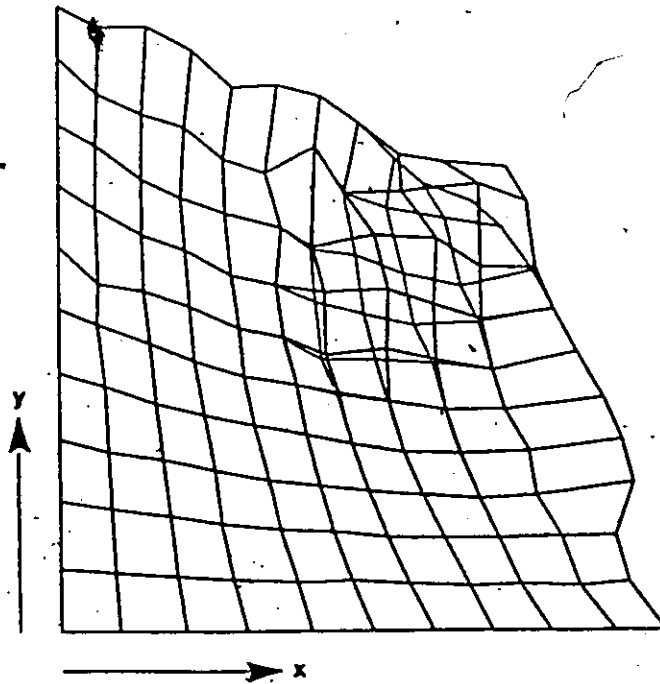


Figure C.13: Diagram showing surface adjustment in a specified direction applied to the blank in Fig. C.4.

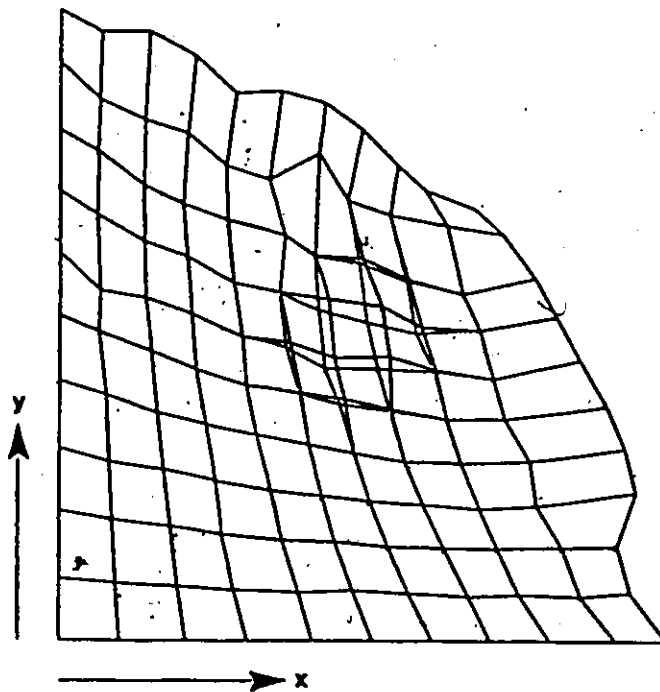


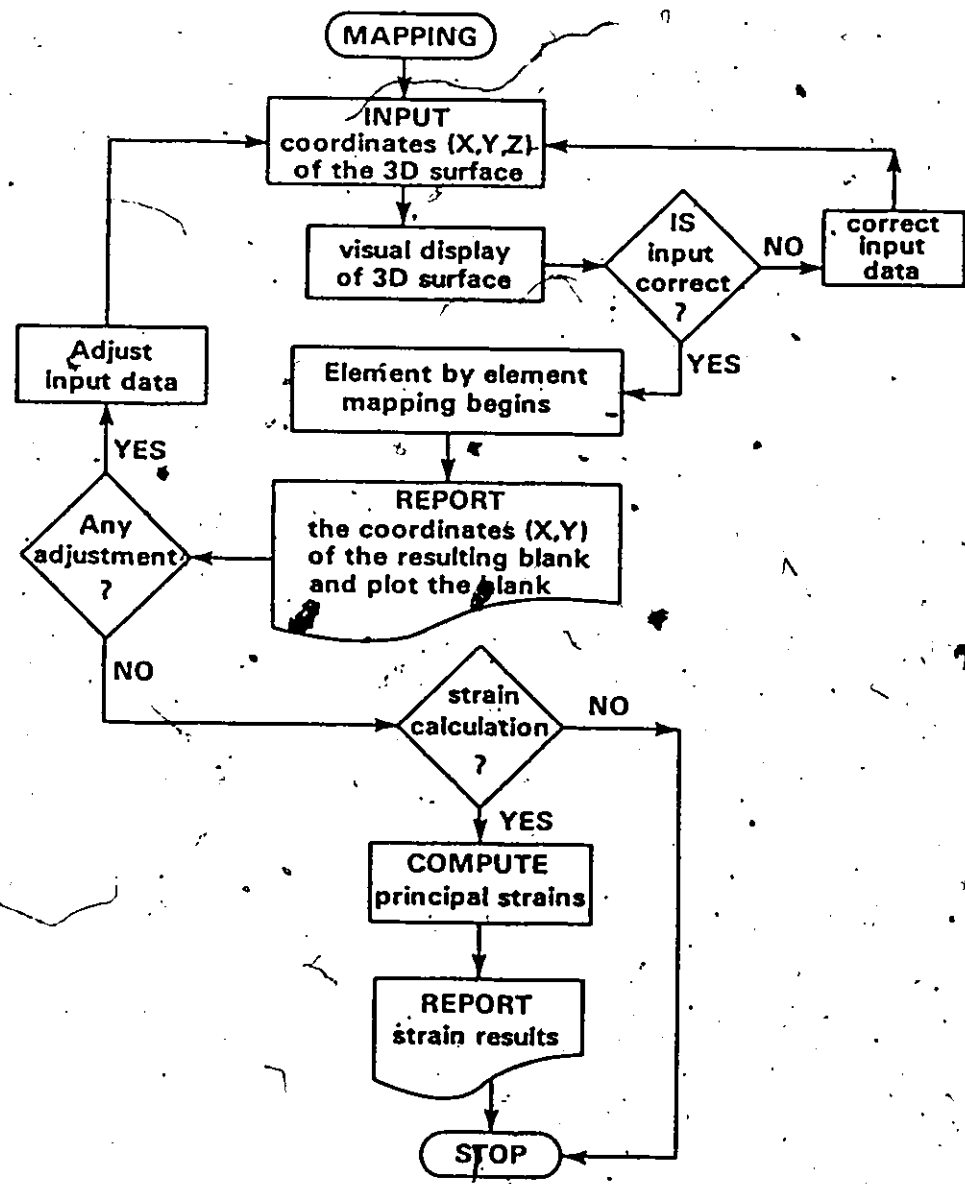
Figure C.14: Diagram showing local distortion of a region within the blank in Fig. C.4.

APPENDIX D

Flow Charts

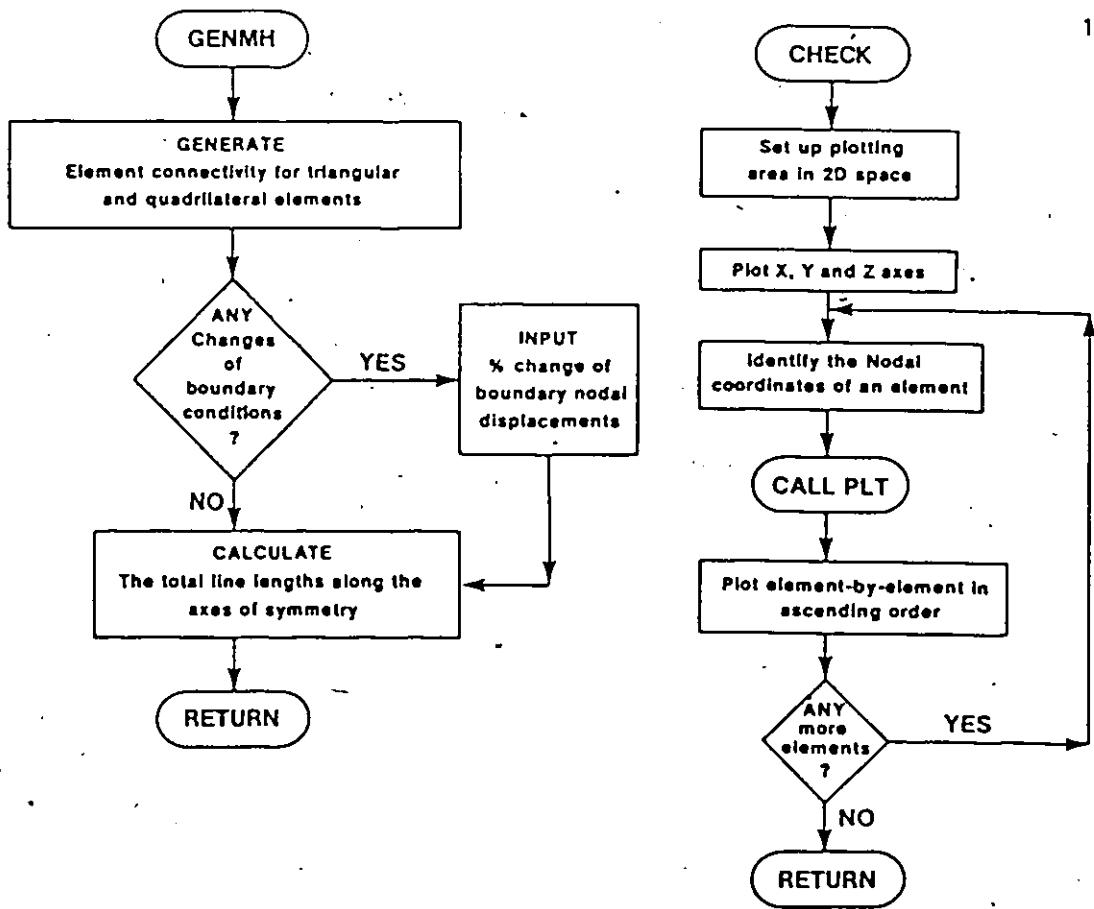
This Appendix describes the philosophy (see Figs. D.1(a) to D.1(g)) of the logical development of a computer-aided die design system based on the theories discussed throughout Chapter 3. The die design package comprises of the following functions:

- (1) visual check - computer plotting of the input surface;
- (2) blank development - performing an element-by-element mapping procedure onto a flat plane using the method of area criterion;
- (3) remapping - performing an element-by-element remapping of a regular grid back on the part surface using known displacements of the nodes generated in (2);
- (4) adjustment - performing a possible modification of a blank surface in hope to achieve a more reasonable design;
- (5) plotting of the resulting blank shape, the resulting remapped grid and the adjusted blank surface;
- (6) strain determination - evaluating the principal strains from the nodal positions of a mesh on the part surface and the resulting mesh on the flat plane or vice versa.

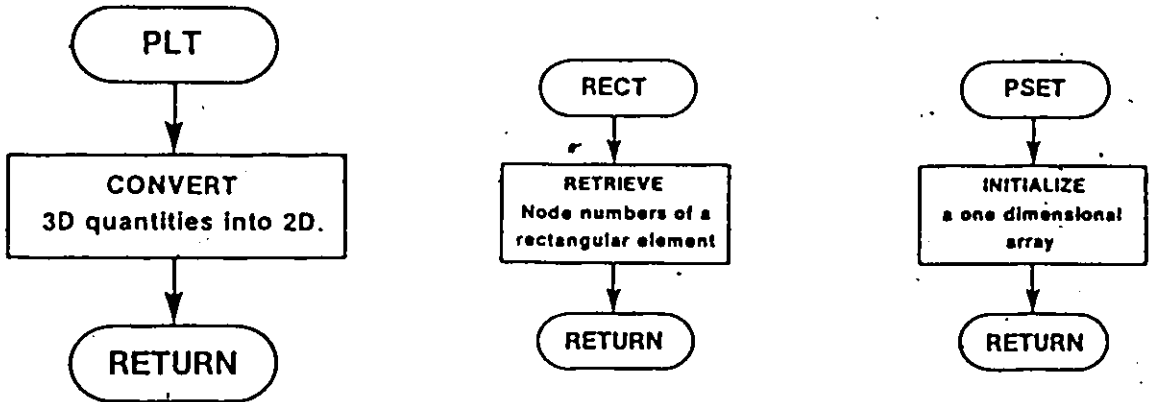


(a)

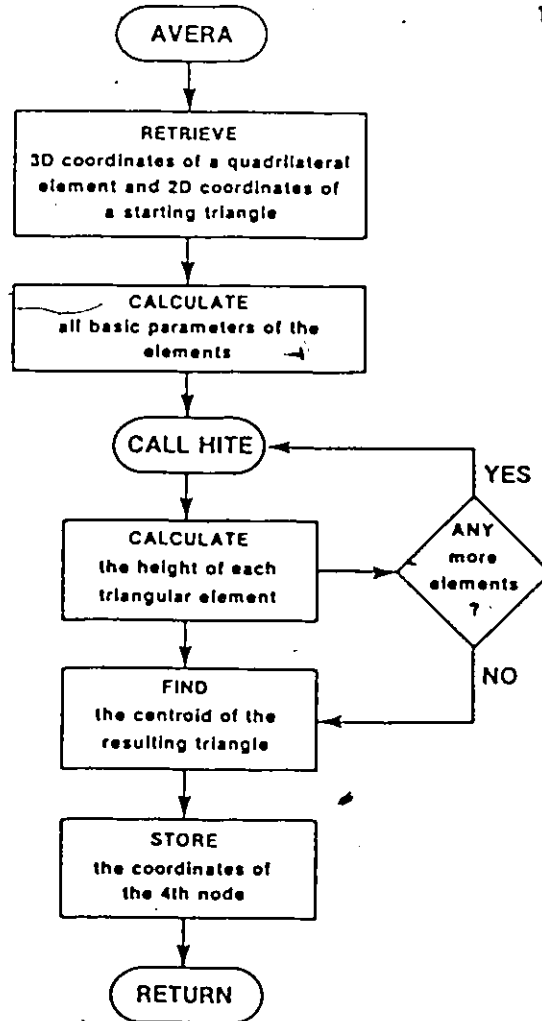
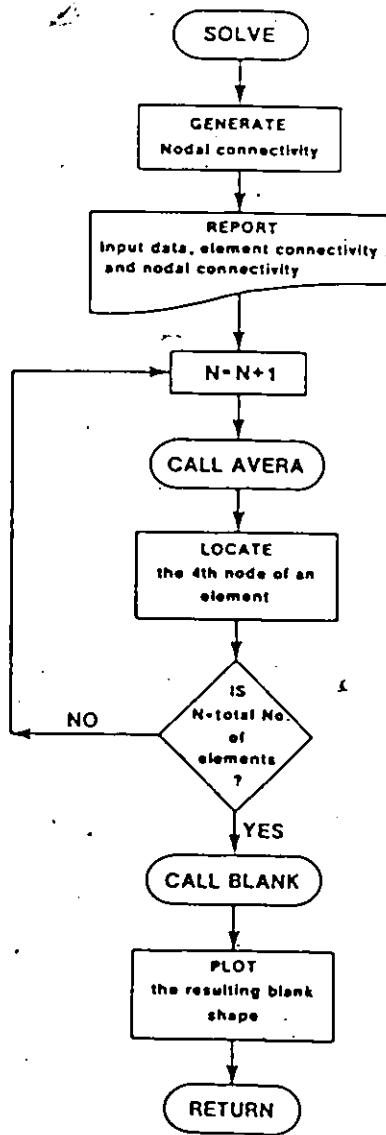
Figure D.1: (a)-(g): Flow charts indicating the complete logical development of the mapping strategy.



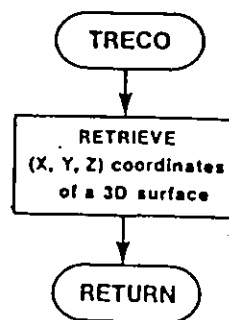
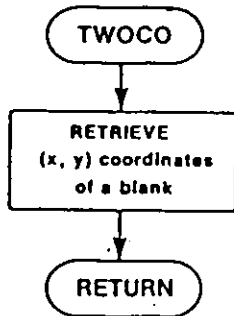
(b)



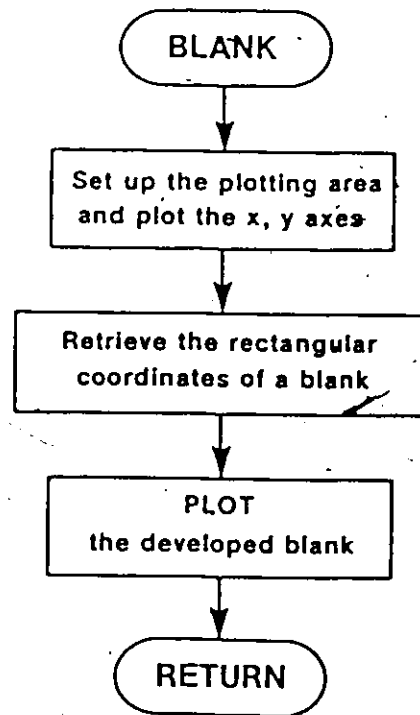
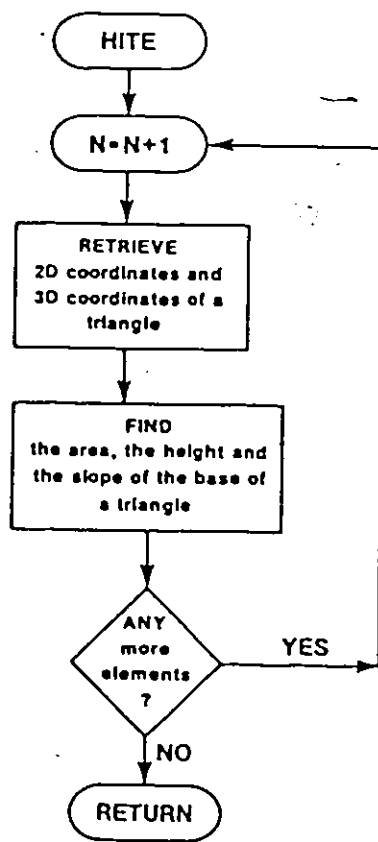
(c)



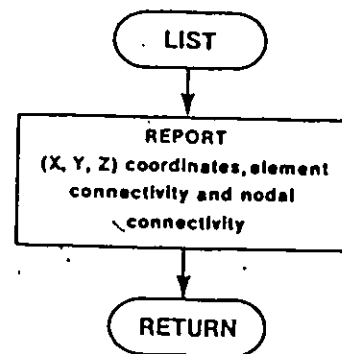
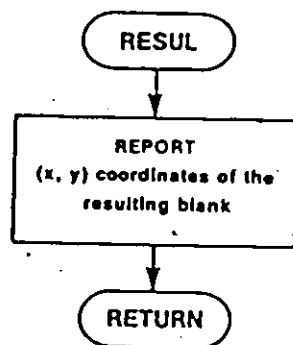
(d)



(e)



(f)



(g)

APPENDIX E

List of Subprograms

Mapping: Blank development

- MAIN PROGRAM - to activate the use of the mapping subroutine and to establish the needed input storage dimensions for each principal variable.
- SUBROUTINE MAPPIN - to input sets of orthogonal coordinates, X, Y and Z of a formed part. To generate and calculate the basic required storage for each principal variable.
- SUBROUTINE GENMH - to generate node numbers, element numbers, element connectivity and to set up the position of boundary nodes on a two-dimensional XOY plane.
- SUBROUTINE CHECK - to check input data by plotting the geometry of a deformed part graphically in 3D space using the Versatec 1200A plotter.
- SUBROUTINE SOLVE - to evaluate the nodal connectivity of a mesh and to organize data for sequential mapping.
- SUBROUTINE LIST - to print the coordinates (X,Y,Z) of the input surface. To print results of the calculated nodal connectivity and element connectivity.
- SUBROUTINE AVERA - to perform an element-by-element mapping procedure in order to develop the required blank shape. This routine is implemented based on the method of area

orientations.

SUBROUTINE ST02 - to store the centroidal principal strains and their orientations of triangular elements.

SUBROUTINE PSTRN - to output results of principal nodal strains and principal element strains.

Remapping: Remapping of blank development

PROGRAM REMAP1 - to generate the three dimensional coordinates on a stamped panel of a regular array of nodal points on the flat blank. To read in the 3D coordinates of the deformed surface, the 2D coordinates of the blank developed by the mapping and the 2D coordinates of a regular mesh superimposed on this blank.

SUBROUTINE DETQIN - to determine if a regular grid point $Q(X,Y)$ is within a quadrilateral.

SUBROUTINE DETTIN - to determine which triangle of the quadrilateral obtained in DETQIN the regular grid point $Q(X,Y)$ lies.

SUBROUTINE PT3D - to compute the coordinates of a 3D remapped point.

Finite Strain Evaluation

PROGRAM STRN - to access strain distributions on the surface of a stamping by measurements made of the deformed square grids, to input the deformed surface and to

output the resulting principal strains.

SUBROUTINE GENCON - to compute the basic storage required for each principal variable and to initialize all variable arrays. To produce a 3D plot of the input stamping, to generate element connectivity and nodal connectivity.

SUBROUTINE EFAC - to set up a local reference coordinate axis for strain determinations.

SUBROUTINE EVAL - to evaluate the coefficients of deformation tensor F , the components of the deformation gradient tensor C , the principal stretches and their orientations.

Plotting of the Strain Contours

SUBROUTINE CONTOUR - to input the coordinates (X,Y) of the resulting blank and strain values of each node. To identify the location of a required contour and its position stored in an array for plotting purposes.

SUBROUTINE INTERP - to generate smoother contours from the positions of the defined contours using a cubic function.

SUBROUTINE SPLINE - to perform a spline interpolation of the data points in order to compute intermediate values between two points.

SUBROUTINE SPLIT - to determine the second derivatives of the spline fit.

SUBROUTINE SOLN - to solve a system of simultaneous equation.

APPENDIX F

Strain Ellipsoids

Lagrangian Strain Ellipsoid

If the total deformation is characterized by an unsymmetric deformation gradient \underline{F} , then the theorem of polar decomposition, expresses that

$$\underline{F} = \underline{R} \cdot \underline{U} = \underline{V} \cdot \underline{R} \quad (\text{F.1})$$

or

$$\underline{U} = \underline{R}^T \cdot \underline{F} \quad \text{and} \quad \underline{V} = \underline{F} \cdot \underline{R}^T \quad (\text{F.2})$$

If (F.2) is expressed in matrix form, then from (4.17) the components of the right stretch tensor, \underline{U} , in the 2-3 plane can be obtained as

$$\begin{bmatrix} U_{22} & U_{23} \\ U_{32} & U_{33} \end{bmatrix} = \begin{bmatrix} \cos\theta & \sin\theta \\ -\sin\theta & \cos\theta \end{bmatrix} \begin{bmatrix} F_{22} & F_{23} \\ F_{32} & F_{33} \end{bmatrix} \quad (\text{F.2})$$

Hence

$$\begin{aligned} U_{22} &= F_{22} \cos\theta + F_{32} \sin\theta \\ U_{23} &= F_{23} \cos\theta + F_{33} \sin\theta \\ U_{32} &= F_{32} \cos\theta - F_{22} \sin\theta \\ U_{33} &= F_{33} \cos\theta - F_{23} \sin\theta \end{aligned} \quad (\text{F.3})$$

Since the tensor, \underline{U} is symmetric, then from (F.3) $U_{12} = U_{21}$ it follows that

$$\tan\theta = \frac{F_{32} - F_{23}}{F_{22} + F_{33}} \quad (\text{F.4})$$

Furthermore

$$\cos\theta = \frac{F_{22} + F_{33}}{\sqrt{(F_{22} + F_{33})^2 + (F_{32} - F_{23})^2}} \quad (\text{F.5a})$$

and

$$\sin \theta = \frac{F_{32} - F_{23}}{\sqrt{(F_{22} + F_{33})^2 + (F_{32} - F_{23})^2}} \quad (\text{F.5b})$$

The orientation of the principal axes of the Lagrangian ellipsoid is obtained, after combining (F.3) and (F.5), as

$$\tan 2\phi_L = \frac{2U_{23}}{U_{22} - U_{33}} = \frac{2(F_{33}F_{32} + F_{22}F_{23})}{(F_{22}^2 - F_{33}^2) + (F_{32}^2 - F_{23}^2)} \quad (\text{F.6})$$

Eulerian Strain Ellipsoid

The orientation of the principal axes with respect to the current configuration is derived in a similar fashion to the above. The starting point

$$\underline{V} = \underline{E} \cdot \underline{R}^T,$$

and the steps leading to an equation like (F.3) are duplicated. The orientation of the Eulerian ellipsoid is given as

$$\tan 2\phi_E = \frac{2V_{23}}{V_{22} - V_{33}} = \frac{2(F_{22}F_{32} + F_{33}F_{23})}{(F_{22}^2 - F_{33}^2) - (F_{32}^2 - F_{23}^2)} \quad (\text{F.7})$$

The orientation of the Lagrangian or Eulerian ellipsoid can be determined precisely from Equations (F.6) and (F.7) respectively. Hill [25] has considered the rotation of the Lagrangian and Eulerian strain ellipsoids due to an infinitesimal deformation step superimposed on a large prior homogeneous deformation. The total deformation gradient tensor \underline{E} is characterized by Equation (4.38) as

$$\underline{E} = d\underline{n} \cdot \underline{\lambda} = \begin{pmatrix} \lambda_2 & \lambda_3 d n_{23} \\ \lambda_2 d n_{32} & \lambda_3 \end{pmatrix} \quad (\text{F.8})$$

Hill, op cit, argued that for a small perturbation superimposed on the large deformation the angle of rotation incurred is small and that to a first order approximation, the second order quantity $(F_{32}^2 - F_{23}^2)$ is ignored. It follows from (F.6) and (F.8) that the rotation of the principal axes of the Lagrangian ellipsoid is

$$\delta\phi_L = \frac{(2\lambda_2\lambda_3)}{\lambda_2^2 - \lambda_3^2} d\eta_{23}, \quad (\text{F.9})$$

and similarly the rotation of the Eulerian strain ellipsoid is

$$\delta\phi_E = \frac{\lambda_2^2 + \lambda_3^2}{\lambda_2^2 - \lambda_3^2} d\eta_{23}. \quad (\text{F.10})$$

The rigid body rotation is calculated from (F.4) as

$$\delta\theta = \frac{\lambda_2 - \lambda_3}{\lambda_2 + \lambda_3} d\eta_{23}. \quad (\text{F.11})$$

Equations (F.9) to (F.11) are identical to the results obtained by Hill [25,26]

Strain Measures

A relationship between the time derivative of $\ln \underline{U}$ and the rate of deformation tensor \underline{D} can be developed by the following procedures.

From Equation (4.8) the time derivative of $\ln \underline{U}$ is

$$(\ln \underline{U})^{\cdot} = \dot{\underline{P}} \cdot \ln \underline{\lambda} \cdot \underline{P}^T + \underline{P} \cdot (\ln \underline{\lambda})^{\cdot} \cdot \underline{P}^T + \underline{P} \cdot \ln \underline{\lambda} \cdot \dot{\underline{P}}^T \quad (\text{F.12})$$

Since the tensor \underline{P} is an orthogonal tensor such that

$$\underline{P} \cdot \underline{P}^T = \underline{1} \quad \text{and} \quad \dot{\underline{P}} \cdot \underline{P}^T + \underline{P} \cdot \dot{\underline{P}}^T = \underline{0}, \quad (\text{F.13})$$

then using the relation $\ln \underline{U} = \underline{P} \cdot \ln \underline{\lambda} \cdot \underline{P}^T$ equation (F.12) becomes

$$(\ln \underline{U})^{\cdot} = \dot{\underline{P}} \cdot \underline{P}^T \cdot \ln \underline{U} - \ln \underline{U} \cdot \dot{\underline{P}} \cdot \underline{P}^T + \underline{P} \cdot \underline{\lambda} \cdot \underline{\lambda}^{-1} \cdot \dot{\underline{P}}^T. \quad (\text{F.14})$$

Hence

$$\underline{P} \cdot \underline{\lambda} \cdot \underline{\lambda}^{-1} \cdot \underline{P}^T = (\dot{\ln} \underline{U})^{\circ} + \dot{\ln} \underline{U} \cdot \underline{\dot{P}} \cdot \underline{P}^T - \underline{\dot{P}} \cdot \underline{P}^T \cdot \dot{\ln} \underline{U} \quad (\text{F.15})$$

or

$$\underline{P} \cdot \underline{\lambda} \cdot \underline{\lambda}^{-1} \cdot \underline{P}^T = (\dot{\ln} \underline{U})^{\circ}, \quad (\text{F.16})$$

where

$$(\dot{\ln} \underline{U})^{\circ} = (\dot{\ln} \underline{U})^{\circ} + \dot{\ln} \underline{U} \cdot \underline{\dot{P}} \cdot \underline{P}^T - \underline{\dot{P}} \cdot \underline{P}^T \cdot \dot{\ln} \underline{U}$$

is the co-rotational rate of $(\dot{\ln} \underline{U})$ relative to the principal axes of \underline{U} .

In view of (F.16) and the time rate of $\underline{U} = \underline{P} \cdot \underline{\lambda} \cdot \underline{P}^T$, it can be shown that

$$\dot{\underline{U}} \cdot \underline{U}^{-1} = (\dot{\ln} \underline{U})^{\circ} + \underline{\dot{P}} \cdot \underline{P}^T - \underline{U} \cdot \underline{\dot{P}} \cdot \underline{P}^T \cdot \underline{U}^{-1}, \quad (\text{F.17})$$

and

$$\underline{U}^{-1} \cdot \dot{\underline{U}} = (\dot{\ln} \underline{U})^{\circ} - \underline{\dot{P}} \cdot \underline{P}^T + \underline{U}^{-1} \cdot \underline{\dot{P}} \cdot \underline{P}^T \cdot \underline{U}. \quad (\text{F.18})$$

It follows from equation (4.49) that

$$\underline{D} = \frac{1}{2} \underline{R} \cdot (\dot{\underline{U}} \cdot \underline{U}^{-1} + \underline{U}^{-1} \cdot \dot{\underline{U}}) \cdot \underline{R}^T, \quad (\text{F.19})$$

upon substituting (F.17) and (F.18) into the above equation, it follows that

$$\underline{D} = \underline{R} \cdot (\dot{\ln} \underline{U})^{\circ} \cdot \underline{R}^T - \frac{1}{2} (\underline{F} \cdot \underline{\dot{P}} \cdot \underline{P}^T \cdot \underline{F}^{-1} - \underline{F}^{-T} \cdot \underline{\dot{P}} \cdot \underline{P}^T \cdot \underline{F}^T). \quad (\text{F.20})$$

The spin tensor which is defined as

$$\underline{W} = \frac{1}{2} \underline{R} \cdot (\dot{\underline{U}} \cdot \underline{U}^{-1} - \underline{U}^{-1} \cdot \dot{\underline{U}}) \cdot \underline{R}^T + \underline{\dot{R}} \cdot \underline{R}^T, \quad (\text{F.21})$$

and upon combining with (F.17) and (F.18) results in

$$\underline{W} = \underline{\dot{R}} \cdot \underline{R}^T + \underline{R} \cdot \underline{\dot{P}} \cdot \underline{P}^T \cdot \underline{R}^T - \frac{1}{2} (\underline{F} \cdot \underline{\dot{P}} \cdot \underline{P}^T \cdot \underline{F}^{-1} + \underline{F}^{-T} \cdot \underline{\dot{P}} \cdot \underline{P}^T \cdot \underline{F}^T) \quad (\text{F.22})$$

Hence the velocity gradient \underline{L} can be calculated as

$$\begin{aligned} \underline{L} &= \underline{D} + \underline{W} \\ &= \underline{R} \cdot (\dot{\ln} \underline{U})^{\circ} \cdot \underline{R}^T + \underline{\dot{R}} \cdot \underline{R}^T + \underline{R} \cdot \underline{\dot{P}} \cdot \underline{P}^T \cdot \underline{R}^T - \underline{F} \cdot \underline{\dot{P}} \cdot \underline{P}^T \cdot \underline{F}^{-1} \end{aligned} \quad (\text{F.23})$$

Hill [26] treats the rotation of the Lagrangian ellipsoid about

its own axes for the special case where they coincide with the frame of reference. Consequently

$$\underline{\underline{P}} = \underline{\underline{1}} \text{ and } \ln \underline{\underline{U}} = \ln \underline{\underline{\lambda}}$$

therefore equation (F.14) reduces to

$$(\ln \underline{\underline{\lambda}})^{\circ} = \dot{\underline{\underline{P}}} \cdot \underline{\underline{P}}^T \cdot \ln \underline{\underline{\lambda}} - \ln \underline{\underline{\lambda}} \cdot \dot{\underline{\underline{P}}} \cdot \underline{\underline{P}}^T + \dot{\underline{\underline{\lambda}}} \cdot \underline{\underline{\lambda}}^{-1} \quad (\text{F.24})$$

Since the spin of the Lagrangian triad is evaluated from

$$\dot{\underline{\underline{P}}} \cdot \underline{\underline{P}}^T = \dot{\phi}_L \begin{bmatrix} 0 & -1 \\ 1 & 0 \end{bmatrix} \quad (\text{F.25})$$

upon substituting (F.25) into (F.24), gives

$$\begin{aligned} (\ln \underline{\underline{\lambda}})^{\circ} &= \dot{\phi}_L \begin{bmatrix} 0 & -1 \\ 1 & 0 \end{bmatrix} \begin{bmatrix} \ln \lambda_2 & 0 \\ 0 & \ln \lambda_3 \end{bmatrix} - \begin{bmatrix} \ln \lambda_2 & 0 \\ 0 & \ln \lambda_3 \end{bmatrix} \begin{bmatrix} 0 & -1 \\ 1 & 0 \end{bmatrix} \dot{\phi}_L + \begin{bmatrix} \dot{\lambda}_2 \lambda_2^{-1} & 0 \\ 0 & \dot{\lambda}_3 \lambda_3^{-1} \end{bmatrix} \\ &= \begin{bmatrix} 0 & -\ln \lambda_3 \\ \ln \lambda_2 & 0 \end{bmatrix} \dot{\phi}_L - \begin{bmatrix} 0 & -\ln \lambda_2 \\ \ln \lambda_3 & 0 \end{bmatrix} \dot{\phi}_L + \begin{bmatrix} \dot{\lambda}_2 \lambda_2^{-1} & 0 \\ 0 & \dot{\lambda}_3 \lambda_3^{-1} \end{bmatrix} \\ &= \begin{pmatrix} \dot{\lambda}_2 / \lambda_2 & (\ln \lambda_2 / \lambda_3) \dot{\phi}_L \\ (\ln \lambda_2 / \lambda_3) \dot{\phi}_L & \dot{\lambda}_3 / \lambda_3 \end{pmatrix} \end{aligned}$$

$$\text{where } \dot{\phi}_L = \frac{2\lambda_2 \dot{\lambda}_3}{\lambda_2^2 - \lambda_3^2} \epsilon_{23}$$

Stress Rates

In order to obtain an objective stress rate, we define a tensor quantity $\underline{\underline{\psi}}$ such that

$$\underline{\underline{D}} = \underline{\underline{R}} \cdot \underline{\underline{\psi}} \cdot \underline{\underline{R}}^T \quad (\text{F.26})$$

$$\text{where } \underline{\underline{\psi}} = (\ln \underline{\underline{U}})^{\circ} - \text{sym}(\underline{\underline{U}} \cdot \dot{\underline{\underline{P}}} \cdot \underline{\underline{P}}^T \cdot \underline{\underline{U}}^{-1})$$

Employing the equation of the rate of work done per unit current volume,

we have

$$\dot{\underline{w}} = \underline{\tau} : \underline{D} = \underline{\tau} : (\underline{R} \cdot \underline{\psi} \cdot \underline{R}^T). \quad (\text{F.27})$$

In view of the second order tensor transform

$$\underline{A} : \underline{B} = (\underline{A}^T \cdot \underline{B}) : \underline{1} = (\underline{A} \cdot \underline{B}^T) : \underline{1}, \quad (\text{F.28})$$

it can be shown that

$$\begin{aligned} \dot{\underline{w}} &= [\underline{\tau}^T \cdot (\underline{R} \cdot \underline{\psi} \cdot \underline{R}^T)] : \underline{1} \\ &= (\underline{\tau}^T \cdot \underline{R} \cdot \underline{\psi}) : \underline{R} \\ &= \underline{R} : (\underline{\tau}^T \cdot \underline{R} \cdot \underline{\psi}) \\ &= [(\underline{R}^T \cdot \underline{\tau}^T \cdot \underline{R}) \cdot \underline{\psi}] : \underline{1} \\ &= (\underline{R}^T \cdot \underline{\tau} \cdot \underline{R}) : \underline{\psi}. \end{aligned} \quad (\text{F.29})$$

The first term on the right side of equation (F.29) can be regarded as a pseudo stress tensor, say $\underline{\tau}_R$, such that

$$\dot{\underline{w}} = \underline{\tau} : \underline{D} = \underline{\tau}_R : \underline{\psi}$$

and

$$\underline{\tau}_R = \underline{R}^T \cdot \underline{\tau} \cdot \underline{R}. \quad (\text{F.30})$$

The time derivative of (F.30) gives

$$\begin{aligned} \dot{\underline{\tau}}_R &= \underline{R}^T \cdot \dot{\underline{\tau}} \cdot \underline{R} + \dot{\underline{R}}^T \cdot \underline{\tau} \cdot \underline{R} + \underline{R}^T \cdot \underline{\tau} \cdot \dot{\underline{R}} \\ &= \underline{R}^T \cdot [\dot{\underline{\tau}} + \underline{R} \cdot \dot{\underline{R}}^T \cdot \underline{\tau} + \underline{\tau} \cdot \dot{\underline{R}} \cdot \underline{R}^T] \cdot \underline{R} \\ &= \underline{R}^T \cdot [\dot{\underline{\tau}} + \underline{\tau} \cdot \dot{\underline{R}} \cdot \underline{R}^T - \dot{\underline{R}} \cdot \underline{R}^T \cdot \underline{\tau}] \cdot \underline{R} \end{aligned}$$

The rate of rotation of the material $\underline{\Omega} = \dot{\underline{R}} \cdot \underline{R}^T$ is skew symmetric and therefore $\underline{\Omega} + \underline{\Omega}^T = \underline{0}$. We can then define a co-rotational stress rate $\underline{\overset{\nabla}{\tau}}$,

where

$$\underline{\overset{\nabla}{\tau}} = \dot{\underline{\tau}} + \underline{\tau} \cdot \underline{\Omega} - \underline{\Omega} \cdot \underline{\tau}. \quad (\text{F.31})$$

Stress Rates in Simple Shear

From equation (4.106) the constitutive equation of a hypoelastic material has the form

$$\dot{\underline{\underline{\sigma}}} = \lambda \text{trace}(\underline{\underline{D}}) \underline{\underline{1}} + 2\mu \underline{\underline{D}} \quad (\text{F.32})$$

where the Lamé constants are defined as

$$\lambda = \frac{E\nu}{(1+\nu)(1-2\nu)} \quad \text{and} \quad \mu = \frac{E}{2(1+\nu)}$$

In the above expressions E is Young's modulus and ν Poisson's ratio. Upon expanding (F.32), the stress rate of an hypoelastic material becomes

$$\dot{\underline{\underline{\sigma}}} = \begin{bmatrix} (\lambda+2\mu)D_{11} & 2\mu D_{12} \\ 2\mu D_{21} & (\lambda+2\mu)D_{22} \end{bmatrix} \quad (\text{F.33})$$

Upon combining the above with the matrix of the deformation gradient tensor $\underline{\underline{D}}$ given in equation (4.104) yields

$$\dot{\underline{\underline{\sigma}}} = \begin{pmatrix} 0 & \mu \dot{s} \\ \mu \dot{s} & 0 \end{pmatrix} \quad (\text{F.34})$$

When the rate type equations described in Chapter 4 are expanded we obtain,

$$\dot{\underline{\underline{\sigma}}} = \dot{\underline{\underline{\sigma}}} + \underline{\underline{\sigma}} \cdot \underline{\underline{\Omega}} - \underline{\underline{\Omega}} \cdot \underline{\underline{\sigma}}$$

$$= \begin{pmatrix} \dot{\sigma}_{11} + \sigma_{12} \Omega_{21} - \sigma_{12} \Omega_{12} & \dot{\sigma}_{12} + \sigma_{11} \Omega_{12} + \sigma_{22} \Omega_{22} - \sigma_{11} \Omega_{22} - \sigma_{22} \Omega_{11} \\ \dot{\sigma}_{21} + \sigma_{12} \Omega_{11} + \sigma_{22} \Omega_{21} - \sigma_{11} \Omega_{21} - \sigma_{22} \Omega_{22} & \dot{\sigma}_{22} + \sigma_{12} \Omega_{12} - \sigma_{12} \Omega_{21} \end{pmatrix}$$

In view of equations (4.93) and (4.94) it can be seen that $\Omega_{11} = \Omega_{22} = 0$ and $\Omega_{21} = -\Omega_{12}$. After combining with (F.33), the above expression reduces to

$$\begin{aligned}
 \dot{\theta}_{11} &= \dot{\sigma}_{11} - 2\dot{\Omega}_{12}\sigma_{21} = 0 \\
 \dot{\theta}_{12} &= \dot{\sigma}_{12} + \dot{\Omega}_{12}\sigma_{11} - \dot{\Omega}_{12}'\sigma_{22} = 2\mu\dot{D}_{12} \\
 \dot{\theta}_{22} &= \dot{\sigma}_{22} + 2\dot{\Omega}_{12}\sigma_{12} = 2\mu\dot{D}_{22} = 0
 \end{aligned} \tag{F.35}$$

Upon applying (F.34) and (4.94), equation (F.35) becomes a set of simultaneous equations of the form

$$\begin{aligned}
 \dot{\sigma}_{11} - 2\dot{\theta}\sigma_{12} &= 0 \\
 \dot{\sigma}_{12} + 2\dot{\theta}\sigma_{11} &= \mu\dot{S} \\
 \dot{\sigma}_{22} + 2\dot{\theta}\sigma_{12} &= 0
 \end{aligned} \tag{F.36}$$

Differentiating (F.36a) twice with respect to time yields

$$\ddot{\sigma}_{11} - 2\ddot{\theta}\sigma_{12} - 2\dot{\theta}\dot{\sigma}_{12} = 0.$$

When this expression is combined with the equations (F.36a) and (F.36b) the following ordinary differential equation is obtained

$$\ddot{\sigma}_{11} - \frac{\ddot{\theta}}{\dot{\theta}}\dot{\sigma}_{11} + 4\dot{\theta}^2\sigma_{11} = 2\mu\dot{\theta}\dot{S}. \tag{F.37}$$

From equations (4.98) and (4.99), with $\ddot{S} = 0$, there results

$$2\mu\dot{\theta}\dot{S} = 4\mu\dot{\theta}^2 \sec^2\theta$$

and

$$\frac{\ddot{\theta}}{\dot{\theta}} = -2\tan\theta \dot{\theta}.$$

Hence (F.37) reduces to

$$\frac{d^2\sigma_{11}}{d\theta^2} + \frac{d\sigma_{11}}{d\theta} 2\tan\theta + 4\sigma_{11} = 4\mu\sec^2\theta, \tag{F.38}$$

which has to be solved numerically.

Finally combining the stress rate proposed in Chapter 4, i.e. equation (4.109) with (F.32) and repeating the procedures described above, an ordinary differential equation similar to that of (F.37) is

obtained, in particular

$$\ddot{\sigma}_{11} - \frac{\dot{\phi}}{\phi} \dot{\sigma}_{11} + 4\dot{\phi}^2 \sigma_{11} = 2\mu\dot{\phi}\dot{S} \quad (\text{F.39})$$

After differentiating equation (4.96) and (4.97) with respect to time and rearranging terms, one obtains respectively

$$\dot{S} = 4\text{cosec}^2 2\phi_L \dot{\phi}_L \quad (\text{F.40})$$

and

$$\dot{S} = -4\text{cosec}^2 2\phi_E \dot{\phi}_E \quad (\text{F.41})$$

The time derivative of (F.40) with $\dot{S} = 0$ yields

$$\ddot{\phi}_L = 4\cot 2\phi_L \dot{\phi}_L^2 \quad (\text{F.42})$$

or

$$\frac{\ddot{\phi}_L}{\dot{\phi}_L} = 4\cot 2\phi_L \dot{\phi}_L \quad (\text{F.43})$$

Similarly from equation (F.41), it follows that

$$\frac{\ddot{\phi}_E}{\dot{\phi}_E} = 4\cot 2\phi_E \dot{\phi}_E \quad (\text{F.44})$$

In view of equations (F.40) and (F.43), the equation (F.39) can be expressed in terms of the spin of the Lagrangian ellipse. Hence

$$\frac{d^2 \sigma_{11}}{d\phi_L^2} - \frac{d\sigma_{11}}{d\phi_L} 4\cot 2\phi_L + 4\sigma_{11} = 8\mu\text{cosec}^2 2\phi_L \quad (\text{F.45})$$

Similarly adopting the spin of the Eulerian strain ellipsoid (F.39) becomes

$$\frac{d^2\sigma_{11}}{d\phi_E^2} - \frac{d\sigma_{11}}{d\phi_E} 4\cot 2\phi_E + 4\sigma_{11} = -8\mu\csc^2 2\phi_E \quad (\text{F.46})$$

Equations (F.45) and (F.46) have been solved numerically and the results are given in Chapter 4.

References

- [1] Duncan, J.L. and Altan, T., CIRP Annals, 29, 1, 153 (1980).
- [2] Biot, M.A., "Mechanics of Incremental Deformations", New York: John Wiley and Sons (1965).
- [3] Malvern, L.E., "Introduction to the Mechanics of a Continuous Medium", New Jersey: Prentice-Hall (1969).
- [4] Gurtin, M.E., "An Introduction to Continuous Mechanics", New York: Academic (1981).
- [5] Sowerby, R., Chu, E. and Duncan, J.L., J. Strain Analysis, 17, 95 (1982).
- [6] Sowerby, R. and Chakravarti, P.C., J. Strain Analysis, 18, 119 (1983).
- [7] Sowerby, R., "The Analysis of Finite, Homogeneous Deformation", Engineering Report, McMaster University, Hamilton, Ontario, Canada (1982).
- [8] Bredendick, F., Die Technik, 4, 247 (1969).
- [9] Chu, E., "Finite Strain Evaluation in Metal Forming: A User's Manual", Metal Forming Research Report 82-006, August (1982).
- [10] Keeler, S.P., Sheet Metal Ind., 48, 511 (1971).
- [11] Chu, E., Dung, N.L., Duncan, J.L., and Sowerby, R., Proc. 2nd Canadian CAD/CAM & Robotics Conference and Exposition (1983).
- [12] McCormick, H.O., CAD/CAM for Automotive Design, SME Technical Paper, MS77-768 (1978).
- [13] Davies, C.M. and Moore, G.G., Sheet Metal Industries, 59, 8, 628 (1982).
- [14] Tang, S., Chu, E. and Samanta, S.K., in Numerical Methods in Industrial Forming Processes, p. 629, J.F.T. Pitman, R.D. Wood, J.M. Alexander and O.C. Zienkiewicz, Eds., Pineridge Press, Swansea, U.K. (1982).
- [15] Duncan, J.L. and Sowerby, R., Annals CIRP, 30, 541 (1981).

- [16] Metals Handbook, 8th Ed., Vol. 4, "Forming" Published by American Society for Metals, p. 193 (1979).
- [17] Soldaat, R.J. and Chu, E., Remapping - Part I. Description of the basic interpolation method, Metal Forming Research Report 82-008, Department of Mechanical Engineering, McMaster University, 1982.
- [18] Soldaat, R.J., and Chu, E., Remapping - Part II. Description of the difficulties encountered in the computer program, Metal Forming Research Report 82-013, Department of Mechanical Engineering, McMaster University, 1983.
- [19] Duncan, J.P. and Vickers, G.W., Interactive adjustment of surfaces, Int. J. Mech. Sci., 20, 1, 1(1978).
- [20] Nemat-Nasser, S., "On Finite Deformation of Elasto-Plasticity", Technical Report #81-8-43, Dept. Civil Engg., Northwestern University, August (1981).
- [21] Lee, E.H., Int. J. Solids Struct., 17, 859 (1981).
- [22] Kleiber, M., Int. J. Engg. Sci., 13, 513 (1975).
- [23] Green, A.E., and Naghdi, P.M., Arch. Rat. Mech. Anal., 18, 251 (1965).
- [24] Hill, R., J. Mech. Phys. Solids, 16, 229 (1968).
- [25] Hill, R., Proc. Roy. Soc., A314, 457 (1970).
- [26] Hill, R., Advances in Soil Mechanics, 18, 1 (1978).
- [27] Gurtin, M.E. and Spear, K., "On the Relationship Between the Logarithmic Strain Rate and the Stretching Tensor", to appear Int. J. Solids and Structures (1983).
- [28] Biot, M.A., Applied Sci. Research, A, 12, 151 (1963).
- [29] Zaremba, S., Bull. Int. Acad. Sci. Cracovie, 594 (1903).
- [30] Zaremba, S., Mem. Sci. Math., #82 (1937).
- [31] Jaumann, G., Sitzber. Akad. Wiss. Wien (IIa) 120, 385 (1911).
- [32] Oldroyd, J.G., Proc. Roy. Soc., A200, 523 (1950).
- [33] Truesdell, C., J. Rat. Mech. Anal., 4, 83 (1955).
- [34] Noll, W., J. Rat. Mech. Anal., 4, 3 (1955).

- [35] Dienes, J.K., Acta Mechanica, 32, 217 (1979).
- [36] Stören, S. and Rice, J.R., J. Mech. Phys. Solids, 23, 421 (1975).
- [37] Nemat-Nasser, S., in "Finite Element Analysis of Transient Non-Linear Structure Behaviour", Edited by Belytschko et al., ASME, 85 (1975).
- [38] Oravas, G.A.E., "Course Notes of Continuum Mechanics", Dept. of Civil Engg., McMaster University, Hamilton, Ontario (1982).
- [39] Nagtegaal, J.C. and DeJong, J.E., Proc. Workshop on Plasticity of Metals at Finite Strain, Div. Appl. Mech. Staford University, 65 (1982).
- [40] Lee, E.H. in Numerical Methods in Industrial Forming Processes, (Eds. J.F.T. Pittman et. al.), p. 39-50, Pineridge Press, Swansea, U.K. (1982).
- [41] Chu, E., The basic concept of strain contour, Metal Forming Research Report 83-002, Department of Mechanical Engineering, McMaster University, 1982.
- [42] Forsythe, G.E., Malcolm, M.A. and Moler, C.B., "Computer Methods for Mathematical Computations", Prentice Hall (1977).
- [43] Ahlberg, J.H., Nilson, E.N. and Walsh, J.L., "The Theory of Splines and Their Applications", New York: Academic Press (1967).
- [44] Mahamed, M., Master's Thesis, McMaster University.